

Copyright Undertaking

This thesis is protected by copyright, with all rights reserved.

By reading and using the thesis, the reader understands and agrees to the following terms:

- 1. The reader will abide by the rules and legal ordinances governing copyright regarding the use of the thesis.
- 2. The reader will use the thesis for the purpose of research or private study only and not for distribution or further reproduction or any other purpose.
- 3. The reader agrees to indemnify and hold the University harmless from and against any loss, damage, cost, liability or expenses arising from copyright infringement or unauthorized usage.

IMPORTANT

If you have reasons to believe that any materials in this thesis are deemed not suitable to be distributed in this form, or a copyright owner having difficulty with the material being included in our database, please contact lbsys@polyu.edu.hk providing details. The Library will look into your claim and consider taking remedial action upon receipt of the written requests.

DEVELOPMENT OF METAMATERIAL SANDWICH PLATES WITH INERTIAL AMPLIFICATION FOR BROADBAND LOW-FREQUENCY VIBRATION CONTROL

GAO LEI

PhD

The Hong Kong Polytechnic University

2025

The Hong Kong Polytechnic University Department of Building Environment and Energy Engineering

Development of metamaterial sandwich plates with inertial amplification for broadband low-frequency vibration control

GAO Lei

A thesis submitted in partial fulfillment of the requirements for the Degree of Doctor of Philosophy

April 2025

CERTIFICATE OF ORIGINALITY

I hereby declare that this thesis is my own work and that, to the best of my knowledge
and belief, it reproduces no material previously published or written, nor material that
has been accepted for the award of any other degree or diploma, except where due
acknowledgement has been made in the text.

_____(Signed)

GAO Lei (Name of student)

ABSTRACT

Sandwich plate structures have been extensively employed in various engineering fields, such as aerospace, mechanical and civil engineering, owing to their superior stiffness-to-weight ratio and load-bearing capabilities. However, their inherent lightweight and thin-walled characteristics make them particularly vulnerable to low-frequency and broadband vibrations. Traditional passive control methods, including locally resonant metamaterials, often suffer from narrow bandgaps and require heavy resonators to achieve low-frequency vibration attenuation. These limitations hinder their practical application in scenarios requiring compactness, low mass and high performance.

To address these challenges, this thesis presents a series of studies on the design, modeling, optimization and experimental validation of a novel class of metamaterial sandwich plates embedded with lever-type inertial amplification (IA). By leveraging the inertial amplification mechanism, the proposed structures enable the formation of multiple low-frequency bandgaps without increasing resonator mass or decreasing stiffness, thus achieving efficient vibration suppression while maintaining structural lightness.

The research begins with the development of a metamaterial sandwich plate with levertype IA (IA-MSP). A comprehensive dynamic model is established to capture the inertial amplification mechanism and its impact on the bandgap behavior. Theoretical analysis, finite element simulations and vibration experiments are performed to validate the ability of the IA-MSP to generate low-frequency bandgaps. Results show that the lever-type resonator serves to amplify the mass motion, thereby enhancing the effective mass of the system and leading to a reduction in the boundary frequencies of bandgaps. Increasing the lever ratio leads to a significant downshift in the bandgap frequency range, offering tuneable vibration control without added mass.

Building on this foundation, a two-degree-of-freedom lever-type IA mechanism is applied in the metamaterial sandwich plate (IA-MSP_{DF2}) to further enhance broadband vibration attenuation. In theoretical analysis, a theoretical dynamic model is constructed by theoretical bandgap formulation in predicting the characteristics of low-frequency multiple bandgaps in the IA-MSP_{DF2}. The effect of various parameters on the vibration transmission characteristics of the IA-MSP_{DF2} is studied. The numerical simulation is also validated through favorable agreement with the results obtained from experimental study. The results show that the coupling effect between the primary and secondary resonators contributes to the widening of attenuation zones. Increasing damping can merge the two bandgaps into a broader and more effective attenuation range, offering improved broadband performance over conventional designs.

To achieve precise control over multiple target frequencies, a graded lever-type IA resonator arrangement is introduced in the metamaterial sandwich plate (GLIA-MSP). This configuration employs periodic arrays of IA resonators with different lever ratios, enabling the formation of multiple low-frequency bandgaps. A hybrid design framework combining theoretical modeling, numerical simulations and genetic algorithm (GA)-based optimization is developed. Within this framework, the GA-based optimization is employed to systematically identify the optimal configuration of lever ratios, ensuring that the bandgaps are simultaneously aligned with the designated target

frequencies. The GLIA-MSP achieves superior bandwidth efficiency and mass effectiveness compared to conventional metamaterial sandwich plates with graded local resonators.

In addition, normalized comparative analyses demonstrate that the proposed IA-based metamaterial sandwich plates significantly outperform traditional designs in terms of vibration attenuation bandwidth and lightweight characteristics. The results show that the proposed IA-based metamaterial sandwich plates exhibit a wider normalized attenuation bandwidth γ and superior lightweight design when compared to other configurations of metamaterial sandwich plates. This remarkable lightweight characteristic enhances the potential of the proposed IA-based metamaterial sandwich plates to offer significant advantages in various engineering applications.

In conclusion, this thesis establishes a comprehensive framework for the design of metamaterial sandwich plates based on inertial amplification principles. The combination of advanced modeling, numerical simulations, experimental validation and intelligent optimization offers a robust approach for achieving low-frequency and broadband vibration suppression. The findings contribute significant insights to the field of metamaterials and hold strong potential for application in engineering systems requiring effective vibration control across multiple frequency ranges.

PUBLICATIONS ARISING FROM THIS THESIS

Journal Papers

Gao, L., Mak, C. M., Ma, K. W., and Cai, C. (2024). Mechanisms of multi-bandgap inertial amplification applied in metamaterial sandwich plates. *International Journal of Mechanical Sciences*, 109424.

Gao, L., Mak, C. M., and Cai, C. (2024). Low-frequency vibration attenuation of metamaterial sandwich plate with lever-type inertial amplified resonators. *Thin-Walled Structures*, 111827.

Gao, L., Mak, C. M, Cai, C and Deng, S. (2024) Metamaterial sandwich plates with two-degree of freedom inertial amplified resonators for broadband low-frequency vibration attenuation, *Mechanics of Advanced Materials and Structures*. 31(30), 12885–12897.

Conference Papers

Gao, L., Mak, C. M., and Cai, C., 2023. A metamaterial sandwich plate with spring-lever-mass resonators. Proceedings of the 52nd International Congress and Exposition on Noise Control Engineering, 2023, Inter-noise 2023, Chiba, Greater Tokyo, Japan.

Paper under review

Gao, L., Mak, C. M., Ma, K. W., and Cai, C. Graded lever-type metamaterial sandwich plate for low-frequency vibration attenuation. *Engineering Structures*. (Under review).

ACKNOWLEDGEMENT

First of all, I am profoundly thankful to my supervisor, Professor Mak Cheuk Ming, for his invaluable guidance, unwavering support and constant encouragement throughout the course of my doctoral studies. This research would not have been possible without his deep expertise, insightful advice and high standards of academic rigor, all of which have had a profound impact on both my research and personal growth. His guidance has greatly inspired my enthusiasm for future academic exploration

I am also grateful to Dr. Ma Kuen Wai for his technical support and assistance with my research papers, and to Dr. Cai Chenzhi from Central South University for his constructive feedback and helpful suggestions during my research. I am truly grateful to all members of our research group: Dr. Chen Lan, Dr. Kang Shengxian, Dr. Li Xiujie, Dr. Xue Rong, Ms. Li Wenxin, and Mr. Deng Supeng, for their support, collaboration, and warm companionship throughout my Ph.D. journey.

Finally, I extend my deepest gratitude to my parents and my wife, whose unwavering love, patience, and encouragement have been a continual source of strength throughout this journey.

Table of Content

CERTIFICATE OF ORIGINALITY	I
ABSTRACT	II
PUBLICATIONS ARISING FROM THIS THESIS	V
ACKNOWLEDGEMENT	VI
Table of Content	VII
Nomenclature	X
List of Figures	XIX
List of Tables	XXIV
Chapter 1	1
Introduction	1
1.1. Research Background	1
1.2. Research Problem Statement	4
1.3. Research Objectives and Significance	6
1.4. Outline of This Thesis	7
Chapter 2	10
Literature Review	10
2.1. Metamaterials	10
2.2. Vibration Control Using LR-type Metamaterials	11
2.3. Vibration Control Using IA Mechanisms	14
2.4 Summary and Research Gap	17
Chapter 3	20
Low-frequency Vibration Control of the IA-MSP	20
3.1. Methodology	21

3.1.1 Theoretical Derivation	21
3.1.2 Band Structure Calculation by Finite Element Method	27
3.1.3 Experimental Study	28
3.2. Results and Discussions	30
3.2.1 Band Structure and Mechanisms	30
3.2.2 Vibration Transmission Research of the IA-MSP	38
3.2.3 Results of Experimental Study	44
3.3. Summary	49
Chapter 4	51
Broadband Low-frequency Vibration Control of the IA-MSP _{DF2}	51
4.1. Methodology	52
4.1.1 Theoretical Model and Finite Element Modelling	52
4.1.2 Experimental Specimen and Setup	63
4.2. Results and Discussions	64
4.2.1 Vibration Transmission Research of the IA-MSP _{DF2}	65
4.2.2 Effects of Parameters on Vibration Transmission	70
4.2.3 Experimental Validation	73
4.2.4 Effect of Damping on Bandgaps of the IA-MSP _{DF2}	77
4.3. Summary VIII	79
7 111	

Chapter 5	82
Precise Multi-frequency Vibration Control of the GLIA-MSP	82
5.1. Methodology	83
5.1.1 Theoretical Derivation	83
5.1.2 Vibration Response Analysis and Numerical Model	86
5.1.3 Optimization Methodology	88
5.2. Results and Discussions	90
5.2.1 Dispersion Relationship and Vibration Transmission Research	91
5.2.2 Comparative Study and Effect of Lever Ratios	94
5.2.3 Optimization and Normalized Comparison	99
5.3. Summary	104
Chapter 6	107
Conclusions and Suggestions for Future Work	107
6.1. Conclusion	107
6.2. Suggestions for Future Work	109
Defenences	111

Nomenclature

Abbreviation Description

LR Local resonance

IA Inertial amplification

IA-MSP Metamaterial sandwich plate incorporating lever-type IA resonators

Metamaterial sandwich plate embedded with two-degree of freedom

IA-MSP_{DF2}

inertial amplified resonators

GA Genetic algorithm

CUF Carrera Unified formulation

CSPs corrugated-core sandwich panels

FEM Finite element method

FFT Fast Fourier Transform

LR-MSP Metamaterial sandwich plates with local resonators

AZ Attenuation zone

BG Bandgap

RW Relative bandwidth

IA-MSP _{DF2}	Metamaterial sandwich plate that incorporates two-degree of freedom inertial amplified resonators
LR-MMSP	Metamaterial sandwich plates incorporating multi-frequency local resonators
AZ1	The first attenuation zone of the IA-MSP _{DF2}
AZ2	The second attenuation zone of the IA-MSP _{DF2}
2-DOF	Two degrees of freedom
GLIA-MSP	Metamaterial sandwich plate with periodic graded arrays of lever- type inertial amplification resonators
GLR-MSP	Metamaterial sandwich plates with periodic graded arrays of local resonators
BER	Bandwidth efficiency ratio
GLIA-1	The first graded lever-type IA resonator
GLIA-2	The second graded lever-type IA resonator
GLIA-3	The third graded lever-type IA resonator
VT	Vibration transmissibility

Terms Description

k The spring stiffness in the IA-MSP The mass in the IA-MSP m The distance between the spring and support bar within the primary l_1 lever-type IA resonator The distance between the support bar and the mass within the l_2 primary lever-type IA resonator The distance between the spring and support bar within the l_3 secondary lever-type IA resonator The distance between the support bar and mass within the secondary l_4 lever-type IA resonator The strain in the *x*-direction ε_x The strain in the *y*-direction ε_v The shear strain γ_{xy} The transverse displacement of the face plates w Q The elastic constants matrix UThe elastic strain energy of the face plates TThe kinetic energy of the face plates The density of the face plates ρ

V	The volume of the face plates
w_0	The transverse displacement of support bar in the IA-MSP
w_1	The displacement of the primary mass
W_2	The displacement of the secondary mass
T_r	The kinetic energy of the resonator in the IA-MSP
U_r	The elastic strain energy of the resonator in the IA-MSP
R	The lever ratio in the IA-MSP
α	Wavenumbers in the <i>x</i> - direction
β	Wavenumbers in the <i>y</i> - direction
ω	Angular frequency
Н	The overall height of the structure
h	The thickness of the face plates
a_x	Lattice constants along the x direction
a_y	Lattice constants along the y direction
γ	The mass ratio between the resonator and faceplates
∇	Differential operator
r	Position vector

C (r) Position dependent elastic tensor

u(r) Displacement vector

Time

k Wave vector

 $\mathbf{u}_{\mathbf{k}}(\mathbf{r})$ Modulation function of the displacement

a Lattice constant vector

 $\Omega(\mathbf{k})$ Stiffness matrices

M Mass matrices

P Acceleration integration

 f_l The lower boundary of the bandgap

 f_u The upper boundary of the bandgap

 r_{ρ} The mass ratios of resonator

 ρ_m The varying mass density of the inertial amplified resonator

 ρ_1 The initial mass density of the inertial amplified resonator

 r_E The Young's modulus ratios of the resonator

 E_s The varying Young's modulus of the resonator spring

 E_1 The initial Young's modulus of the resonator spring

The density ratios of the face plate $r_{\rho f}$ The varying density of the face plate ρ_f The initial density of the face plate ρ_2 $f_{nd.l}$ Normalized lower boundary frequency Lattice constant a The shear wave velocity of the host structure v_{s} Relative density $\bar{\rho}_c$ The average density of the core ρ_c The eigenfrequency of the primary lever-type IA resonator f_p The eigenfrequency of the secondary lever-type IA resonator f_{s} The mass of the primary lever-type IA resonator m_1 The mass of the secondary lever-type IA resonator m_2 The spring stiffness of the primary lever-type IA resonator k_1 The spring stiffness of the secondary lever-type IA resonator k_2 The lever ratio of the primary lever-type IA resonators R_1 The lever ratio of the secondary lever-type IA resonators R_2 T_{m1} The kinetic energy of the primary resonator

T_{m2}	The kinetic energy of the secondary resonator
U_{m1}	The elastic strain energy of the primary resonator
U_{m2}	The elastic strain energy of the secondary resonator
f_{l1}	The lower boundary frequency of the first bandgap for the IA- $\ensuremath{MSP_{DF2}}$
f_{u1}	The upper boundary frequency of the first bandgap for the IA- $\ensuremath{MSP_{DF2}}$
f_{l2}	The lower boundary frequency of the second bandgap for the IA- $\ensuremath{MSP_{DF2}}$
f_{u2}	The upperboundary frequency of the second bandgap for the IA- $\ensuremath{MSP_{DF2}}$
M	The mass of two face plates in the unit cell
χ	The mass ratio of the secondary lever-type IA resonator to the primary lever-type IA resonator
ψ	The mass ratio of the primary lever-type IA resonator to the face plates
m_c	The total mass of the core layer
V_c	The space volume occupied by the core layer

V_s	The equivalent volume of core layer
\widetilde{C}	The complex elastic modulus of the resonator
C	The elastic modulus of the resonator without damping
$\eta_{_{ m S}}$	Structural loss factor
T_{r1}	The kinetic energy of the GLIA-1
T_{r2}	The kinetic energy of the GLIA-2
T_{r3}	The kinetic energy of the GLIA-3
U_{r1}	The elastic strain energy of the GLIA-1
U_{r2}	The elastic strain energy of the GLIA-2
U_{r3}	The elastic strain energy of the GLIA-3
A_{in}	The displacement of the input point A,
B_{out}	The displacement of the output point B.
f_{ci}	The center frequency of the <i>i</i> -th bandgap
$f_{ci}^{ m target}$	The target center frequency of the f_{ci}
γ_i	Weighting coefficient
F	fitness function

- f_{c1} The center frequency of the bandgap 1
- f_{c2} The center frequency of the bandgap 2
- f_{c3} The center frequency of the bandgap 3

List of Figures

Figure 3.1 (a) The schematic diagram of IA-MSP. (b) The unit cell of IA-MSP. (c) The
simplified model of the unit cell of IA-MSP. (d) The displacements of the spring-lever-
mass system. (e) The irreducible Brillouin zone (grey zone) and sweeping direction of
wave vectors (M- Γ -X-M-Y- Γ).
Figure 3.2 The experimental specimen of an IA-MSP with 6×5 unit cells: (a) without
upper face plate; (b) global photo.
Figure 3.3 The experimental setup of the vibration test
Figure 3.4 Band structure of IA-MSP (dotted black line) and eigenfrequencies of the
inertial amplified resonator (dashed red line)
Figure 3.5 Bandgap boundaries of the IA-MSP derived through theoretical prediction
and numerical simulation (FEM): (a) boundary frequencies with R , (b) boundary
frequencies with r_{ρ} , (c) boundary frequencies with r_{E} , (d) boundary frequencies with $r_{\rho f}$
Figure 3.6 (a) The unit cell of LR-MSP. (b) The simplified model of LR-MSP unit cell.
(c) The band structure of LR-MSP and the vibration mode shapes associated with the
lower and upper boundary frequency
Figure 3.7 The model of the IA-MSP with 6×5 unit cells and boundary conditions.39
Figure 3.8 The acceleration response of the IA-MSP $(R = 2)$ and sandwich plate without
resonators

Figure 3.9 Vibration modes of the IA-MSP ($R = 2$) at different excitation frequencies:
(a) $f = 39$ Hz; (b) $f = 52$ Hz; (c) $f = 109$ Hz42
Figure 3.10 The acceleration response of the LR-MSP and IA-MSP ($R = 2$)
Figure 3.11 The acceleration response of the IA-MSP at different <i>R</i> -values
Figure 3.12 The result comparison: (a) the band structure of the IA-MSP, (b) the
acceleration response in the numerical analysis, (c) the acceleration response in the
experiment
Figure 3.13 Normalized comparisons between the IA-MSP and (a) typical
metamaterials sandwich plates. Comparison of (b) the single-phase metamaterial
sandwich plates and (c) the multi-phase metamaterial sandwich plates
Figure 4.1 Schematic diagram of IA-MSP _{DF2} : (a) a unit cell; (b) displacements of the
lever-type IA resonators in a unit cell; (c) the model of IA-MSP _{DF2} with 6×5 unit cells
and boundary conditions
Figure 4.2 Unit cell of the metamaterial plate with 2-DOF spring-mass resonators.
(Xiao et al., 2019)59
Figure 4.3 Dispersion surfaces of the IA-MSP _{DF2} : (a) dispersion surfaces, (b) a front
view of dispersion surfaces and (c) a partial magnification of dispersion surfaces 60
Figure 4.4 Dispersion surfaces of the IA-MSP _{DF2} at different lever ratios: (a) $R_1 = R_2 =$
1, (b) $R_1 = R_2 = 2$, (c) $R_1 = R_2 = 3$, and (d) $R_1 = R_2 = 4$
Figure 4.5 Experimental specimen of the IA-MSP _{DF2} and experimental setup 64

Figure 4.6 Comparison of the theoretical results and the FEM results: (a) the dispersion
surfaces of IA-MSP _{DF2} predicted theoretically, (b) the acceleration response through
the FEM analysis
Figure 4.7 The top view of vibration modes of the IA-MSP _{DF2} with 6×5 unit cells at
the marked frequencies in Figure 4.6 (b): (a) $f = 36$ Hz (falling within the passband);
(b) $f = 40$ Hz (falling within the bandgap1); (c) $f = 60$ Hz (falling within the bandgap2);
(c) $f = 174$ Hz (falling within the passband)
Figure 4.8 Schematic diagram of (a) the unit cell of the metamaterial sandwich plate
incorporating multi-frequency local resonators (LR-MMSP); (b) simplified model of
the unit cell
Figure 4.9 Acceleration response of the IA-MSP _{DF2} and the LR-MMSP69
Figure 4.10 Dispersion surfaces and acceleration responses of the IA-MSP _{DF2} : (a) R_1 =
$R_2 = 1.5$, (b) $R_1 = R_2 = 2$, (c) $R_1 = R_2 = 2.5$, and (d) $R_1 = R_2 = 3$ 70
Figure 4.11 Acceleration responses of the IA-MSP _{DF2} for different parameters: (a)
eigenfrequencies of the primary lever-type IA resonator fp , (b) eigenfrequencies of the
secondary lever-type IA resonator fs , (c) resonator mass ratios $\chi = m2/m1$, (d) mass
ratios of the primary lever-type IA resonator to the face plates $\psi = m1/M$
Figure 4.12 Comparison of the acceleration responses: (a) in the numerical simulation;
(b) in the experimental study
Figure 4.13 Normalized comparison of normalized attenuation bandwidth γ and the
relative density ρc between the proposed IA-MSP _{DF2} and other metamaterial
sandwich plates

Figure 4.14 The acceleration responses of IA-MSP _{DF2} at different damping ratio 78
Figure 4.15 Vibration modes of faceplates and resonators of IA-MSP _{DF2} with
η s = 0.01 and η s = 0.2 at different excitation frequencies: (a) f = 450 Hz; (b) f = 650
Hz
Figure 5.1 Schematic illustration of (a) GLIA-MSP; (b) unit cell of GLIA-MSP and (c)
displacements of three graded lever-type IA resonators (GLIA-1, GLIA-2 and GLIA-
3) in an equivalent unit cell model
Figure 5.2 Numerical model of the GLIA-MSP comprising 6×5 unit cells
Figure 5.3 Flowchart of the GA optimization
Figure 5.4 Theoretical and numerical results. (a) 3D view of dispersion surfaces of the
GLIA-MSP; (b) front view; (c) magnified view; (d) vibration transmissibility of GLIA-
MSP with 6×5 unit cells and (e) vibration modes of GLIA-MSP at the excitation
frequencies of 54, 70, 77, 103, 140, and 175 Hz
Figure 5.5 Comparison of bandgap characteristics between GLIA-MSP and GLR-MSP.
(a) Theoretical bandgap distributions; (b) Vibration transmissibility of GLIA-MSP
$(R_1 = R_2 = R_3 = 1.5)$ and GLR-MSP96
Figure 5.6 Effect of lever ratios on the vibration transmissibility of GLIA-MSP: (a) R_1 =
$R_2 = R_3 = 1.5$; (b) $R_1 = R_2 = R_3 = 2$; (c) $R_1 = R_2 = R_3 = 2.5$ and (d) $R_1 = R_2 = R_3 = 3$
Figure 5.7 Vibration transmissibility of GLIA-MSP ($R_1 = R_2 = R_3 = 1.5$) with a 6×5 unit
cell arrangement under different boundary conditions

Figure 5.8 Vibration transmissibility of GLIA-MSP ($R_1 = R_2 = R_3 = 3$) at different
damping ratio
Figure 5.9 Optimization results for target bandgap center frequencies (50 Hz, 100 Hz,
150 Hz): (a) dispersion surfaces of the GLIA-MSP and (b) vibration transmissibility of
GLIA-MSP with 6×5 unit cell configuration
Figure 5.10 Normalized comparison of relative bandwidth (RW), relative density ρc
and bandwidth efficiency ratio (BER) between GLIA-MSP and other metamaterial
sandwich plates

List of Tables

Table 3.1 Geometrical parameters of IA-MSP. ($a = 0.1 \text{ m}$)
Table 3.2 Material parameters
Table 3.3 Geometrical parameters of the experimental specimen of an IA-MSP with 6
\times 5 unit cells. ($a = 0.1 \text{ m}$)
Table 4.1 Geometrical parameters of the IA-MSP _{DF2} . ($a = 0.1 \text{ m}, h = 0.002 \text{ m}$) 62
Table 4.2 Material parameters of the IA-MSP _{DF2} 62
Table 5.1 Geometrical parameters of the GLIA-MSP. ($a_x = a_y = a = 0.1 \text{ m}$)
Table 5.2 Material parameters of the GLIA-MSP
Table 5.3 Comparison of bandgaps for GLIA-MSP with varying lever ratios alongside
those of GLR-MSP96
Table 5.4 Optimization results of the GLIA-MSP

Chapter 1

Introduction

1.1. Research Background

Sandwich plate structures, comprising two face plates and a core layer, are extensively used in diverse fields of engineering applications, encompassing aerospace, transportation, civil engineering, and marine engineering, owing to the high stiffnessto-weight ratio properties (Ruzzene, 2004; Teng et al., 2023; Vinson, 2001; Z.-J. Wu et al., 2013; Yang et al., 2013; Zok et al., 2004). However, as lightweight and thinwalled structures, the sandwich plates usually perform poorly in the vibro-acoustic fields, significantly limiting their application (Song et al., 2019). To improve their vibration attenuation and sound insulation performance, various methods have been developed, including damping treatment (Z.-J. Wu et al., 2013; Yang et al., 2013), structural design (Denli & Sun, 2007; Wang et al., 2009), vibration absorbers (Mak & Jianxin, 2002; Mak et al., 2023; Yu Sun et al., 2019), and active control (Araújo et al., 2010; Luo et al., 2008). The present methods for controlling vibrations are centred mainly on the regulation of mid-to-high-frequency vibrations, with the exception of active control. Although effective in attenuating low-frequency vibrations, the utilization of an external circuit often constrains the practical application of active control in engineering. Thus, low-frequency vibration attenuation of sandwich plates remains a challenging issue that needs to be addressed in engineering applications.

In recent decades, metamaterials have garnered significant attention as a type of artificial metamaterials that are composed of periodically arranged microstructures. The word "meta" is derived from Greek and translates as "beyond". The metamaterials possess remarkable physical properties that surpass those of conventional structures, including negative Poisson's ratio (Tao et al., 2022; Yasuda & Yang, 2015), negative effective stiffness (S. Lin et al., 2021; Y. Liu et al., 2022), and wave guide (Y. Wang et al., 2021; P. Zhao et al., 2021), among others. It is noteworthy that metamaterials possess bandgaps, which correspond to frequency regions in which elastic and acoustic wave propagation is inhibited. This feature has opened up a novel avenue for regulating low-frequency vibration and noise. Previous studies have reported that the bandgap has two generation mechanisms, Bragg scattering and local resonance (LR). The Bragg scattering mechanism arises from the interference and multiple scattering effects between the periodic units of the structure (Brillouin, 1953; Mead, 1996; Timorian et al., 2020). The unit cell's lattice constant corresponds to a wavelength within a similar range, limiting the attainment of low-frequency bandgaps. Large-sized structures or materials with high density or low modulus are required to acquire a low-frequency Bragg bandgap. In 2000, the concept of photonic crystal based on LR mechanism was initially introduced by Z. Liu et al. (2000). This innovation broke the limitation of generating low-frequency bandgaps in the metamaterials by creating a bandgap two orders of magnitude smaller than the lattice constant of a unit cell. The cause of LR mechanism generation can be understood using the "spring-mass" resonator model (Chen et al., 2011; Huang et al., 2019; Vo et al., 2022; Yao et al., 2008). This model demonstrates how local resonators can convert external work into kinetic energy when the forcing frequency aligns with the resonance frequency. To ameliorate its property

of the low frequency vibration attenuation, a variety of resonators (spring-mass subsystem), such as mass-beam resonators (Jinqiang Li et al., 2020), plate-type resonators (Q. Wang et al., 2021), membrane-type resonators (J. Li et al., 2023), simply cantilever beam resonators (Qiang et al., 2021), and other types of resonators (H. Li et al., 2021; Z.-Y. Li et al., 2020; G.-L. Yu & Miao, 2019), have been periodically incorporated into the core layer of the sandwich plate. The local resonant properties of these resonators can be activated within the bandgap and create inertial forces to weaken the vibration of the plate (An et al., 2023).

An alternative approach utilizing the inertial amplification (IA) mechanism has been proposed to realize bandgaps without sacrificing structural stiffness or considerably increasing system mass. In 2007, Yilmaz et al. (2007) proposed a substitute approach based on the IA mechanism to achieve low-frequency bandgaps without compromising the overall stiffness or significantly increasing the total mass. This approach involves enhancing the effective inertia of the system through motion amplification of small masses. The IA mechanism has been employed as fundamental elements in discrete and continuous systems for the design of diverse lattice configurations (Acar & Yilmaz, 2013; Banerjee et al., 2021; Bhatt et al., 2022; Xiang Fang et al., 2018; Orta & Yilmaz, 2019; Yilmaz & Hulbert, 2010; Yuksel & Yilmaz, 2015, 2020). These investigations studied the wave propagation behavior of periodic lattices incorporating IA mechanisms. The exceptional capabilities of the low-frequency vibration isolation in periodic lattices integrated with IA mechanisms were validated. Then, the IA mechanism was introduced in metamaterial design to facilitate the mitigation of lowfrequency vibrations (N. M. Frandsen et al., 2016; Jingru Li et al., 2020; J. Li et al., 2022; Mizukami et al., 2021; Mu et al., 2022a, 2022b; S. Muhammad et al., 2020; Xi et al., 2021; Y. Xue et al., 2024; Zeng, Cao, Wan, Guo, An, et al., 2022; C. Zhao, Zhang, Zhao, & Deng, 2023; C. Zhao, Zhang, Zhao, Hong, et al., 2023). This approach does not require sacrificing stiffness or increasing the total mass, thereby overcoming the drawbacks of previously mentioned methods.

1.2. Research Problem Statement

The practical application of LR-type metamaterials sandwich plates in attenuating lowfrequency vibration is confronted with formidable challenges. A considerably heavy resonator mass, which composes a substantial portion of the total medium mass, is required to open up the bandgap at low frequency. The realization of weighty resonators within small-size sandwich structures poses a complex design problem. A novel approach to tuning bandgap frequencies involves incorporating IA mechanisms into metamaterial design. The IA mechanism with a small mass can play a positive role in achieving strong vibration attenuation at low frequencies. The bandgap frequency ranges generated by IA mechanisms are primarily influenced by the amplification angle, which refers to the deviation between the host structure and each lateral bar. To achieve low-frequency bandgaps, a substantial amplification angle is required, necessitating the use of long lateral bars within the IA mechanism. However, accommodating these long bars poses a significant constraint in many real-world applications due to space limitations. Therefore, there is a need to investigate and develop lightweight and compact designs to attain vibration attenuation at lower frequencies in the sandwich plate.

The IA mechanism offers a solution to low-frequency vibration attenuation in the sandwich plate. However, IA resonators possess a limited operational bandwidth, as it exhibits optimal efficacy solely at its resonant frequency within a relatively narrow frequency range. Lower frequency bandgaps are commonly accompanied by narrower bandwidths. Multi-bandgap mass-spring resonators have been introduced into the metamaterial plates to obtain broadband vibration attenuation (Fan et al., 2022; Peng et al., 2015; Xiao et al., 2019). To the best of the authors' knowledge, metamaterial sandwich plates inspired by the idea of multi-bandgap inertial amplified resonators have never been presented in previous literature. The achievement of multiple bandgaps can facilitate the merging and broadening of bandgaps. Therefore, it is necessary to explore the achievement of multi-frequency lever-type IA metamaterial sandwich plate for obtaining broadband vibration attenuation.

In addition, most existing studies have implemented uniform resonator configurations in the metamaterials, which inherently limit the range of adjustable parameters and thus restrict the achievable bandgap range. This limitation significantly hinders the vibration control performance of metamaterial sandwich plates in applications requiring multiple frequency band ranges. Therefore, further research is required to develop an innovative analytical framework and an optimization-based approach to enhance the performance and adaptability of metamaterial sandwich plates for multi-frequency vibration control. Additionally, achieving precise alignment of multiple bandgaps with target frequency ranges is essential for improving vibration suppression efficiency and structural performance.

1.3. Research Objectives and Significance

Due to the limitation of the previous studies, this thesis aims to propose novel class of metamaterial sandwich plates embedded with lever-type IA to achieve low-frequency and broadband vibration control. The primary objective of this study is to analyse the effectiveness of the proposed metamaterial sandwich plates in attenuating the low-frequency vibration utilizing theoretical dynamical model, numerical analysis, experimental study and algorithm optimization. Specifically, the study seeks:

- 1) To establish a theoretical dynamic model of proposed metamaterial sandwich plates embedded with lever-type IA mechanisms. The dispersion equations of the unit cell are derived, and the lever-type IA mechanisms employed in the metamaterial sandwich plate to achieve lower frequency bandgap are interpretated.
- 2) To investigate vibration suppression characteristics of proposed metamaterial sandwich plates numerically and experimentally. Comparative studies are conducted to assess the effectiveness of both the metamaterial sandwich plates with lever-type IA mechanisms and LR-type metamaterials sandwich plates in attenuating low-frequency vibrations.
- 3) To quantitatively evaluate the vibration attenuation performance and lightweight efficiency of the proposed metamaterial sandwich plates. The effects of the structural parameters on the vibration transmission characteristics of the metamaterial sandwich plates with lever-type IA mechanisms are studied.
- 4) To develop an optimization framework for metamaterial sandwich plates with lever-type IA mechanisms, with the goal of achieving precise alignment of multiple bandgaps with target frequency ranges. This approach enhances the performance

and adaptability of metamaterial sandwich plates in multi-frequency vibration control applications.

This study concerns theoretical analysis, numerical simulation, experimental research and algorithm optimization to contribute to improving the vibration suppression performance of sandwich plates. The theoretical analysis elucidates underlying mechanisms of the lever-type IA resonator for attenuating low-frequency vibrations in sandwich panels, which establishes a solid foundation for future research in the field. The numerical simulation enables an intuitive comparison of bandgap characteristics and vibration suppression performance between the metamaterial sandwich plates with lever-type IA mechanisms and LR-type metamaterials sandwich plates. It can also obtain the relationships between parameters (e.g. geometrical and material parameters) and the vibration attenuation performance. Experimental studies serve to confirm the theoretical and numerical results while providing an opportunity to assess the feasibility and effectiveness of metamaterial sandwich plates with lever-type IA mechanisms in achieving low-frequency broadband vibration isolation in engineering applications. An optimization-based approach is proposed to achieve precise alignment of multiple bandgaps with target frequency ranges.

1.4. Outline of This Thesis

This chapter outlines the research background, problems, objectives, and significance of the thesis. The remaining chapters are summarized as follows:

Chapter 2 presents a review of relevant literature on metamaterials, with a particular focus on vibration control using LR-type metamaterials and IA mechanisms. Existing research in both approaches is summarized to identify current limitations and motivate the research presented in this thesis.

Chapter 3 introduces the lever-type IA mechanism into the design of metamaterial sandwich plates for the first time. Through the amplification of resonator motion, the lever mechanism contributes to an effective increase in the system's dynamic mass, resulting in a reduction of the coupled-mode frequency and enabling low-frequency bandgap formation. This chapter demonstrates the superior vibration isolation capabilities of the proposed lever-type IA metamaterial sandwich plate (IA-MSP) compared to conventional LR-based configurations.

Chapter 4 proposes a novel metamaterial sandwich plate embedded with two-degree of freedom inertial amplified resonators (IA-MSP_{DF2}) to achieve broadband low-frequency vibration attenuation. The findings offer important guidance on the design principles and parametric control of multi-bandgap behavior in metamaterial sandwich structures.

Chapter 5 develops a comprehensive design and optimization framework that integrates theoretical modeling, finite element simulations, and genetic algorithm (GA)-based optimization. The aim is to precisely tune multiple bandgaps to desired frequency targets, thereby enhancing the effectiveness and adaptability of lever-type IA metamaterial sandwich plates in multi-frequency vibration control applications.

Chapter 6 summarizes the key contributions and findings of the entire PhD project. It also outlines recommendations for future studies on vibration control by using levertype IA metamaterial sandwich plates.

Chapter 2

Literature Review

2.1. Metamaterials

Metamaterials, which are composed of artificially arranged microstructures, have garnered extensive research interest due to their unique capabilities in waveguiding (Mousavi et al., 2015; P. Zhao et al., 2021), energy dissipation (Hussein & Frazier, 2013; Mei et al., 2023) and energy localization (Oudich et al., 2011; Thomes et al., 2022). These extraordinary functionalities are fundamentally derived from the bandgap properties of metamaterials, where elastic waves within the bandgap range are prevented from propagating through the structure. Currently, metamaterial bandgaps are generally categorized into Bragg scattering bandgaps and locally resonant bandgaps. The Bragg scattering bandgap arises due to the interference between transmitted and reflected waves at periodic interfaces. Since its formation mechanism is inherently dependent on the periodicity of the structure, the wavelength of the Bragg scattering bandgap is generally comparable to the lattice constant, resulting in bandgaps that predominantly lie in the high frequency (W. Gao et al., 2022; Tallarico et al., 2023). Consequently, achieving low-frequency Bragg scattering bandgaps necessitates large structural dimensions, which significantly limits their practical application in lowfrequency vibration suppression. By contrast, the locally resonant bandgap, first discovered in 2000 by Liu et al. (Z. Liu et al., 2000), provides a more effective approach

for low-frequency vibration control. Unlike Bragg scattering systems, locally resonant metamaterials can achieve bandgaps where the elastic wavelength significantly exceeds the lattice dimension—by as much as two orders of magnitude. This characteristic facilitates low-frequency vibration suppression using compact structures, overcoming the size constraints inherent to Bragg scattering metamaterials. Due to this advantage, locally resonant metamaterials have great potential for low-frequency vibration isolation.

2.2. Vibration Control Using LR-type Metamaterials

Researchers have extensively investigated locally resonant metamaterials in various structural forms, including beams, plates, shafts and rods (Choi et al., 2022; Hu et al., 2021; Hussain & Lim, 2021; J. Li et al., 2023; Lou et al., 2025; Nobrega et al., 2016; Patro et al., 2023; Shi et al., 2022; Tao et al., 2022; Z. Wu et al., 2019; Xu & Jing, 2024; D. Yu et al., 2006; S. Zhang et al., 2023), further expanding their applicability in engineering vibration control. D. Yu et al. (2006) investigated the vibration properties of Timoshenko beams integrated with periodic local resonators through theoretical analysis and experimental validation. The results showed the local resonators induced low-frequency bandgaps, offering a means for effectively controlling flexural vibrations in beams. Hu et al. (2021) developed a metamaterial beam that comprises multiple local resonators with distinct resonance frequencies to achieve broadband vibration suppression. Tao et al. (2022) devised a metamaterial plate composed of resonant cylinders that demonstrate an intriguing negative Poisson's ratio property.

This unique design aimed to enhance the structure's performance on attenuating the low-frequency vibration. J. Li et al. (2023) employed membrane-mass resonators as local resonators within a plate. The resonator inclusion proved to be highly beneficial, as it significantly enhanced the vibration suppression performance of the plate. Hussain and Lim (2021) proposed a novel metamaterial pillared-plate structure featuring an exceptionally wide local resonance bandgap. Through numerical simulations and experimental investigations, they demonstrated that the expansion of the local resonance bandgap could be achieved through simultaneous modulation of the composite pillar mass density and the plate stiffness. Cinefra et al. (2021) employed the Carrera Unified Formulation (CUF) within a finite element framework to investigate metamaterial plates. The utilization of CUF finite elements resulted in improved computational efficiency for heterogeneous materials. The CUF is a versatile method that can be applied to diverse structural modeling scenarios(Erasmo Carrera et al., 2021; Erasmo Carrera et al., 2013; Erasmo Carrera & Giunta, 2010; E Carrera & Zozulya, 2022; De Miguel et al., 2021; Pagani & Carrera, 2017).

The concept of locally resonant metamaterials has been used in developing plate structure, especially sandwich plates, with the aim of achieving superior performance in attenuating vibrations within low-frequency regimes (An et al., 2023; Choi et al., 2023; Choi et al., 2024; Jiang et al., 2021; H. Li et al., 2022; H. Li et al., 2021; Jinqiang Li et al., 2020; J. Li et al., 2023; Lim, 2019; Song et al., 2020; Q. Wang et al., 2021; Xi et al., 2022; Yan et al., 2022; Y. Zhang et al., 2021). An et al. (2023) presented a novel type of meta-orthogrid sandwich plates that were equipped with locally resonant resonators for achieving efficient low-frequency vibration attenuation. The springmass resonators were periodically embedded within tubes positioned between the two

faceplates. The bandgap in the range of 95.02–115.55 Hz was primarily induced by the resonance characteristics of the embedded resonator. Choi et al. (2023) introduced a plate-type locally resonant metamaterial designed for efficient low-frequency vibration isolation. The local resonator within the structure employed stainless steel and silicone rubber. This combination resulted in a local resonance bandgap ranging from 38.8 Hz to 44.2 Hz. Then, they presented a hybrid behavior of locally resonant bandgap and vibration attenuation mechanisms to achieve broadband vibration control. The hybrid isolation behavior enables the realization of a bandgap spanning from 34.42 Hz to 52.91 Hz in the experimental investigation. The presence of material damping within the experimental resonators can facilitate the expansion of the bandgap beyond the boundary frequencies identified by numerical analysis (Choi et al., 2024). In addition, multi-frequency resonators have been introduced in the design of metamaterial plates to achieve vibration isolation across multiple bandgaps (Fan et al., 2022; Peng et al., 2015; Xiao et al., 2019). Peng et al. (2015) investigated the mechanism of multibandgap metamaterial plate incorporating two-mass resonators for broadband vibration isolation. Two distinct bandgaps were identified within the ranges of 712.9–737.6 Hz and 891.7-912.1 Hz. Notably, it was found that the presence of high damping in resonators facilitated the merging of two bandgaps into a broader bandgap. Xiao et al. (2019) proposed a laminate acoustic metamaterial with two degrees of freedom local resonators. Two distinct bandgaps were generated around the resonant frequency of the resonators. The first bandgap spans from 352 Hz to 378 Hz, while the second bandgap ranges from 442 Hz to 465.5 Hz. Fan et al. (2022) devised a design for metamaterial sandwich plates featuring two coupled mass-beam resonators. This design enabled the

achievement of two low-frequency bandgaps spanning 51.6–78.9 Hz and 100.2–156.4 Hz.

Beyond passive design strategies, active control, nonlinear mechanisms, and quasi-zero stiffness concepts have been integrated into locally resonant metamaterial sandwich plates to tune and widen bandgaps, thereby improving low-frequency vibration attenuation performance. Li et al. (Z.-Y. Li, T.-X. Ma, et al., 2022; Z.-Y. Li, Y.-Z. Wang, et al., 2022; Z.-Y. Li et al., 2024) attached piezoelectric patches to a locally resonant metamaterial sandwich plate and employed an external circuit to achieve active adaptive feedback control of vibration. Fang et al., (Fang et al., 2017; Fang et al., 2016; Xin Fang et al., 2018) introduced nonlinearities into locally resonant metamaterials and were the first to discover and confirm the chaotic band phenomenon, demonstrating its effectiveness in low-frequency broadband vibration suppression. They further investigated vibration reduction properties of nonlinear metamaterial sandwich plates (Sheng et al., 2023). Zhou et al. (Cai et al., 2023; Cai, Zhou, Wang, Pan, et al., 2022; Cai, Zhou, Wang, Xu, et al., 2022; Q. Lin et al., 2022) applied the quasi-zero stiffness concept to metamaterial beams, plates and pipes, leveraging the high static and low dynamic stiffness properties to realize ultra-low-frequency bandgaps.

2.3. Vibration Control Using IA Mechanisms

In recent years, inertial amplification (IA) method has been introduced in metamaterial design to achieve the vibration control (Banerjee et al., 2021; Bhatt et al., 2022; Hussein

et al., 2022; Jingru Li et al., 2020; Yilmaz & Hulbert, 2010; Yilmaz et al., 2007; Yilmaz & Kikuchi, 2006; C. Zhao, Zhang, Zhao, Hong, et al., 2023). Yilmaz et al. (Yilmaz & Hulbert, 2010; Yilmaz et al., 2007; Yilmaz & Kikuchi, 2006) firstly utilized the motion amplification of a small mass to induce low-frequency bandgaps. This approach does not require sacrificing stiffness or increasing the total mass, thereby overcoming the drawbacks of previously mentioned methods. Building upon this concept, researchers have extended IA mechanisms into various configurations, including triangular (Acar & Yilmaz, 2013; Jingru Li et al., 2020; Yuksel & Yilmaz, 2015, 2020; Zeng, Cao, Wan, Guo, An, et al., 2022; J. Zhang et al., 2025; C. Zhao, Zhang, Zhao, Hong, et al., 2023), x-type (H. Li et al., 2023; Y. Li & Zhou, 2021; Russillo et al., 2022; Yonghang Sun, Dong, et al., 2024; Yonghang Sun, Zhang, et al., 2024), pyramidal (Mi & Yu, 2021; Otlu et al., 2023; Xi et al., 2022) and lever-type (L. Gao, Mak, & Cai, 2024; L. Gao, Mak, Cai, et al., 2024; L. Gao, Mak, Ma, et al., 2024; Yonghang Sun et al., 2025; S. Wang et al., 2021; Xi et al., 2023; Zeng, Cao, Wan, Guo, Wang, et al., 2022) resonators to control wave propagation. Jingru Li et al. (2020) incorporated the IA mechanism into the design of a metamaterial sandwich beam featuring pyramidal truss cores. This innovative design aimed to attain multiple and broader frequency bandgaps to effectively attenuate vibrations. Banerjee et al. (2021) proposed a new conception for obtaining a wider bandgap with a dual-attenuation peak through coupling IA and LR mechanism to achieve strong vibration isolation. Zhao et al. (2023) presented a kind of IA metamaterials that incorporate double resonators. The unique aspect of this design lies in the merging of bandgaps within the realm of double-zero effectiveness, leading to a broadband vibration attenuation. Subsequently, several studies have investigated the IA method's efficacy for low-frequency vibration attenuation of metamaterials (N.

M. M. Frandsen et al., 2016; Mizukami et al., 2021; Orta & Yilmaz, 2019; S. Wang et al., 2021; Xi et al., 2021; Xi et al., 2023; Yuksel & Yilmaz, 2020; Zeng, Cao, Wan, Guo, An, et al., 2022; Zeng, Cao, Wan, Guo, Wang, et al., 2022). Yuksel and Yilmaz (2020) designed a two-dimensional elastic metamaterial that features topologically optimized IA mechanisms, resulting in the achievement of an ultrawide low-frequency bandgap. Xi et al. (2021) proposed a four-bar IA mechanism to enhance the vibration attenuation capabilities of corrugated-core sandwich panels (CSPs) in low-frequency ranges. By comparing the IA-CSP with CSPs equipped with attached local resonators, it was observed that the IA-CSP exhibited a broader band of low-frequency attenuation. Bar-hinge resonators (triangular, x-type and pyramidal configurations) amplify inertia through the angle between the host structure and lateral bars. Achieving a lower frequency bandgap requires a larger amplification angle. In contrast, lever-type IA resonators achieve inertial amplification by adjusting the lever ratio, where a higher lever ratio results in a lower bandgap frequency. This eliminates the need for long lateral bars in sandwich cores, which occupy significant space for large amplification angles. This approach facilitates low-frequency bandgap generation while enhancing tunability and space efficiency for vibration control. Zeng et al. (2022) presented an innovative category of seismic metamaterials incorporating a lever-type IA system to attenuate the low-frequency seismic surface waves. Through experimental investigations, they thoroughly examined and discussed the vibration attenuation characteristics of a metamaterial plate equipped with lever-arm resonators. The obtained results clearly illustrated that the lever-type IA approach provides a viable means to isolate low-frequency seismic surface waves, thus offering an alternative solution in this domain. Then, Xi et al. (2023) introduced lever-type IA resonators into

a thin plate to improve its capabilities of attenuating low-frequency vibration. Compared to LR-type metamaterial plates with equivalent mass, the lever-type IA metamaterial plates exhibited significantly broader complete bandgaps at the desired target frequency. Sun et al. (2023) introduced a kind of metamaterial beam to enhance its ability to attenuate low-frequency flexural waves. The lever-type resonators were periodically installed on a host beam. The numerical results showed that the beam achieved a lower bandgap (97-160 Hz) than the LR-type metamaterial beam with identical additional mass. These findings highlight the superior effectiveness of the lever-type IA approach in achieving wider low-frequency bandgaps for vibration attenuation in thin plates.

2.4 Summary and Research Gap

This chapter reviews the previous studies related to the study of metamaterials, vibration control using LR-type metamaterials, and using IA mechanisms. The corresponding research gaps are summarized as follows:

1) The practical application of LR-type metamaterial sandwich plates in attenuating low-frequency vibrations faces significant challenges. Achieving a bandgap at low frequencies typically requires resonators with considerable mass, which accounts for a substantial portion of the total structural mass. However, incorporating such heavy resonators into compact sandwich structures introduces complex design constraints. A promising alternative is to integrate IA mechanisms into metamaterial design, enabling low-frequency vibration isolation with relatively

small masses. The bandgap frequency induced by IA mechanisms is primarily governed by the amplification angle—the deviation between the host structure and the lateral bars. Realizing low-frequency bandgaps requires a large amplification angle, which in turn demands long lateral bars. However, integrating such long bars is often impractical due to space limitations in real-world applications. This underscores the need to develop lightweight and compact IA-based designs capable of achieving efficient vibration attenuation at low frequencies within the geometric constraints of sandwich structures.

- 2) Although IA mechanisms offer a viable route to low-frequency vibration attenuation, their operational bandwidth is typically narrow, with optimal performance occurring near their resonance frequency. Lower bandgap frequencies tend to be associated with even narrower bandwidths, limiting their practical effectiveness. To address this, multi-bandgap mass-spring resonators have been proposed to achieve broader attenuation ranges. However, to the best of the authors' knowledge, metamaterial sandwich plates incorporating multi-bandgap inertial amplification resonators have not yet been explored. Achieving multiple bandgaps within the same structure not only enables coverage of distinct frequency ranges but also allows for potential merging and broadening of bandgaps, which is critical for broadband vibration suppression. This highlights the necessity of developing multi-frequency IA-MSPs as a new paradigm for enhanced broadband vibration attenuation.
- 3) In most existing designs, resonators are configured uniformly, which inherently limits the tunability of structural parameters and restricts the achievable bandgap range. This uniformity poses a major challenge in applications requiring flexible

control over multiple frequency ranges, thereby constraining the overall vibration control performance of metamaterial sandwich plates. To overcome these limitations, further research is needed to establish an innovative analytical framework coupled with an optimization-based design methodology. Such a framework should enable strategic control over bandgap characteristics through parametric modeling and optimization algorithms, ensuring that multiple bandgaps are precisely aligned with target frequency ranges. This advancement is essential for improving vibration suppression efficiency, enhancing structural performance, and expanding the adaptability of metamaterial sandwich plates in complex engineering environments.

Chapter 3

Low-frequency Vibration Control of the IA-MSP

In this chapter, a novel metamaterial sandwich plate incorporating lever-type inertial amplification resonators (IA-MSP) is developed to achieve low-frequency bandgaps and enhanced vibration attenuation. This marks the first application of lever-type IA mechanisms within a sandwich plate structure, where the amplification of resonator motion effectively increases the system's dynamic mass. As a result, the coupled mode frequency is significantly reduced, enabling the formation of low-frequency bandgaps without the need for large centralized masses or heavy local resonators. A comprehensive investigation of the IA-MSP's bandgap characteristics and vibration behavior is conducted through theoretical modeling, numerical simulations, and experimental validation. A dynamic model is established to mathematically describe the inertial amplification mechanism and its influence on the system's dynamic response. Vibration transmission analyses confirm that the lever-type configuration significantly amplifies mass motion, leading to increased effective mass and enhanced low-frequency isolation. Moreover, by adjusting the lever ratio R, the bandgap boundaries can be finely tuned. Compared to conventional LR-based metamaterial sandwich plates (LR-MSP) with identical geometric and material parameters, the IA-MSP with R = 2 exhibits bandgap boundaries that are approximately half those of the LR-MSP. As R increases, the lower boundary of the bandgap continues to decrease, resulting in a clear shift of the bandgap towards lower frequencies.

3.1. Methodology

This section presents the study's methodology, which explains the strategies and accordance adopted to obtain the objectives of the preliminary study. In the first subsection, the section presents theoretical derivation of the dynamic model, revealing the IA mechanism in the proposed plate theoretically. Then, it outlines the FEM employed for calculating the band structure, which provides the foundation for the following investigations. Finally, the experiment test is introduced including the experimental setup and experimental specimen of an IA-MSP.

3.1.1 Theoretical Derivation

The proposed IA-MSP and its unit cell are presented in Figures 3.1 (a) and (b), respectively. Two face plates are connected by a periodic array of support bars, with lever-type inertial amplification resonators periodically integrated between them. Each resonator comprises a spring, a lever, and a mass, all connected to the support bar by a hinge joint. In this study, the analysis focuses only on the transverse vibration of the IA-MSP, with the assumption that the supporting bars possess infinite stiffness.

To reveal the lever-type inertial amplification mechanism, the IA-MSP unit cell is analytically described by equivalent mass-lever-spring model, as shown in Figure 3.1 (c). k denotes the spring stiffness, m represents the mass, and l_1 and l_2 are the distance between the spring and support bar and between the support bar and the mass, respectively. According to the classical plate theory, the strain-displacement correlations at a point (x, y, z) of two face plates are expressed as follows:

$$\left\{\varepsilon_{x}, \varepsilon_{y}, \gamma_{xy}\right\}^{T} = \left\{-z\frac{\partial^{2} w}{\partial x^{2}}, -z\frac{\partial^{2} w}{\partial y^{2}}, -2z\frac{\partial^{2} w}{\partial x \partial y}\right\}^{T}$$
(3.1)

where ε_x represents the strain in the x-direction, ε_y represents the strain in the y-direction, γ_{xy} represents the shear strain, and w denotes the transverse displacement of the plate.

The constitutive relation of the plate in the context of a plane stress problem is defined as:

$$\sigma = \mathbf{Q}\varepsilon, \tag{3.2}$$

where **Q** denotes the elastic constants matrix, which can be expressed as:

$$\mathbf{Q} = \begin{bmatrix} Q_{11} & Q_{12} & 0 \\ Q_{21} & Q_{22} & 0 \\ 0 & 0 & Q_{66} \end{bmatrix}, \tag{3.3}$$

where

$$Q_{11} = Q_{22} = \frac{E}{1 - v^2}, Q_{12} = Q_{21} = \frac{vE}{1 - v^2}, Q_{66} = \frac{E}{2(1 + v)},$$
 (3.4)

The elastic strain energy U and the kinetic energy T associated with the face plates are expressed as follows:

$$U = \frac{1}{2} \int_{V} \{\varepsilon\}^{\mathrm{T}} \{\sigma\} \mathrm{d}V, \tag{3.5}$$

$$T = \frac{1}{2} \int_{V} \rho \left(\frac{\partial w}{\partial t}\right)^{2} dV, \tag{3.6}$$

where ρ and V denote the density and volume of face plates.

To elucidate lever-type inertial amplification mechanism of the resonator, an analysis of the resonator's dynamic problem is conducted, and the motion of mass within the resonator is depicted in Figure 3.1 (d) for clarity. The terms w_1 and w_0 are the transverse displacement of mass and support bar, respectively. The assumption is made that the lever is rigid and devoid of mass. Therefore, the kinetic energy T_r and the elastic strain energy T_r of the inertial amplified resonator are given as follows:

$$T_r = \frac{1}{2}m\dot{w}_1^2, (3.7)$$

$$U_r = \frac{1}{2}k\left(\frac{w_1}{R} - w_0\right)^2,\tag{3.8}$$

where *R* represents the lever ratio, which can be obtained by $R = l_2 / l_1$.

In the context of elastic wave propagation within unbounded acoustic metamaterial plates comprising a periodic unit cell, it is postulated that the displacements of the face plates (w), the support bar (w_0) , and the mass (w_1) can be posited to manifest in the ensuing expressions:

$$w=Ae^{i(\alpha x+\beta y-\omega t)}, \ w_0=Ae^{-i\omega t}, \ w_1=Be^{-i\omega t},$$
 (3.9)

where α and β denote the wavenumbers in the x- and y- directions, ω is the wave frequency, and A and B denote unknown displacement amplitudes. This study is dedicated to the exclusive investigation of low-frequency vibrations. It is hypothesized that the wavelength substantially exceeds the length of the resonator, thereby leading to the omission of any phase disparity between w_0 and w_1 . When only considering the

resonator system (spring-lever-mass system), the transverse displacement of the support bar w_0 is assumed to be zero. The principle of conservation of mechanical energy is then formulated as follows:

$$T_r - U_r = 0.$$
 (3.10)

By substituting Eqs (3.7)-(3.9) into Eq. (3.10), the resonance frequency of the inertial amplified resonator is calculated as follows:

$$f = \frac{1}{2\pi} \sqrt{\frac{k}{R^2 m}}. (3.11)$$

To obtain the equations governing the behavior of the metamaterial plate, Hamilton's principle is utilized as follows:

$$\int_0^t (\delta T - \delta U + \delta T_r - \delta U_r) = 0.$$
(3.12)

By substituting Eq. (3.9) into Eq. (3.12), the ensuing set of algebraic equations is derived:

$$\left[\frac{8\sin\left(\frac{\alpha a_{x}}{2}\right)\sin\left(\frac{\beta a_{y}}{2}\right)}{\alpha\beta}\left[\rho h\omega^{2} - \frac{\left(H^{3} - h^{3}\right)}{3}\left(Q_{11}\alpha^{4} + 2Q_{12}\alpha^{2}\beta^{2} + Q_{22}\beta^{4} + 4Q_{66}\alpha^{2}\beta^{2}\right)\right] - \frac{k}{R^{2}} \qquad \frac{k}{R^{2}} \\
\frac{k}{R^{2}} \qquad m\omega^{2} - \frac{k}{R^{2}}\right] \begin{Bmatrix} A \\ B \end{Bmatrix} = 0,(3.13)$$

where H denotes the overall height of the structure, and h denotes the thickness of face plates. Eq (3.13) indicates that non-zero solutions for A and B are present only when the determinant of the matrix equals zero:

$$\left(m\omega^{2} - \frac{k}{R^{2}}\right) \left\{ \frac{8\sin\left(\frac{\alpha a_{x}}{2}\right)\sin\left(\frac{\beta a_{y}}{2}\right)}{\alpha\beta} \left[\rho h\omega^{2} - \frac{\left(H^{3} - h^{3}\right)}{3}\left(Q_{11}\alpha^{4} + 2Q_{12}\alpha^{2}\beta^{2} + Q_{22}\beta^{4} + 4Q_{66}\alpha^{2}\beta^{2}\right)\right] - \frac{k}{R^{2}} \right\} - \frac{k^{2}}{R^{4}} = 0,$$
(3.14)

The ω is determined by solving Eq. (3.14) for the values of α and β . The lower boundary of the bandgap corresponds to ω when α and β approach zero, while the upper boundary of the bandgap corresponds to ω when α and β approach infinity. When wave frequencies at boundaries of the bandgap are divided by 2π , the bandgap is expressed as follows:

$$\left(\frac{1}{2\pi}\sqrt{\frac{k}{R^2m}}, \frac{1}{2\pi}\sqrt{\frac{k}{R^2m}} + \frac{k}{2R^2a_xa_y\rho h}\right),$$
 (3.15)

where a_x and a_y denote lattice constants along the x and y direction, and $2a_xa_y\rho h$ represents the mass of two faceplates in the unit cell. In Eq. (3.15), the first term corresponds to the resonance frequency. The mass ratio of the resonator to the faceplates is expressed as $\gamma = m/2a_xa_y\rho h$. The bandgap is reformulated as follows:

$$\left(\frac{1}{2\pi}\sqrt{\frac{k}{R^2m}}, \frac{1}{2\pi}\sqrt{\frac{k}{R^2m}}\sqrt{1+\gamma}\right). \tag{3.16}$$

Assuming the lever is rigid and massless, the inertial mass can be amplified by a factor of R^2 , and resonance frequency will be reduced by a factor of R. It is evident that enlarging the value of R can enhance the effect of inertial mass amplification and obtain a lower resonance frequency. In addition, obtaining a low resonance frequency can also be achieved by using a small spring stiffness or a large mass. However, the resonator

mass is limited, and soft materials used for the spring section are not durable in practical engineering applications. Therefore, adjusting the fulcrum position is a superior approach to amplify the movement of small masses and achieve low-frequency vibration attenuation.

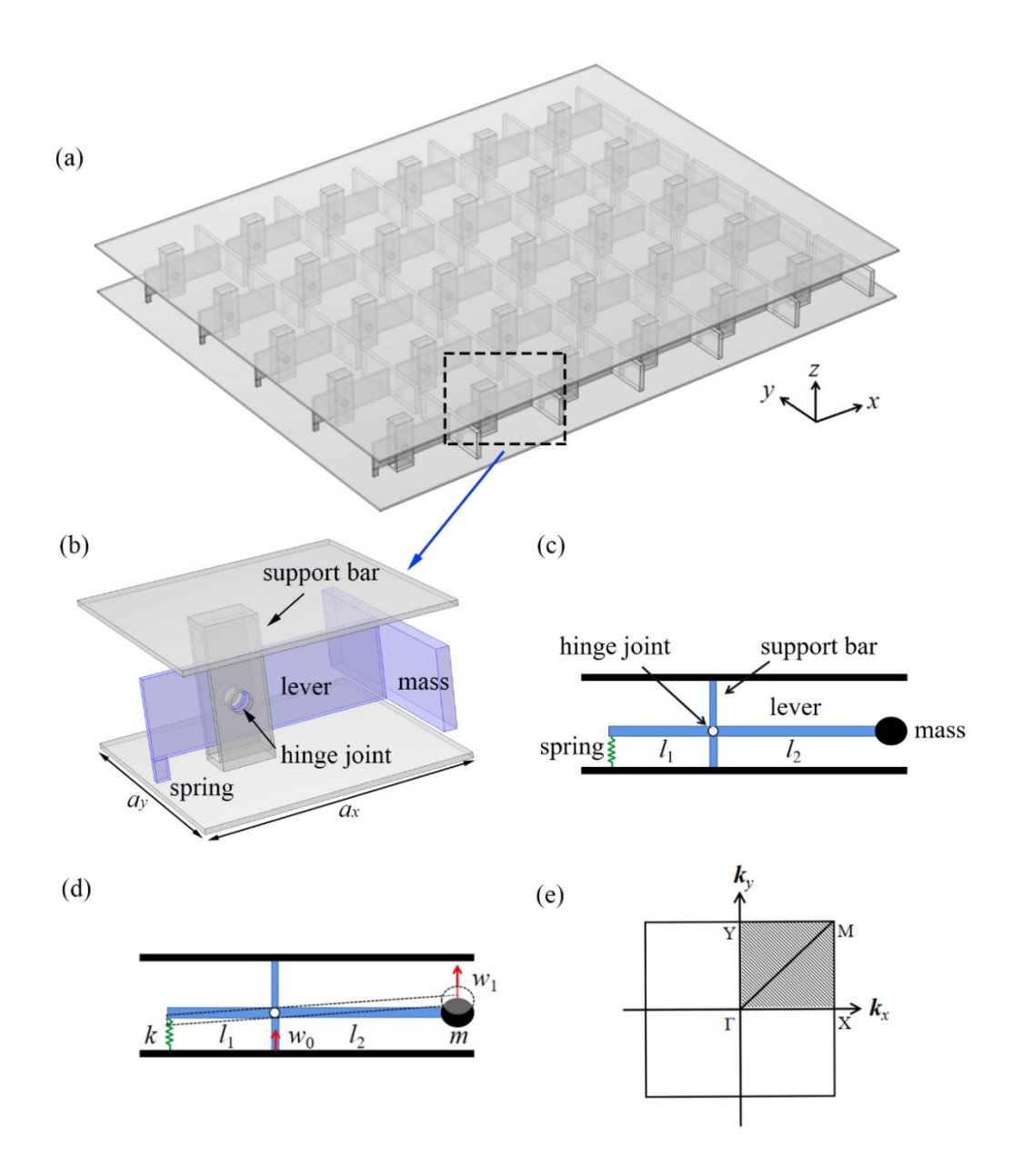


Figure 3.1 (a) The schematic diagram of IA-MSP. (b) The unit cell of IA-MSP. (c) The simplified model of the unit cell of IA-MSP. (d) The displacements of the spring-lever-

mass system. (e) The irreducible Brillouin zone (grey zone) and sweeping direction of wave vectors (M- Γ -X-M-Y- Γ).

3.1.2 Band Structure Calculation by Finite Element Method

The band structure serves as a framework for comprehending the physical characteristics of metamaterials structures. The governing equation that describes the propagation of elastic waves in solids is mathematically formulated as follows

$$\nabla \cdot (\mathbf{C}(\mathbf{r}) : \nabla \mathbf{u}(\mathbf{r})) = \rho(\mathbf{r}) \frac{\partial^2 \mathbf{u}(\mathbf{r})}{\partial t^2}, \tag{3.17}$$

where ∇ denotes the differential operator, $\mathbf{r} = (x, y, z)$ denotes the position vector, $\mathbf{C}(\mathbf{r})$, $\mathbf{u}(\mathbf{r})$ and $\rho(\mathbf{r})$ denotes the position dependent elastic tensor, displacement vector and mass density, respectively. t denotes the time. According to the Bloch-Floquet theorem, the displacement vector in Eq. (3.17) is expressed as:

$$\mathbf{u}(\mathbf{r},t) = e^{i(\mathbf{k}\cdot\mathbf{r}-\omega t)}\mathbf{u}_{\mathbf{k}}(\mathbf{r}), \tag{3.18}$$

where k denotes the Bloch-Floquet wave vector, ω represents the angular frequency, and $\mathbf{u}_{k}(\mathbf{r})$ represents the modulation function of the displacement, which characterizes the periodic behavior within the unit cell:

$$\mathbf{u}_{k}(\mathbf{r}) = \mathbf{u}_{k}(\mathbf{r} + \mathbf{a}), \tag{3.19}$$

where $\mathbf{a} = (a_x, a_y)$ denotes the lattice constant vector, a_x and a_y denote lattice constants along the x and y direction. By substituting Eq. (3.19) into (3.18), the periodic displacement boundary condition is yielded:

$$\mathbf{u}(\mathbf{r} + \mathbf{a}, t) = e^{i\mathbf{k}\cdot\mathbf{a}}\mathbf{u}(\mathbf{r}, t). \tag{3.20}$$

Combining the Eq. (3.17) and (3.20), the dispersion relation of the system is transformed into the eigenvalue equation:

$$(\Omega(\mathbf{k}) - \omega^2 \mathbf{M}) \cdot \mathbf{u} = 0, \tag{3.21}$$

where $\Omega(\mathbf{k})$ and \mathbf{M} represent the stiffness and mass matrices, respectively. Periodic boundary conditions are employed along edges of face plates of the unit cell. By varying the wave vector \mathbf{k} along the boundaries of irreducible Brillouin zone as shown in Figure 3.1 (e), the band structure of unit cell and resonance eigenmodes are calculated using characteristic frequency analysis with the FEM. In the computed band structure, a bandgap is defined as a frequency range lacking corresponding eigenvalues.

3.1.3 Experimental Study

A vibration experiment is carried out to investigate the vibration attenuation capabilities of IA-MSP in this study. Figure 3.2 illustrates the experimental specimen of an IA-MSP consisting of 6 × 5 unit cell. To facilitate the preparation of experimental specimen, all components including the spring, lever, mass, support bar, and faceplate are fabricated using steel material. In this experimental specimen, the supporting bar and lever are hinged together by a bolt that passes through the holes. The supporting bars and face plates, face plates and springs, levers and masses, levers and springs are all connected by laser welding. Figure 3.3 depicts the experimental setup for the vibration test. The two short edges of the plate are clamped to the foundation, while the remaining two edges are unconstrained. The excitation perpendicular to the face plate

is generated through a KISTLER type 9276A force hammer. The vibration acceleration is sampled by the Brüel & Kjær type 4394 accelerometer and recorded by the Brüel & Kjær Pulse 3160. The measured acceleration vibration signal is represented as a time-domain signal. The Fast Fourier Transform (FFT) analysis module in Pulse is capable of performing a rapid Fourier transformation on time domain data, enabling frequency spectrum analysis to obtain the vibration characteristics of the IA-MSP.

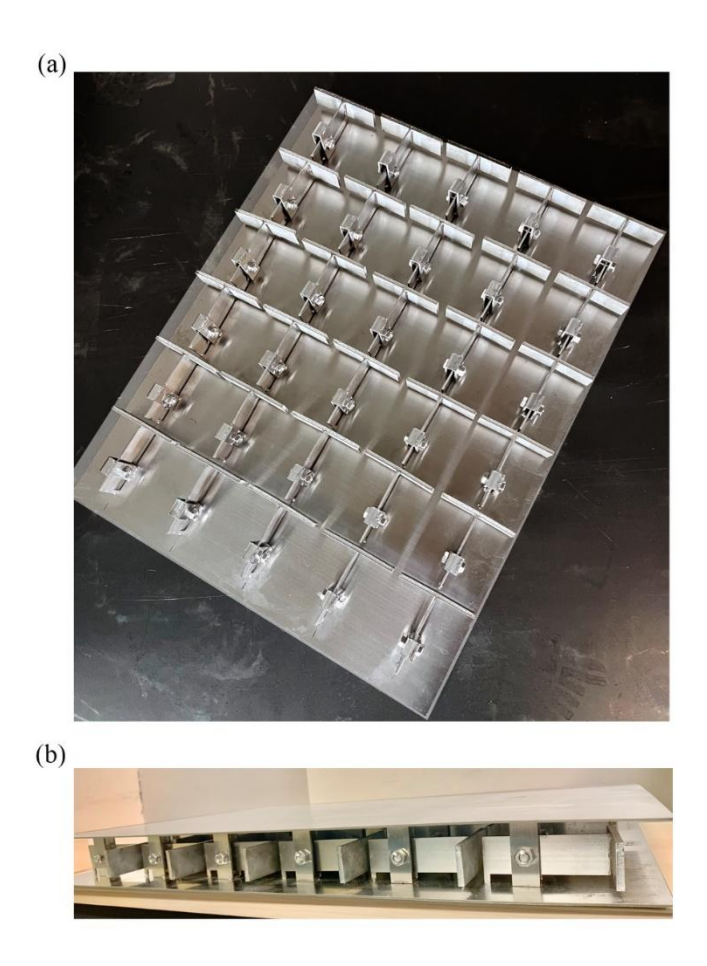


Figure 3.2 The experimental specimen of an IA-MSP with 6×5 unit cells: (a) without upper face plate; (b) global photo.

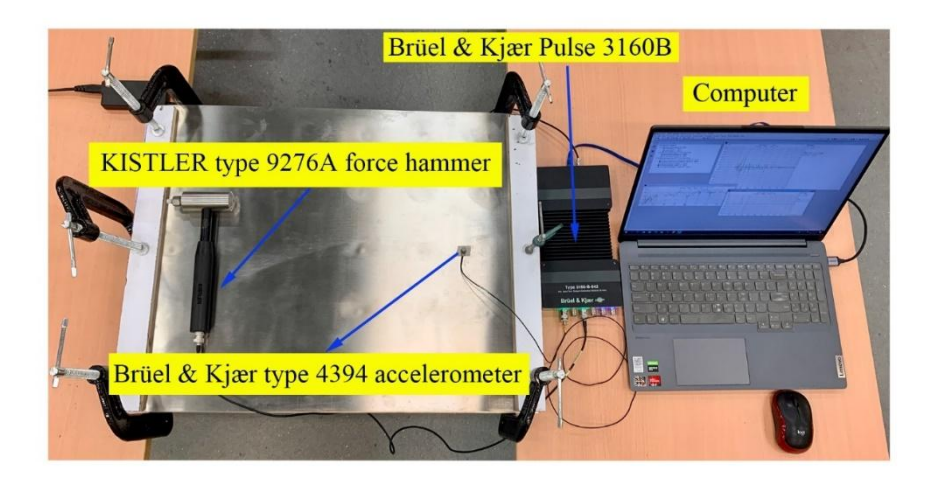


Figure 3.3 The experimental setup of the vibration test.

3.2. Results and Discussions

This section primarily encompasses three components. Firstly, the band structure of the unit cell is calculated, the mechanism of bandgap generation is elucidated through the analysis of eigenmodes, and theoretical predictions are further validated by the numerical results. Subsequently, transmission and vibration characteristics of the IA-MSP with 6×5 unit cells are investigated through numerical simulations. Finally, the experiment is carried out, and a normalized comparison is performed to quantitatively evaluate the vibration attenuation capability and lightweight design of the IA-MSP and other kinds of reported metamaterials sandwich plates.

3.2.1 Band Structure and Mechanisms

This subsection analyzes the band structure of the IA-MSP unit cell and explores the generation mechanism of low-frequency bandgap. Currently, the term "low frequency"

lacks a precise definition. This study concentrates on subwavelength frequency vibrations and defines "low frequency" as the range where the unit cell size is considerably smaller than the elastic wave wavelength (Xi et al., 2021). In the unit of the IA-MSP, both a_x and a_y have the same value of 10 cm, represented as a, the face plate's thickness h is 2 mm, l_1 is 0.25 a, l_2 is 0.50 a, and other geometrical parameters and materials parameters of IA-MSP have been presented in Tables 3.1 and 3.2. The band gap outcomes obtained via FEM are computed utilizing COMSOL Multiphysics 5.6 software, employing characteristic frequency analysis. The refined tetrahedral meshes are applied to the support bar, while the remaining part of the structure is meshed with refined swept meshes. The mesh's precision has been verified through a mesh convergence study. Figure 3.4 presents the band structure of IA-MSP (represented by dotted black lines) and the eigenfrequencies of the inertial amplified resonator (represented by dashed red lines). The bandgap exists in the grey zone (51-80 Hz), where the eigenvalues are absent. To explore the generation mechanism of bandgap, the eigenmode shapes A-C of the inertial amplified resonator, the coupled eigenmode shapes D and E, and the coupled mode shapes F and G of the IA-MSP are presented in Figure 3.4.

Figure 3.4 presents that the vibration deformation of mode shapes D and E, which correspond to horizontal dotted black lines, mostly occur in the inertial amplified resonator, whereas the deformation of the face plates is neglectable. Therefore, these mode shapes are referred as coupled eigenmode shapes. Notably, the dashed red line, indicating the eigenfrequencies of the inertial amplified resonator, mostly coincides with horizontal dotted black lines, which denote the coupled eigenmode shapes of the IA-MSP. Furthermore, the eigenmode shapes of the inertial amplified resonator 31

coincide with the coupled eigenmode shapes of the IA-MSP. For instance, eigenmode shape A corresponds to coupled eigenmode shape D, and eigenmode shape B corresponds to coupled eigenmode shape E. However, there is no corresponding coupled eigenmode with the eigenmode shape C of the inertial amplified resonator. Specifically, there is no horizontal dotted black line coinciding with the dashed red line of eigenfrequency 52 Hz, which corresponds to the mode shape C. Notably, mode shape F illustrates that vibration deformation mainly occurs in the mass, and mode shapes of the inertial amplified resonator are similar to the eigenmode shape C. The lower boundary of bandgap is determined by the coupled mode F, which are in correspondence with the eigenmode shape C. The upper boundary of bandgap is determined by the coupled mode G, the vibration deformation mostly occurs in the lever near the spring, and the face plates are also deformed. Modes G are coupled modes of the out-of-plane vibration mode of the face plate and the vibration mode of the inertial amplified resonator.

To further elucidate the bandgap formation mechanism induced by the inertial amplified resonator, acceleration integrations P of eigenmode shape A-C of the inertial amplified resonator in the z direction are calculated. The acceleration integration P can be expressed as (Q. Wang et al., 2021):

$$P = \rho \iiint a(x, y) dx dy dz, \qquad (3.22)$$

where ρ denotes the density of the inertial amplified resonator, a(x, y) denotes the acceleration of the resonant mode shape of the inertial amplified resonator in the z direction at point (x, y). The acceleration integration P is compared without a specific

value, and a non-zero value of P indicates the main structure is subjected to a reaction force, which contributes to a coupling effect of the out-of-plane vibration of face plates and the resonant vibration of the inertial amplified resonator. Through the calculations, the P value of the eigenmode shape C is non-zero, and this mode shape precisely leads to the locally resonant bandgap. On the contrary, the acceleration integration of the other eigenmode shapes is zero, indicating no reaction force is acting on the face plates, and no coupling effect occurs on the structure. Therefore, it is essential to obtain the eigenmode shape with non-zero acceleration for generating the locally resonant bandgap at low frequencies. Moreover, the hinge joint in the IA-MSP is favourable for transmitting a reaction force between the resonator and face plates and amplifying the resonator's mass, which results in obtaining the locally resonant bandgap at a low-frequency range.

Table 3.1 Geometrical parameters of IA-MSP. (a = 0.1 m)

Structure	Length, width, and height
Mass	$0.100a \times 0.900a \times 0.300a$
Lever	$0.750a \times 0.025a \times 0.300a$
Spring	$0.050a \times 0.025a \times 0.080a$
Support bar	$0.200a \times 0.200a \times 0.530a$

Table 3.2 Material parameters

Structure	Young's modulus (GPa)	Poisson ration	Density (kg/m ³)
Mass (steel)	200	0.30	7850

Spring (rubber)	0.05	0.47	1300	
Face plates, lever and	70	0.33	2700	
support bar (aluminum)				

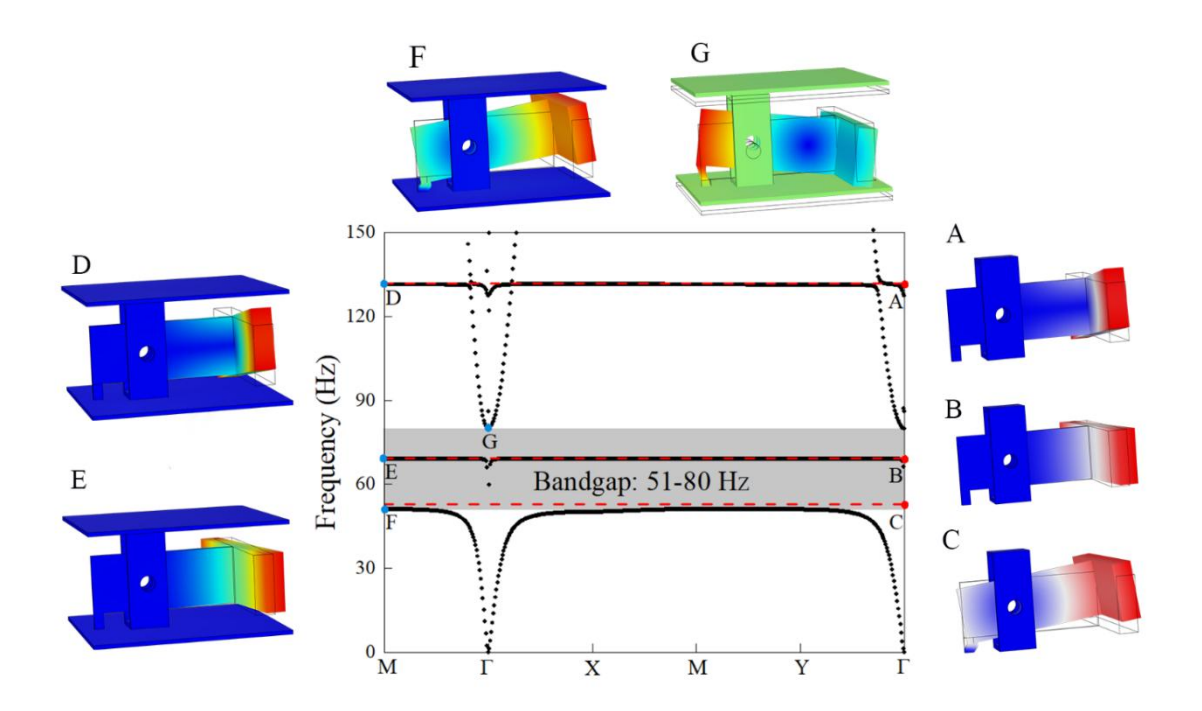


Figure 3.4 Band structure of IA-MSP (dotted black line) and eigenfrequencies of the inertial amplified resonator (dashed red line).

To validate the accuracy of the numerical results presented above, the numerically computed boundaries of the bandgap are compared with the theoretical predictions, as presented in Figure 3.5. Each plot in the analysis varies only a single parameter, while keeping the other geometrical and material parameters constant shown in Tables 3.1 and 3.2. As shown in Figure 3.5, the theoretical predictions exhibit a remarkable concurrence with the simulated boundaries of the bandgap across all instances. As described in subsection 3.1.1, increasing the lever ratio *R* of the inertial amplified resonator can result in an inertial mass amplified effect, which leads to a lower 34

resonance frequency. Figure 3.5 (a) presents the influence of R on the bandgap of IA-MSP. The overall length of the lever remains constant at 0.75a, the support bar position remains constant, and the resonator position varies, leading to variations in the lever ratio R. The results show that increasing the R leads to a reduction in both the lower (f_l) and upper (f_u) boundaries of the bandgap. Consistent with Eq. (3.16), an elevated value of R induces a decline in the resonant frequency of inertial amplified resonator, causing the bandgap to move towards lower frequencies. Figure 3.5 (b) shows the bandgap with varying mass ratios of resonator r_{ρ} . The r_{ρ} is defined as $r_{\rho} = \rho_m/\rho_1$, where ρ_m denotes a varying mass density of the inertial amplified resonator, and $\rho_1 = 7850 \text{ kg/m}^3$ is the initial mass density of the inertial amplified resonator. The results demonstrate a downward shift in the f_l and f_u of the bandgap, accompanied by an expansion in the bandgap width as r_{ρ} increases. According to Eq. (3.16), the bandgap boundaries are sensitive to the resonator mass. As the resonator mass increases, a decrease in the resonance frequency is observed, while the mass ratio γ of the resonator to faceplates experiences an increment. Consequently, this results in a shift of the bandgap to lower frequencies and the attainment of a broader bandgap. Figure 3.5 (c) illustrates the depiction of the bandgap variation corresponding to the alteration of the spring stiffness ratio of the resonator. The r_E is characterized by $r_E = E_s/E_1$, where E_s is a varying Young's modulus of the resonator spring, and $E_1 = 0.05$ GPa is the initial Young's modulus of the resonator spring. The findings clearly demonstrate that increasing the value of r_E leads to a substantial rise in both f_l and f_u of the bandgap in the IA-MSP. This observation aligns with the theoretical prediction stated in Eq. (3.16), which suggests that a decrease in stiffness corresponds to a lower bandgap. Figure 3.5 (d) depicts the influence of faceplate mass on the bandgap behavior of the IA-MSP. The

 $r_{\rho f}$ is defined as $r_{\rho f} = \rho_f/\rho_2$, where ρ_f denotes a varying density of the face plate, and ρ_2 = 2700 kg/m³ is the initial faceplate density. It is evident that the f_l remains constant, as it is not affected by the mass of the face plates. However, the f_u of the bandgap decreases as $r_{\rho f}$ increases, in accordance with Eq. (3.16).

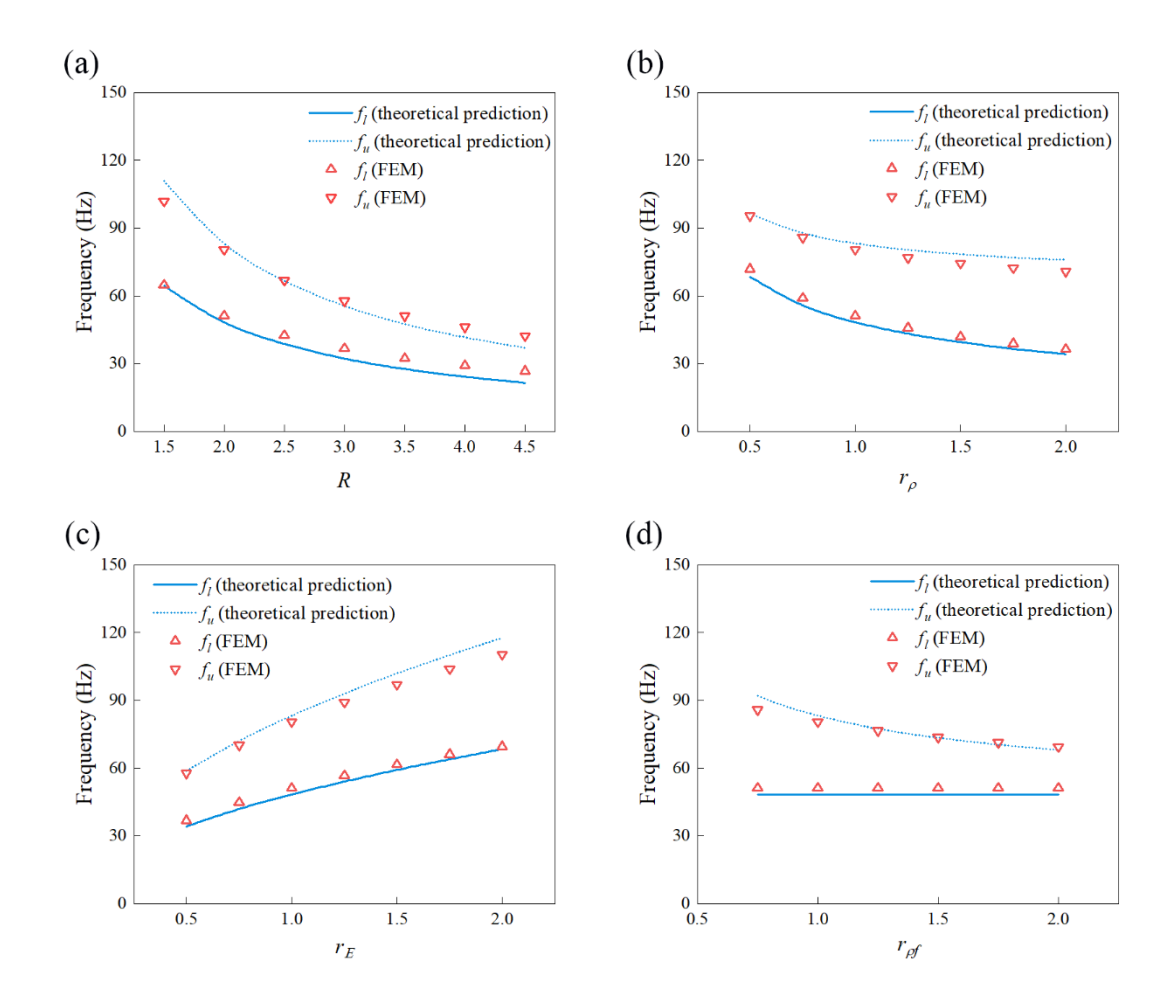


Figure 3.5 Bandgap boundaries of the IA-MSP derived through theoretical prediction and numerical simulation (FEM): (a) boundary frequencies with R, (b) boundary frequencies with r_{ρ} , (c) boundary frequencies with r_{E} , (d) boundary frequencies with $r_{\rho f}$. Moreover, the LR-MSP consisting of the same plates, springs and masses as the IA-MSP is introduced for comparison. The unit cell of LR-MSP and the simplified model

are depicted in Figures 3.6 (a) and (b), respectively. To ensure a reasonable comparison, the geometrical and materials parameters of the support bar, spring and mass in the LR-MSP are identical to those of the IA-MSP. Moreover, the mass of the lever is attached to the faceplates. Figure 3.6 (c) presents the band structure of LR-MSP. A bandgap is observed to span from 103-164 Hz. The mode associated with the lower bandgap boundary is induced by the coupled effect of face plates and resonators. Comparing the bandgap of the LR-MSP with equal mass (103-164 Hz), the bandgap position of the IA-MSP (51-85 Hz) is lower than that of the LR-MSP. The bound frequencies of the IA-MSP with an R-value of 2 are half of those observed in the LR-MSP (equivalent to the IA-MSP with an R-value of 1). This agreement with the theoretical prediction outlined in Eq. (3.16) further reinforces the consistency of the obtained results. The superiority of achieving lower bandgap for the IA-MSP is attributed to the lever-type inertial amplified mechanism. The lever-type inertial amplified resonator in IA-MSP is capable of generating significant inertial forces through the amplification of mass motion, thereby increasing the effective system mass. As a consequence, the resonance frequency and the frequency associated with the coupled mode are reduced, resulting in a strong capability of the IA-MSP to obtain a low-frequency bandgap. However, it is evident that the width of the bandgap of the LR-MSP is broader compared to that of the IA-MSP, which is an inevitable result. A lower bandgap frequency range tends to be accompanied by a narrower bandgap width. The bandgap width can be expanded by increasing material damping or using different kinds of unit cells (Fan et al., 2022; Jingiang Li et al., 2020).

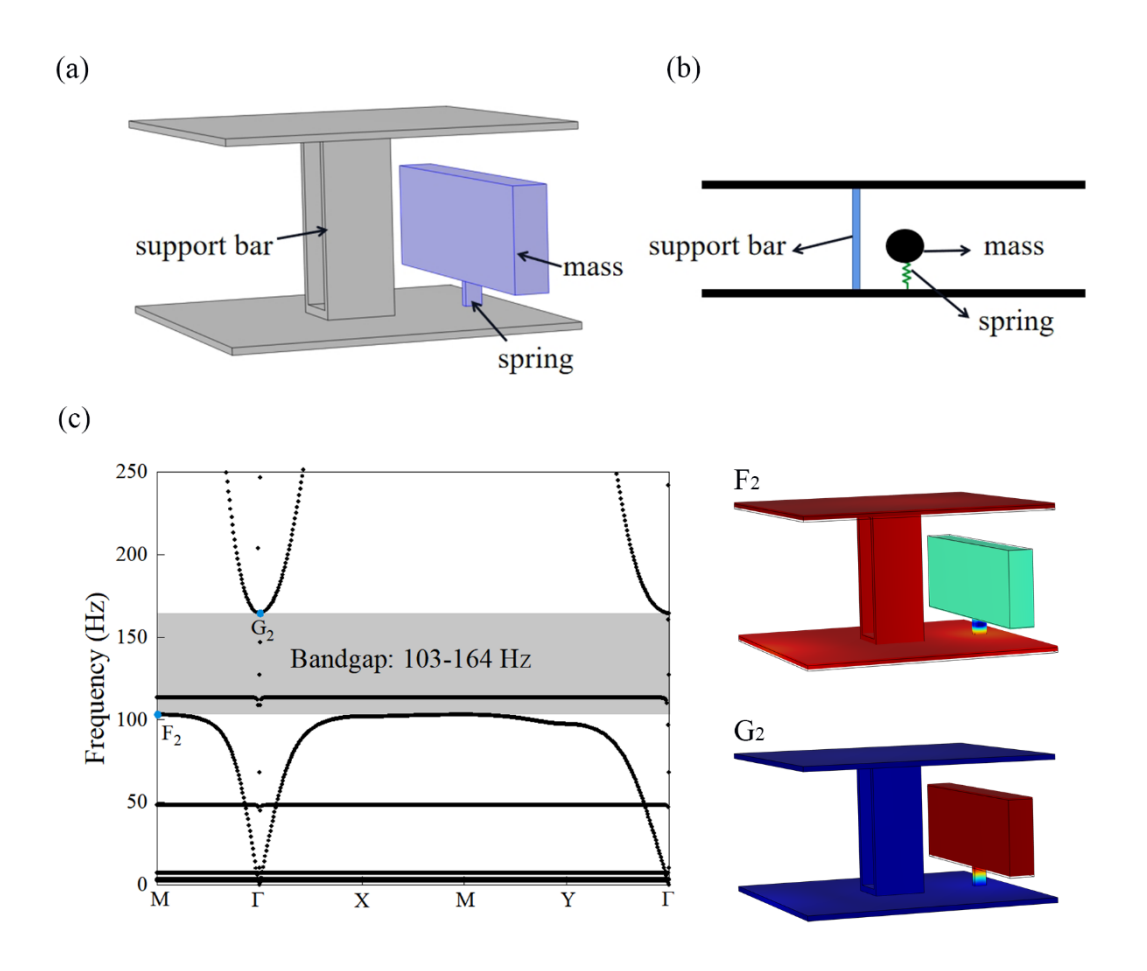


Figure 3.6 (a) The unit cell of LR-MSP. (b) The simplified model of LR-MSP unit cell. (c) The band structure of LR-MSP and the vibration mode shapes associated with the lower and upper boundary frequency.

3.2.2 Vibration Transmission Research of the IA-MSP

In this subsection, an investigation on vibration transmission is carried out to examine the vibration attenuation capabilities of IA-MSP. The COMSOL Multiphysics software is employed for modelling and calculation. The geometric and material parameters of IA-MSP including the mesh generation, are identical to those mentioned previously. The IA-MSP structure, as depicted in Figure 3.7, features clamped boundaries on its

two shorter edges (highlighted by the red boundaries), while the remaining two edges (illustrated by the blue boundaries) are left unconstrained. The frequency-domain analysis applies a harmonic point load of constant 1 N amplitude (0° phase) across 0-150 Hz at Point A (100 mm, 250 mm, 57 mm) on the upper face plate, corresponding to the frequency response function (FRF) calculation under uniform spectral excitation. The resulting acceleration response is measured at point B (500 mm, 250 mm, 57 mm), with a frequency interval of 0.5 Hz. Figure 3.8 displays the acceleration response of the IA-MSP at a lever ratio R of 2, compared with that of a sandwich plate without resonators. The vibration attenuation capabilities of the IA-MSP are clearly evident within a frequency range of 50-80 Hz, demonstrating significant reduction in vibration compared with the sandwich plate without resonators. A grey area in Figure 3.8, where the acceleration decreases significantly, is referred to as the attenuation zone (AZ). The location and width of the AZ are observed to coincide with that of the bandgap predicted theoretically and numerically.

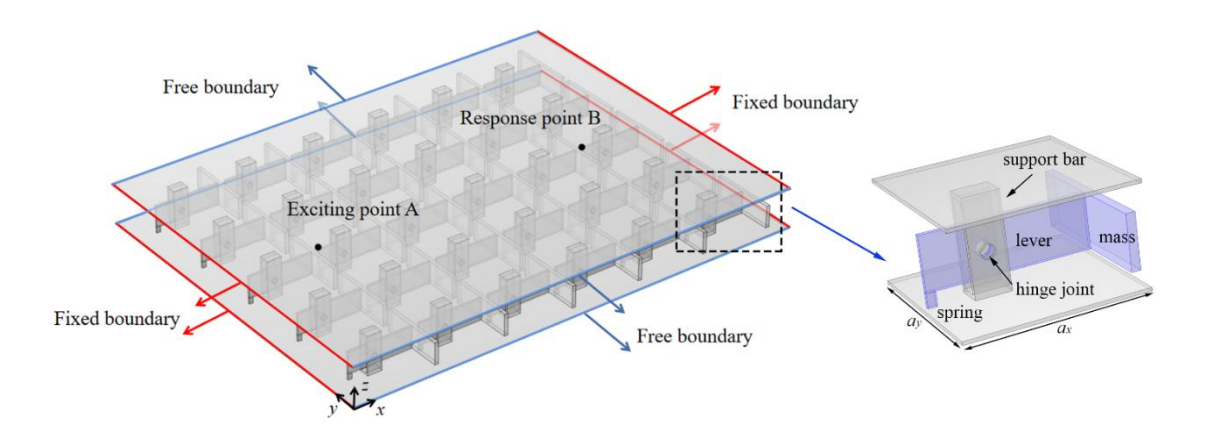


Figure 3.7 The model of the IA-MSP with 6×5 unit cells and boundary conditions.

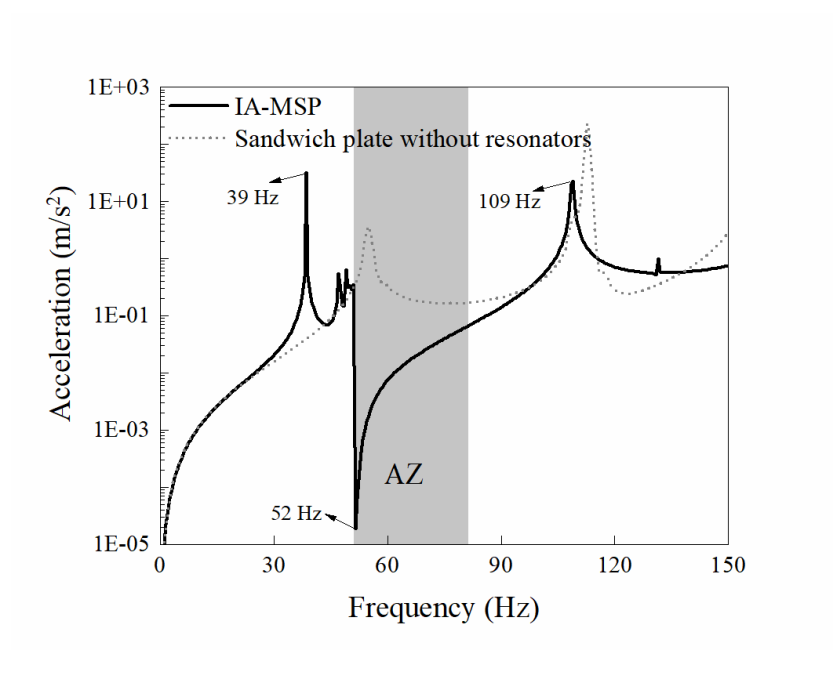


Figure 3.8 The acceleration response of the IA-MSP (R = 2) and sandwich plate without resonators.

To further illustrate the efficacy of IA-MSP in attenuating vibrations in bandgap, the computed vibration shapes of IA-MSP at different excitation frequencies are illustrated in Figure 3.9. The figures clearly present the distribution of vibration across the plate for different excitation frequencies. Specifically, Figures 3.9 (a) and (c) indicate that vibrations are distributed throughout the entire plate during excitation within the passband (39 and 109 Hz). In contrast, Figure 3.9 (b) shows that the vibration energy centralizes around the excitation point when the excitation frequency falls within the bandgap (52 Hz). It can be attributed to the proximity of the excitation frequency to the eigenfrequency of the inertial amplified resonator corresponding to the mode C in Figure 3.4. As a result, the resonance of inertial amplified resonator is motivated, resulting in a reaction that resists the excitation and is exerted on the face plate. This reaction causes a significant attenuation of plate vibrations within the bandgap range.

Moreover, a comparative analysis is undertaken to validate the superiority of the lowfrequency vibration attenuation property of IA-MSP. Figure 3.10 compares the vibration responses at point B between the IA-MSP with a lever ratio R of 2 and the LR-MSP, both consisting of 6×5 unit cells, subject to identical excitation conditions. The LR-MSP shares identical geometrical parameters, material parameters, and boundary conditions with the IA-MSP. As depicted in Figure 3.10, the frequency range encompassing the AZ of the LR-MSP exhibits a close proximity to the bandgap range depicted in Figure 3.6 (c) (103-164 Hz). Due to the lever-type IA mechanism, the AZ of IA-MSP is substantially lower than that of the LR-MSP, as presented in Figure 3.10. The AZ range of IA-MSP is observed to be half as low as that of the LR-MSP. Figure 3.11 presents the acceleration response of the IA-MSP at different R-values. The overall length of the lever remains constant at 0.75a, the support bar position remains constant, and the resonator position varies, leading to variations in the lever ratio R. The relationship between the lever ratio R and the position of the AZ is evident, with a higher R value leading to a noticeable shift of the AZ towards lower frequencies. This observation implies that, under a constrained mass condition, adjusting the R value allows for achieving a lower bandgap, thereby significantly enhancing the ability of metamaterial sandwich plate to attenuate low-frequency vibrations.

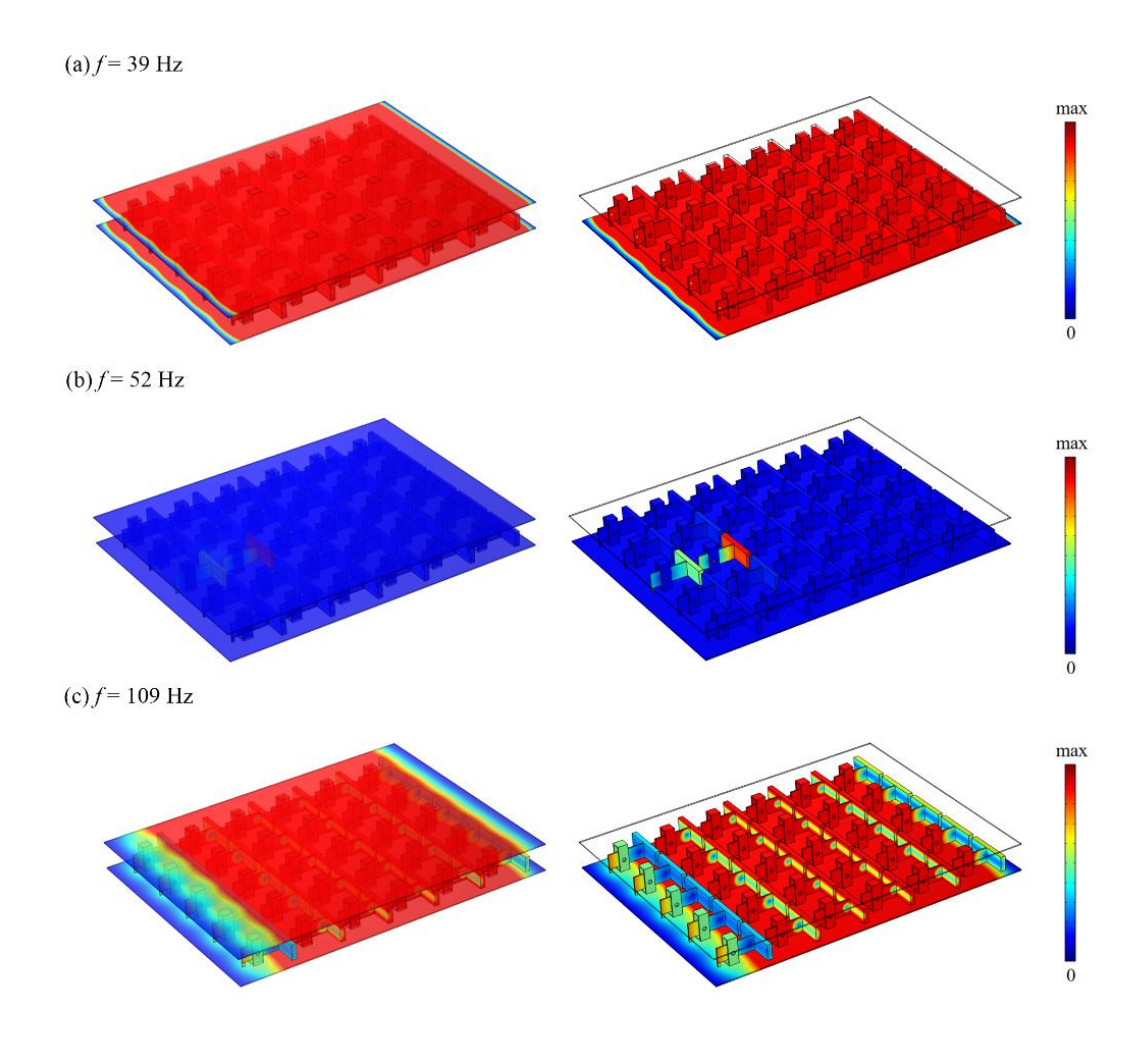


Figure 3.9 Vibration modes of the IA-MSP (R = 2) at different excitation frequencies: (a) f = 39 Hz; (b) f = 52 Hz; (c) f = 109 Hz.

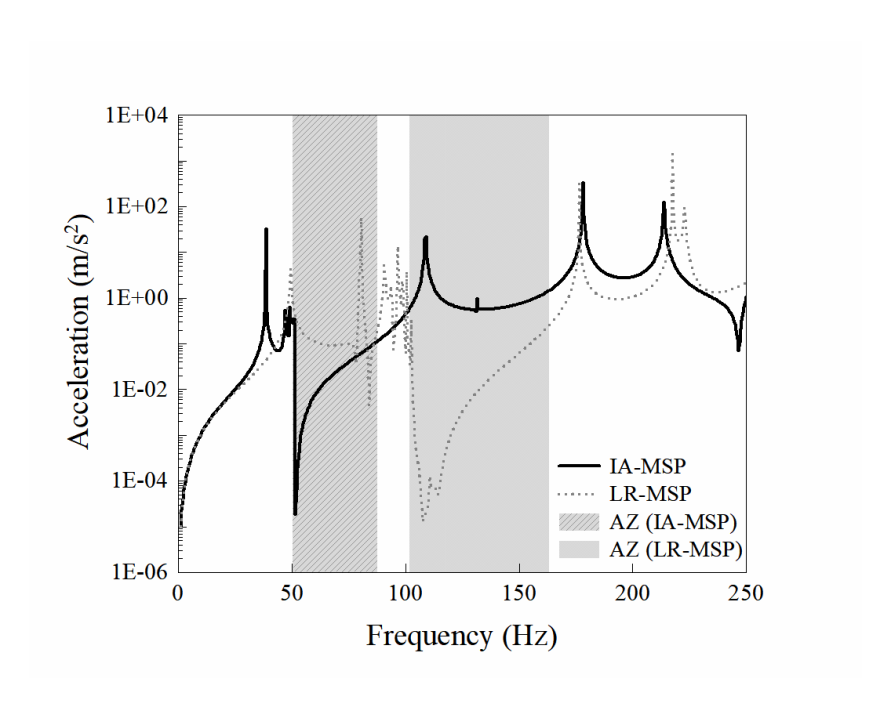


Figure 3.10 The acceleration response of the LR-MSP and IA-MSP (R = 2).

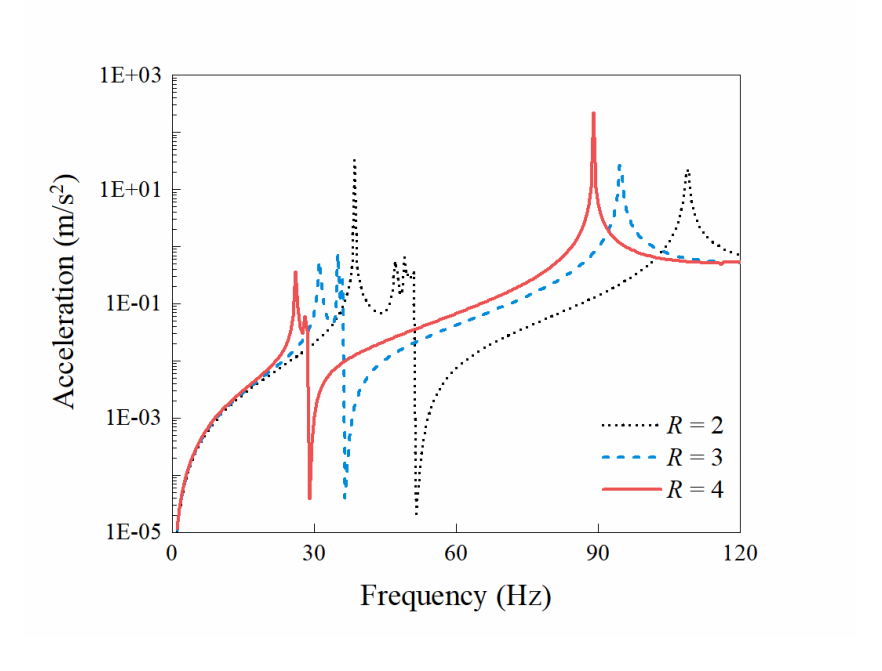


Figure 3.11 The acceleration response of the IA-MSP at different *R*-values.

3.2.3 Results of Experimental Study

A vibration experiment is conducted to investigate the vibration attenuation capabilities of the IA-MSP in this subsection. Figure 3.2 illustrates the experimental specimen of an IA-MSP consisting of 6×5 unit cell. To facilitate the preparation of experimental specimen, all components including the spring, lever, mass, support bar, and faceplate are fabricated using steel material, possessing the following properties: a Young's modulus of 200 GPa, a density of 7850 kg/m³, and a Poisson ratio of 0.3. The geometrical parameters of the experimental specimen are shown in Table 3.3. In this experimental specimen, the supporting bar and lever are hinged together by a bolt that passes through the holes. The supporting bars and face plates, face plates and springs, levers and masses, levers and springs are all connected by laser welding. The experimental setup of the vibration test is presented in Figure 3.3. The boundary conditions in the experiment are identical to those shown in Figure 3.7, where the two short edges of the plate are clamped to the foundation, while the remaining two edges are unconstrained. The excitation perpendicular to the face plate is applied through a KISTLER type 9276A force hammer. The vibration acceleration is sampled by the Brüel & Kjær type 4394 accelerometer and recorded by the Brüel & Kjær Pulse 3160. The measured acceleration vibration signal is represented as a time-domain signal. The Fast Fourier Transform (FFT) analysis module in Pulse is capable of performing a rapid Fourier transformation on time domain data, enabling frequency spectrum analysis to obtain the vibration characteristics of the IA-MSP. The excitation and response acquisition positions are identical to those in Figure 3.7.

Table 3.3 Geometrical parameters of the experimental specimen of an IA-MSP with 6 \times 5 unit cells. (a = 0.1 m)

Structure	Length, width, and height
Mass	$0.050a \times 0.900a \times 0.300a$
Lever	$0.900a \times 0.025a \times 0.300a$
Spring	$0.050a \times 0.025a \times 0.080a$
Support bar	$0.200a \times 0.150a \times 0.530a$

Figure 3.12 presents a comparative analysis between the acceleration response acquired from the experimental study and numerical analysis. The model of the IA-MSP with 6 × 5 unit cells in the numerical analysis is identical to the experimental specimen, encompassing both geometric and material parameters. The bandgap obtained in the band structure ranges from 486 to 682 Hz, as depicted in Figure 3.12 (a). The bandgap (486-682 Hz) is an out-of-plane bandgap. Although there exists a branch within this bandgap, it does not affect the identification of out-of-plane bandgap. This is because the vibration mode associated with this branch corresponds to the in-plane mode. Therefore, as presented in Figure 3.12 (b), there are no resonance peaks within the AZ due to the out-of-plane excitation used in the numerical analysis. However, the location of the AZ observed in the experimental study, presented in Figure 3.12 (c), is not entirely consistent with the location identified in the numerical analysis, as presented in Figure 3.12 (b). The AZ range acquired from the experiment is approximately 400-600 Hz, which is around 80 Hz lower than the numerical analysis results. The acceleration attenuation in the experimental study is not especially evident compared

to the numerical analysis. They are potentially due to the experimental model lacking entirely coordinated connection conditions and an ideal constraint. For example, the hinge conditions created by the bolts in the experimental setup are not ideal, as they exhibited frictional effects and the presence of voids at the hinge joint. Additionally, two short edges of the plate are not perfectly clamped with clamps. The difference may also be attributed to material damping of the experimental model and processing deviations. Moreover, a presence of several resonance peaks within the AZ is evident in Figure 3.12 (c), contrasting the absence of any resonance peak within the AZ in Figure 3.12 (b). This discrepancy may be due to the slightly larger rigidity of the hammer head employed in the experimental setup, leading to an unstable initial excitation signal imparted by the force hammer. It could also potentially be caused by the neglect of several factors in the numerical simulation, including damping, nonlinearities, material defects and backlash in the hinge joints. These factors, when present in the experiment, can significantly influence the system's response and lead to the appearance of small resonance peaks. Despite discrepancies between results of numerical simulation and experiment, it has been demonstrated that the IA-MSP exhibits a significant vibration attenuation effect within the bandgap region.

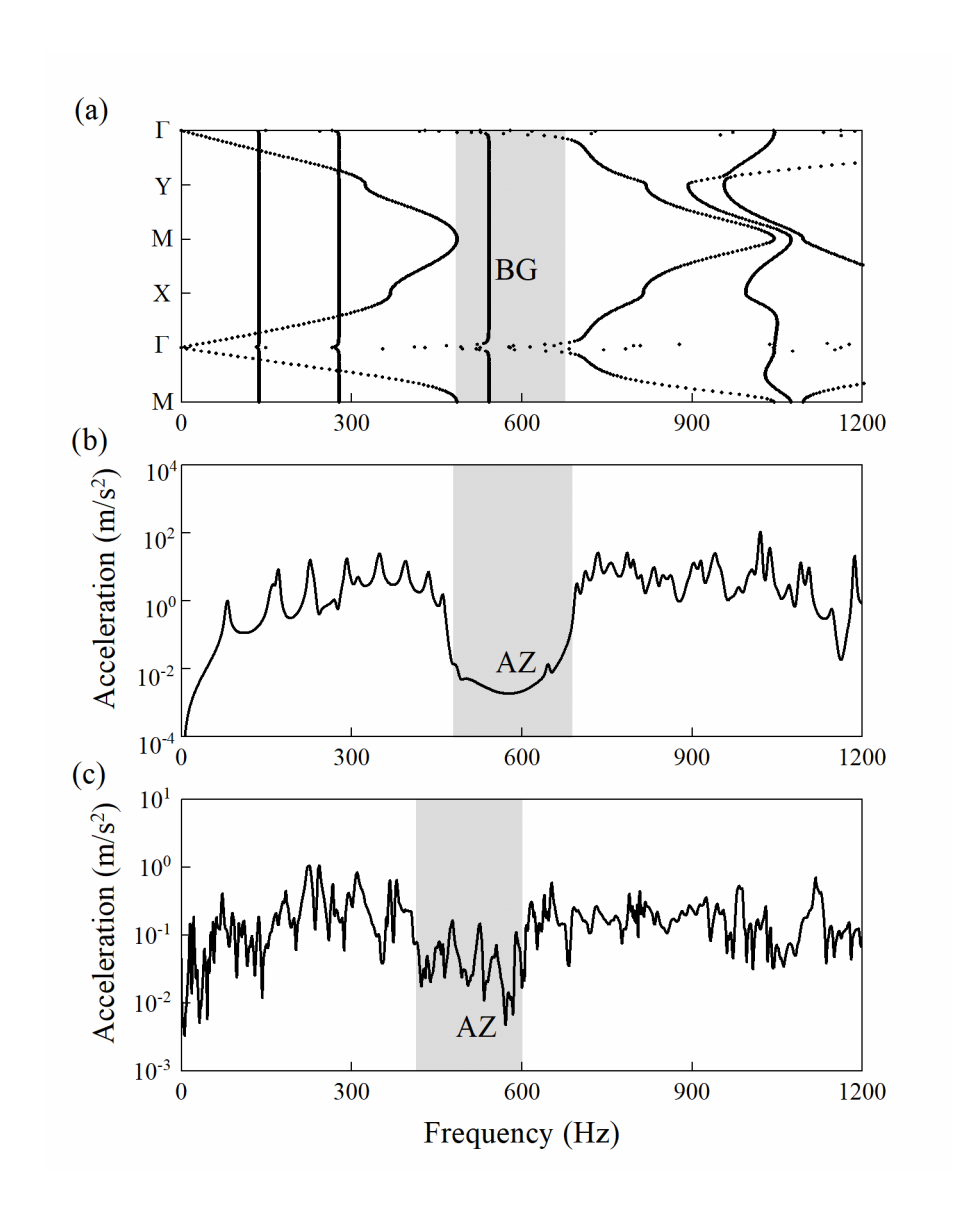


Figure 3.12 The result comparison: (a) the band structure of the IA-MSP, (b) the acceleration response in the numerical analysis, (c) the acceleration response in the experiment.

A normalized comparison is conducted to quantitatively evaluate the vibration attenuation performance and lightweight design of the proposed structure and other kinds of reported metamaterials sandwich plates (H. Li et al., 2021; Z.-Y. Li et al., 2020; Xi et al., 2021; G.-L. Yu & Miao, 2019), as presented in Figure 3.13. To evaluate the

width and position of the bandgap, the relative bandwidth (RW) is introduced (Muhammad & Lim, 2019):

$$RW = \frac{f_u - f_l}{0.5(f_u + f_l)},\tag{3.23}$$

where, f_u and f_l denote the upper and lower boundary frequency of bandgap, respectively. A larger RW indicates a wider bandgap. A normalized lower boundary frequency $f_{nd,l} = f_l a/v_s$ is introduced to assess quantitatively the bandgap characteristics (H. Li et al., 2021; Lim et al., 2020), where a is the lattice constant, and v_s is the shear wave velocity of the host structure. A relative density $\bar{\rho}_c = \rho_c/\rho$ is used to evaluate the degree of lightweight design, which is defined as the ratio of the average density of the core ρ_c to the density of host structure material ρ (H. Li et al., 2021; Z. Xue & Hutchinson, 2004). The average density of the core ρ_c is defined as $\rho_c = \frac{m_c}{V_c}$, where m_c is the total mass of the core layer, and V_c is the space volume occupied by the core layer (the cuboid space between the two faceplates containing all resonators, including void spaces). When the material of the core layer is the same with the material of the host structure, the relative density $\bar{\rho}_c = \frac{\rho_c}{\rho} = \frac{V_s}{V_c}$, where V_s is the equivalent volume of core layer (solid volume of resonators only). Notably, the coordinates of $f_{nd,l}$ and $\bar{\rho}_c$ have been taken the reciprocal to ensure a uniform representation of the performance levels in the radar diagrams presented in Figure 3.13. In the radar diagrams depicted in Figure 3.13, it should be observed that a larger covered area in the radar diagram represents the advantageous combination of a wider low-frequency vibration attenuation performance and a lightweight design. Figure 3.13 (a) illustrates normalized comparisons between the IA-MSP and typical metamaterials sandwich 48

plates. Notably, the IA-MSP exhibits the largest covered area, indicating its superior overall performance. This superiority extends not only to single-phase metamaterial sandwich plates (Figure 3.13 (b)) but also to multi-phase metamaterial sandwich plates (Figure 3.13 (c)). The aforementioned comparisons further confirm the outstanding lightweight design and the low-frequency, broadband vibration attenuation capabilities of the proposed IA-MSP.

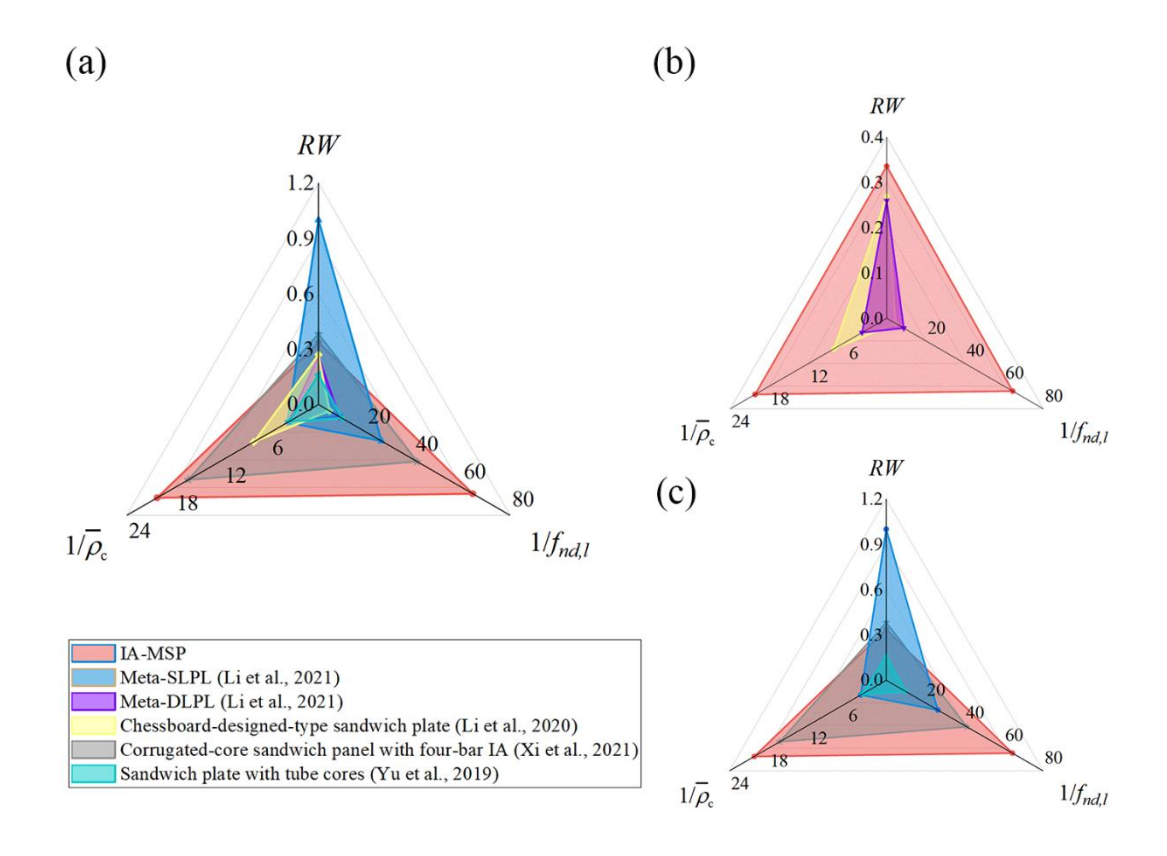


Figure 3.13 Normalized comparisons between the IA-MSP and (a) typical metamaterials sandwich plates. Comparison of (b) the single-phase metamaterial sandwich plates and (c) the multi-phase metamaterial sandwich plates.

3.3. Summary

This chapter proposes a novel metamaterial sandwich plate with lever-type IA resonators (IA-MSP) to achieve broadband vibration attenuation at low frequencies. The dynamic model of the unit cell is mathematically formulated, allowing for the theoretical determination of the bandgap. FEM simulations and experiments have been conducted to verify such excellent vibration attenuation properties. The results demonstrate that, compared with traditional LR-MSPs possessing identical geometric and material properties, the IA-MSP with a lever ratio R=2 exhibits boundary frequencies approximately half those of the LR-MSP. Moreover, an increase in R results in a progressive decrease in the lower boundary frequency, accompanied by a downward shift of the entire bandgap. The superior low-frequency vibration attenuation capability of the IA-MSP is attributed to the amplification effect of the lever-type inertial resonators, which enhance the effective mass of the system and reduce the coupled mode frequency associated with the bandgap. The new findings presented in this study break the long-standing and challenging limitations of conventional traditional LR-type sandwich plates, showing that a lower and broader bandgap can be achieved in IA-MSP while circumventing the necessity of employing high mass. This study provides valuable insights into the development of lightweight sandwich structures with low-frequency broadband vibration attenuation capabilities.

Chapter 4

Broadband Low-frequency Vibration Control of the IA- MSP_{DF2}

This chapter presents a novel metamaterial sandwich plate incorporating two-degreeof-freedom inertial amplification resonators (IA-MSP_{DF2}) designed to achieve two lowfrequency bandgaps and broadband vibration attenuation. Compared with metamaterial sandwich plates embedding multi-frequency local resonators (LR-MMSP) of equivalent additional mass, the IA-MSP_{DF2} demonstrates the ability to achieve multiple bandgaps at significantly lower frequencies. A theoretical dynamic model is developed to elucidate the mechanism responsible for the formation of multiple low-frequency bandgaps in the IA-MSP_{DF2}. The vibration attenuation performance is systematically investigated through both finite element simulations and experimental validation. Furthermore, the influence of various parameters on the vibration transmission characteristics is analyzed. The results reveal that the boundary frequencies of the IA-MSPDF2 correspond precisely to the lever ratios of the LR-MMSP. By adjusting the lever ratios, fine-tuning and optimization of the multiple low-frequency bandgaps can be achieved. Under a fixed attached mass, increasing the lever ratio further shifts the bandgaps towards lower frequencies. Additionally, as the eigenfrequencies of the primary (f_p) and secondary (f_s) lever-type IA resonators decrease, both the first and second attenuation zones (AZ1 and AZ2) move towards lower frequencies. A decrease in f_p not only shifts AZ1 downward but also leads to a broader AZ1 and further

reductions in minimum acceleration levels within the attenuation zones. Moreover, increasing the damping within the inertial amplification resonators promotes the expansion and eventual merging of the two attenuation zones into a single broader band. A normalized comparison validates the superior performance of the IA-MSP_{DF2}, confirming its advantages in achieving lightweight structural design and effective low-frequency broadband vibration attenuation.

4.1. Methodology

A theoretical dynamic model of the IA-MSP_{DF2} is presented to explain the underlying multi-bandgap IA mechanism in this section. Through the establish of dynamic equation for the IA-MSP_{DF2}, the dispersion equation is derived to determine the expression for the bandgaps. Then, a comparative analysis is carried out to validate the effectiveness of IA-MSP_{DF2} in achieving lower frequencies through the inertial amplification mechanism. This analysis involves comparing the bandgap results obtained from the IA-MSP_{DF2} with those obtained from metamaterial plates incorporating multi-frequency spring-mass resonators. The FEM and experimental setup are also presented in this section

4.1.1 Theoretical Model and Finite Element Modelling

The IA-MSP_{DF2} consists of two face plates and a periodic array of multi-frequency lever-type IA resonators, and its unit cell is illustrated in Figure 4.1 (a). m_1 and m_2 are the mass of the primary and secondary lever-type IA resonator, respectively. k_1 and k_2 are the spring stiffness of the primary and secondary lever-type IA resonator,

respectively. l_1 and l_2 are the distance from the spring to support bar and from the support bar to the mass, within the primary lever-type IA resonator, respectively. l₃ and l₄ are the distance from the spring to support bar and from the support bar to mass, within the secondary lever-type IA resonator, respectively. The classical plate theory is referred to section 3.1.1. To explain the IA mechanism of the resonator, a theoretical dynamic model of the IA-MSP_{DF2} is constructed. The motion of the mass within both the primary and secondary lever-type IA resonators is depicted in Figure 4.1 (b) to provide a clearer illustration. This study primarily investigates the vertical vibration of the structure, with particular emphasis on the vibrational behavior along the vertical axis. The horizontal displacement of the resonators is negligible in comparison to the vertical displacement. Consequently, the analysis predominantly concentrates on the longitudinal displacement of the resonators. The displacements of the primary and secondary mass are represented by w_1 and w_2 , respectively. w_0 is the displacement of the support bar. The assumption is made that the lever is rigid and possesses no mass. By establishing dynamic equation for the IA-MSP_{DF2}, the dispersion equation is derived to determine the expression for the bandgaps. For the primary and secondary lever-type IA resonators, the governing equations describing the vibration of the resonators are derived by applying Newton's second law and the lever law:

$$m_2\ddot{w}_2 + \frac{k_2}{R_2^2}(w_2 - w_1) = 0,$$
 (4.1)

$$m_1\ddot{w}_1 - \frac{k_2}{R_2^2}(w_2 - w_1) + \frac{k_1w_1}{R_1^2} = 0,$$
 (4.2)

where $R_1 = l_2 / l_1$ and $R_2 = l_4 / l_3$ denote the lever ratios of the primary and secondary lever-type IA resonators, respectively.

Given that the elastic wave within the IA-MSP_{DF2} consisting of a periodic unit cell, the displacements of face plates w, the support bar w_0 , the primary mass w_1 , and the secondary mass w_2 are hypothesized to manifest in the ensuing expressions:

$$w = Ae^{i(\alpha x + \beta y - \omega t)}, \ w_0 = Ae^{-i\omega t}, \ w_1 = Be^{-i\omega t}, \ w_2 = Ce^{-i\omega t},$$
 (4.3)

where α and β denote the wavenumbers in the x- and y- directions, ω is the wave frequency, and A, B and C denote the displacement amplitudes. The study is focused exclusively on the investigation of low-frequency oscillations. It is hypothesized that the wavelength significantly exceeds the resonator length, thus rendering phase differences between w_0 , w_1 , and w_2 negligible.

By substituting $w_1 = Be^{-i\omega t}$ and $w_2 = Ce^{-i\omega t}$ in Eqs. (4.1) and (4.2), the eigenfrequency of multi-frequency lever-type IA resonator can be determined through the ensuing computations as outlined below:

$$\omega_{1},\omega_{2} = \frac{\sqrt{2}}{2} \sqrt{\frac{k_{1}}{R_{1}^{2}m_{1}} + \frac{k_{2}}{R_{2}^{2}m_{2}} + \frac{k_{2}}{R_{2}^{2}m_{1}} \pm \frac{\sqrt{-4R_{1}^{2}R_{2}^{6}k_{1}k_{2}m_{1}m_{2} + \left(R_{1}^{2}R_{2}^{2}k_{2}m_{1} + R_{2}^{4}k_{1}m_{2} + R_{1}^{2}R_{2}^{2}k_{2}m_{2}\right)^{2}}}{R_{1}^{2}R_{2}^{4}m_{1}m_{2}}.$$
 (4.4)

The primary (secondary) resonator system is characterized by the kinetic energy T_{m1} (T_{m2}) and elastic strain energy $U_{m1}(U_{m2})$, as defined below:

$$T_{m1} = \frac{1}{2} m_1 \dot{w}_1^2, \tag{4.5}$$

$$T_{m2} = \frac{1}{2} m_2 \dot{w}_2^2, \tag{4.6}$$

$$U_{m1} = \frac{1}{2} \frac{k_1}{R_1^2} (w_1 - w_0)^2, \tag{4.7}$$

$$U_{m2} = \frac{1}{2} \frac{k_2}{R_2^2} (w_2 - w_1)^2. \tag{4.8}$$

To formulate the equations governing the behavior of the metamaterial sandwich plate, Hamilton's principle can be employed as a fundamental principle of mechanics:

$$\int_0^t (\delta T - \delta U + \delta T_m - \delta U_m) = 0, \qquad (4.9)$$

where $T_m = T_{m1} + T_{m2}$ and $U_m = U_{m1} + U_{m2}$ are the overall kinetic energy and elastic strain energy of the lever-type IA resonator system.

By substituting Eq. (4.3) in Eq. (4.9), the ensuing result yields the following set of algebraic equations:

$$\begin{bmatrix} \frac{8\sin(\frac{\alpha\alpha\chi}{2})\sin(\frac{\beta\omega_y}{2})}{\alpha\beta} \left[\rho h \omega^2 - \frac{(H^3 - (H - h)^3)}{3} \left(Q_{11} \alpha^4 + 2 Q_{12} \alpha^2 \beta^2 + Q_{22} \beta^4 + 4 Q_{66} \alpha^2 \beta^2 \right) \right] - \frac{k_1}{R_1^2} & \frac{k_1}{R_1^2} & 0 \\ \frac{k_1}{R_1^2} & m_1 \omega^2 - \frac{k_1}{R_1^2} - \frac{k_2}{R_2^2} & \frac{k_2}{R_2^2} \\ 0 & \frac{k_2}{R_2^2} & m_2 \omega^2 - \frac{k_2}{R_2^2} \end{bmatrix} \begin{pmatrix} A \\ B \\ C \end{pmatrix} = 0, \quad (4.10)$$

where H represents the overall height of the structure, and h represents the thickness of the face plates. To ensure non-zero solutions for the eigenvalue problem formulated in Eq. (4.10), the determinant of the associated matrix must equal zero. Thus, the dispersion equation relating ω , α , and β is derived in the following manner:

$$\begin{cases} \frac{8\sin(\frac{\alpha\omega_x}{2})\sin(\frac{\beta\omega_y}{2})}{\alpha\beta} \left[\rho h\omega^2 - \frac{(H^3 - (H - h)^3)}{3} \left(Q_{11}\alpha^4 + 2Q_{12}\alpha^2\beta^2 + Q_{22}\beta^4 + 4Q_{66}\alpha^2\beta^2 \right) \right] - \frac{k_1}{R_1^2} \right\} \left(m_1 m_2 \omega^4 - \frac{k_2}{R_2^2} m_1 \omega^2 - \frac{k_1}{R_1^2} m_2 \omega^2 + \frac{k_1 k_2}{R_1^2 R_2^2} - \frac{k_2}{R_2^2} m_2 \omega^2 \right) \\ - \frac{k_1^2}{R_1^4} m_2 \omega^2 + \frac{k_1^2 k_2}{R_1^4 R_2^2} = 0, \end{cases}$$

$$(4.11)$$

The ω is determined by solving Eq. (4.11) for the values of α and β . The lower boundary of bandgaps corresponds to ω as α and β approach zero, whereas the upper boundary

of the bandgap corresponds to ω when α and β approach infinity. By dividing the wave frequencies at the bandgap boundaries by 2π , the bandgap can be expressed as follows:

Bandgap1:
$$(f_{11}, f_{11}),$$
 (4.12)

Bandgap2:
$$(f_{l2}, f_{u2}),$$
 (4.13)

where

$$f_{l1} = \frac{\sqrt{2}}{4\pi} \sqrt{\frac{k_1}{R_1^2 m_1} + \frac{k_2}{R_2^2 m_2} + \frac{k_2}{R_2^2 m_1} - \sqrt{\frac{k_1^2}{R_1^4 m_1^2} + \frac{k_2^2}{R_2^4 m_2^2} + \frac{k_2^2}{R_2^4 m_1^2} - \frac{2k_1 k_2}{R_1^2 R_2^2 m_1 m_2} + \frac{2k_2^2}{R_2^4 m_1 m_2} + \frac{2k_1 k_2}{R_1^2 R_2^2 m_1^2}},$$
 (4.14)

$$f_{u1} = \frac{\sqrt{2}}{4\pi} \sqrt{\frac{k_1}{R_1^2 m_1} + \frac{k_2}{R_2^2 m_2} + \frac{k_2}{R_2^2 m_1} + \frac{k_1}{R_1^2 M} - \sqrt{\frac{k_1^2}{R_1^2 m_1^2} + \frac{k_2^2}{R_2^4 m_2^2} + \frac{k_2^2}{R_1^2 m_1^2 m_2} + \frac{2k_1 k_2}{R_1^2 R_2^2 m_1 m_2} + \frac{2k_1 k_2}{R_1^2 R_2^2 m_1^2} + \frac{k_1^2}{R_1^2 R_2^2 m_1^2} - \frac{2k_1 k_2}{R_1^2 R_2^2 m_1^2} + \frac{2k_1 k_2}{R_1^2 R_2^2 m_1^2} + \frac{k_1^2}{R_1^2 R_2^2 m_1^2} - \frac{2k_1 k_2}{R_1^2 R_2^2 m_1^2} + \frac{2k_1 k_2}{R_1^2 R_2$$

$$f_{l2} = \frac{\sqrt{2}}{4\pi} \sqrt{\frac{k_1}{R_1^2 m_1} + \frac{k_2}{R_2^2 m_2} + \frac{k_2}{m_1} + \sqrt{\frac{k_1^2}{R_1^4 m_1^2} + \frac{k_2^2}{R_2^4 m_2^2} + \frac{k_2^2}{m_1^2} - \frac{2k_1 k_2}{R_1^2 m_1 R_2^2 m_2} + \frac{2k_2 k_2}{m_1 R_2^2 m_2} + \frac{2k_1 k_2}{R_1^2 m_1^2}},$$
(4.16)

$$f_{u2} = \frac{\sqrt{2}}{4\pi} \sqrt{\frac{k_1}{R_1^2 m_1} + \frac{k_2}{R_2^2 m_2} + \frac{k_2}{R_2^2 m_1} + \frac{k_1}{R_1^2 M} + \sqrt{\frac{k_1^2}{R_1^4 m_1^2} + \frac{k_2^2}{R_2^4 m_2^2} + \frac{k_2^2}{R_2^2 m_1^2} - \frac{2k_1 k_2}{R_1^2 R_2^2 m_1 m_2} + \frac{2k_2^2}{R_1^2 R_2^2 m_1 m_2} + \frac{2k_1 k_2}{R_1^2 R_2^2 m_1^2} + \frac{k_1^2}{R_1^2 R_2^2 m_1^2} - \frac{2k_1 k_2}{R_1^2 R_2^2 m_1 m_2} + \frac{2k_2^2}{R_2^2 m_1 m_2} + \frac{2k_1 k_2}{R_1^2 R_2^2 m_1^2} + \frac{k_1^2}{R_1^2 R_2^2 m_1^2} - \frac{2k_1 k_2}{R_1^2 R_2^2 m_1 m_2} + \frac{2k_1 k_2}{R_1^2 R_2^2 m_1^2} + \frac{2k_1 k_2}{R_1^2 R_2^2 m_1$$

where f_{l1} and f_{u1} represent the lower and upper boundary frequency of the first bandgap for IA-MSP_{DF2}, respectively. Similarly, f_{l2} and f_{u2} represent the lower and upper boundary frequency of the second bandgap, respectively. $M=2a_xa_y\rho h$ is the mass of two face plates in the unit cell. Eqs. (4.14) and (4.16) indicate that the lower boundary frequencies of bandgaps, denoted as $f_{l1}=\omega_1/2\pi$ and $f_{l2}=\omega_2/2\pi$, align with the eigenfrequencies of resonators in Eq. (4.4). As ω_1 and ω_2 decrease, the bandgaps move to lower frequencies.

The detailed process of theoretical derivation is presented Eqs. (4.15) and (4.17) demonstrate that the upper boundary frequencies of bandgaps are governed by the 56

resonators' eigenfrequency and the face plate mass. Therefore, the adjustment of bandgaps could be made by manipulating the resonators' eigenfrequency and the mass ratio of the resonator to the face plate.

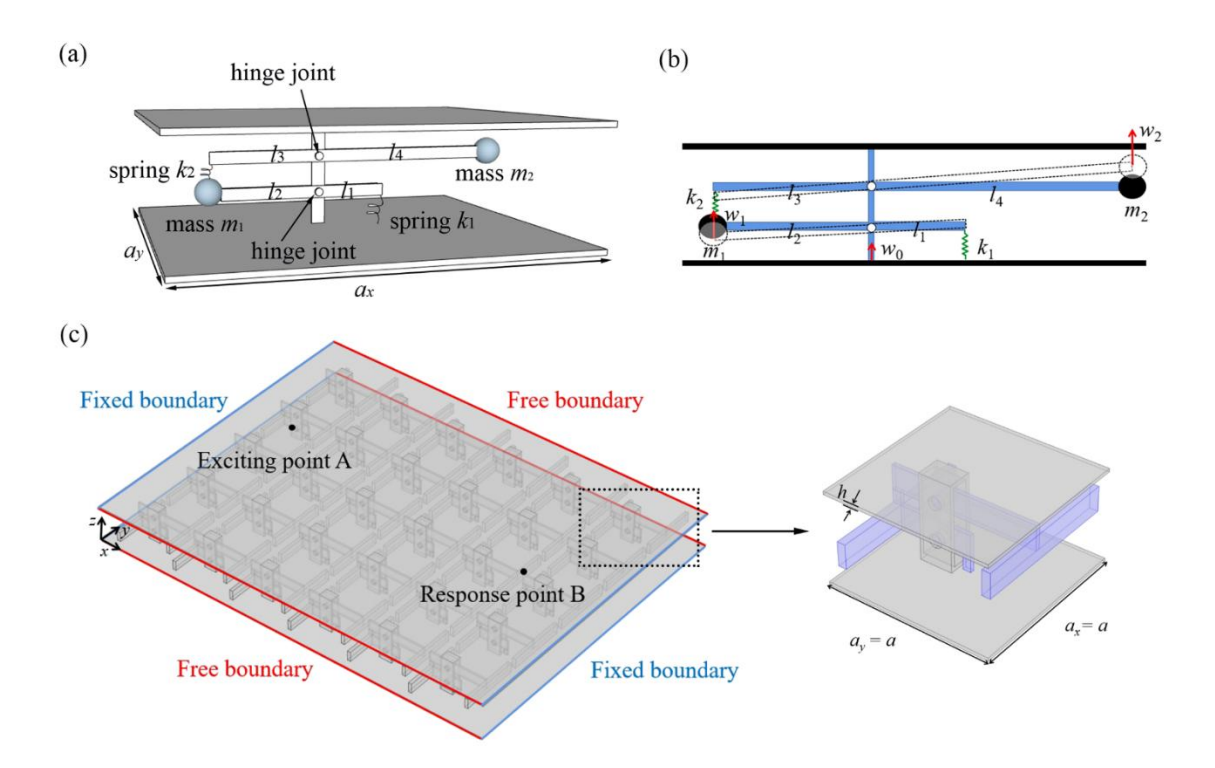


Figure 4.1 Schematic diagram of IA-MSP_{DF2}: (a) a unit cell; (b) displacements of the lever-type IA resonators in a unit cell; (c) the model of IA-MSP_{DF2} with 6×5 unit cells and boundary conditions.

A comparative analysis is conducted to substantiate the efficacy of IA-MSP_{DF2} in achieving lower frequencies through the lever-type IA mechanism. The bandgap results of IA-MSP_{DF2} is compared to those of metamaterial plates that integrate two degrees of freedom (2-DOF) spring-mass resonators (Xiao et al., 2019). The unit cell of the metamaterial plate with 2-DOF spring-mass resonators is shown in Figure 4.2. This comparison is carried out while ensuring that the parameters remain identical across the systems. The mass and spring parameters of resonators are same with Ref. (Xiao et 57

al., 2019): $m_1 = 60$ g, $m_2 = 0.05m_1 = 3$ g, $k_1 = 359670$ N/m, $k_2 = 18930$ N/m, and M = 100230 g. The lever ratios R_1 and R_2 are both assigned a value of 2. Figure 4.3 (a) presents the dispersion surface of the IA-MSP_{DF2}, while Figure 4.3 (b) offers a front view of Figure 4.3 (a). Additionally, Figure 4.3 (c) provides a partial magnification of the dispersion surface. The dispersion curves exhibit two bandgaps (represented by grey regions). The frequency range of the first bandgap is 172–189 Hz, and that of the second bandgap is 221-233 Hz. In contrast, the bandgaps in metamaterial plates incorporating 2-DOF spring-mass resonators span from 352 Hz to 378 Hz and from 442 Hz to 465.5 Hz under the same spring and mass conditions (Xiao et al., 2019). The boundary frequencies of the IA-MSP_{DF2} are exactly half of those of the metamaterial plates incorporating 2-DOF spring-mass resonators due to the lever-type IA mechanism. The eigenfrequency of the primary lever-type IA resonator is determined by $f_p = \frac{1}{2\pi} \sqrt{\frac{k_1}{R_1^2 m_1}}$, and the eigenfrequency of the secondary lever-type IA resonator is given by $f_s = \frac{1}{2\pi} \sqrt{\frac{k_2}{R_2^2 m_2}}$. However, the eigenfrequency of the spring-mass resonator is $f = \frac{1}{2\pi} \sqrt{\frac{k}{m}}$. This implies that the primary and secondary inertial masses are amplified by a factor of R_1^2 and R_2^2 respectively. Therefore, the eigenfrequencies of the primary and secondary resonators are reduced by R_1 and R_2 , respectively. When the lever ratios R_1 and R_2 are both set to 2, the boundary frequencies of the IA-MSP_{DF2} are exactly halved compared to those of the metamaterial plates that incorporate 2-DOF springmass resonators. Figure 4.4 presents the dispersion surfaces of the IA-MSP_{DF2} at different lever ratios. When $R_1 = R_2 = 1$, the lever-type IA resonator is equivalent to the spring-mass resonator. As depicted in Figure 4.4 (a), the bandgaps span from 352 Hz

to 378 Hz and from 442 to 465 Hz. These findings align with the results obtained from the metamaterial plates incorporating 2-DOF spring-mass resonators (Xiao et al., 2019). As the lever ratio increases, the bandgaps of the IA-MSP_{DF2} progressively shift towards lower frequencies as illustrated in Figures 4.4 (b)-(d). Notably, the boundary frequencies of the IA-MSP_{DF2} are precisely 1/*R* of those observed in the metamaterial plates incorporating 2-DOF spring-mass resonators. Therefore, the IA-MSP_{DF2} demonstrate clear advantages in achieving lower frequency bandgaps.

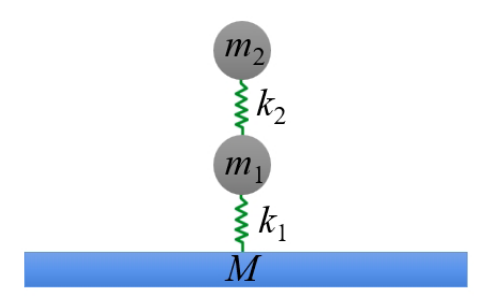


Figure 4.2 Unit cell of the metamaterial plate with 2-DOF spring-mass resonators. (Xiao et al., 2019)

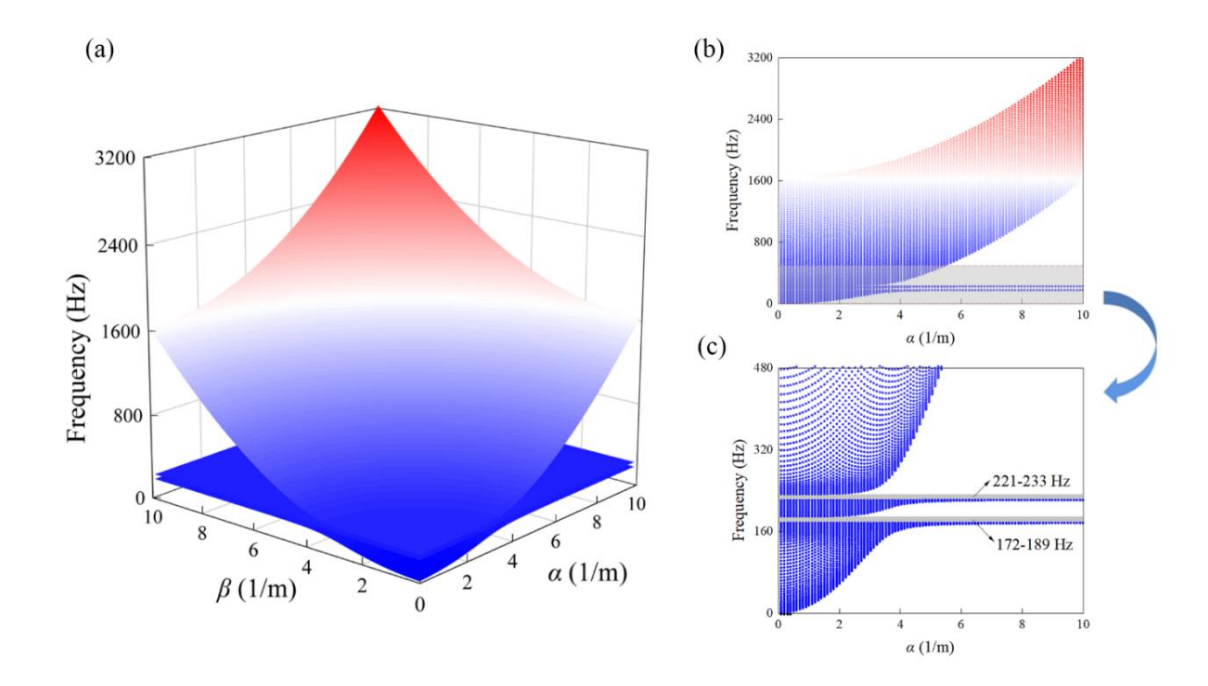


Figure 4.3 Dispersion surfaces of the IA-MSP_{DF2}: (a) dispersion surfaces, (b) a front view of dispersion surfaces and (c) a partial magnification of dispersion surfaces.

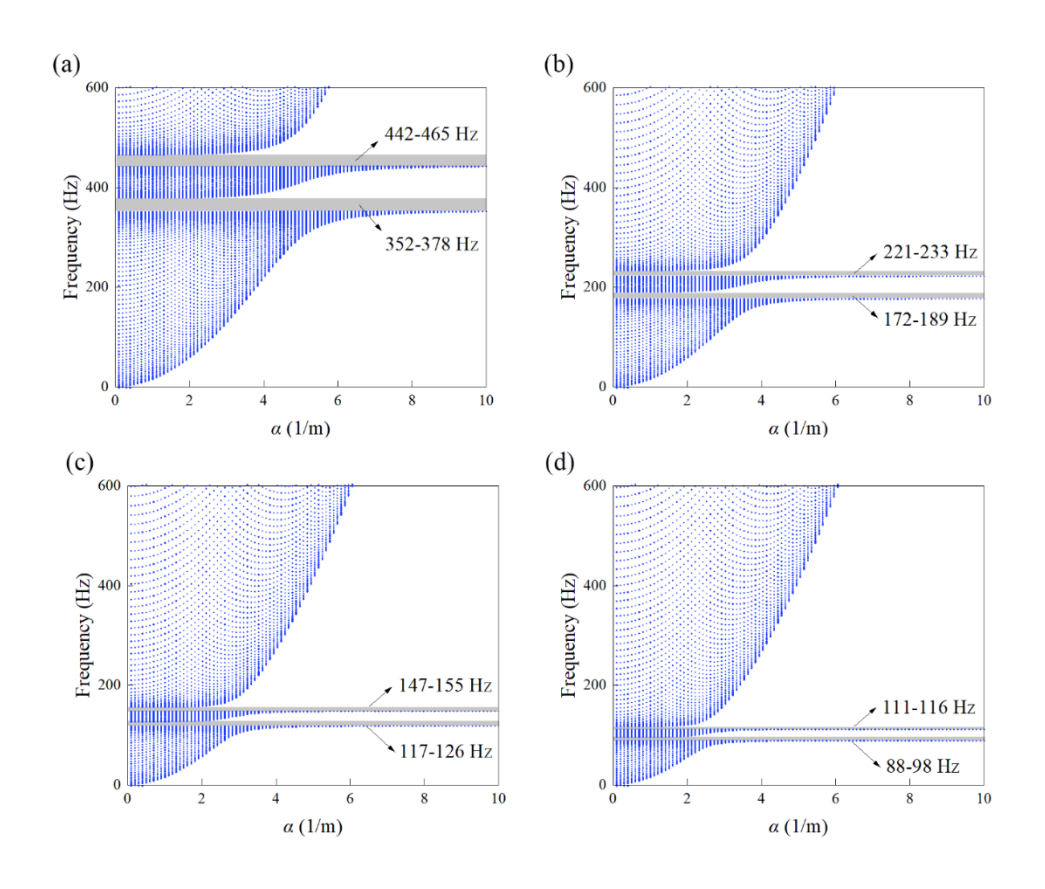


Figure 4.4 Dispersion surfaces of the IA-MSP_{DF2} at different lever ratios: (a) $R_1 = R_2 = 1$, (b) $R_1 = R_2 = 2$, (c) $R_1 = R_2 = 3$, and (d) $R_1 = R_2 = 4$.

The finite element model of the IA-MSP_{DF2} is presented in Figure 4.1 (c). The geometric and material characteristics of IA-MSP_{DF2} are detailed in Tables 4.1 and 4.2. Specifically, the values of the parameters are as follows: $m_1 = 1060$ g, $m_2 = 0.05m_1 = 53$ g, $k_1 = 312500$ N/m, $k_2 = k_1/19 = 16447$ N/m, M = 108 g and $R_1 = R_2 = 2$. Face plates and resonators are meshed using refined swept elements, while the supporting bars are meshed using refined tetrahedral elements. Two short edges of the model are fixed boundaries, and two long edges are free boundaries. External excitation with an amplitude of 1 N along the z-direction is applied at Point A (100 mm, 250 mm, 57 mm), and the response point is at Point B (500 mm, 250 mm, 57 mm), with a frequency spacing of 1 Hz.

Table 4.1 Geometrical parameters of the IA-MSP_{DF2}. (a = 0.1 m, h = 0.002 m)

Structure	Length, width, and height
Mass m_1	$0.050a \times 0.900a \times 0.150a$
Lever 1	$0.450a \times 0.025a \times 0.150a$
Spring k_1	$0.050a \times 0.025a \times 0.080a$
Support bar	$0.200a \times 0.200a \times 0.530a$
Mass m_2	$0.050a \times 0.900a \times 0.150a$
Lever 2	0.900 <i>a</i> ×0.025 <i>a</i> ×0.150 <i>a</i>
Spring k_2	$0.050a \times 0.025a \times 0.080a$
Faceplate	$6.000a \times 5.000a \times h$

Table 4.2 Material parameters of the IA-MSP $_{DF2}$.

Structure	Young's	Poisson	Density
	modulus	ration	(kg/m^3)
	(GPa)		
Mass m_1	200	0.30	7850×20
Mass m_2	200	0.30	7850
Face plates, lever1 and lever 2, and	70	0.33	2700
support bar			
Spring k_1	0.2	0.47	1300
Spring k_2	0.2/19	0.47	1300

4.1.2 Experimental Specimen and Setup

A The experimental specimen of the IA-MSP_{DF2} with 6×5 unit cells and experimental setup are shown in Figure 4.5. To facilitate the preparation of experimental specimen, all components including the springs, levers, masses, support bars, and faceplates were fabricated using steel material. The steel material possesses the following properties: a Young's modulus of 200 GPa, a density of 7850 kg/m3, and a Poisson ratio of 0.3. The geometrical parameters are shown in Table 4.1. The spring component of the primary lever-type IA resonator was welded to the base plate, while the spring part of the secondary lever-type IA resonator was welded to the mass of the primary lever-type IA resonator. The supporting bars and face plates, levers and masses, levers and springs were all connected by laser welding. Both resonators were then connected to the support bar using bolts. Two short edges of the plate were fixed on the foundation using clamps, while the remaining two edges were unconstrained. A KISTLER type 9276A force hammer was used to strike the excitation point on the face plate vertically, a Brüel & Kjær type 4394 accelerometer was utilized to collect the acceleration at the response point, and Brüel & Kjær Pulse 3160B and Labshop were utilized for the data record and analysis. The Pulse software's Fast Fourier Transform (FFT) analysis module can quickly transform time domain data into frequency spectra, allowing for the analysis of vibration characteristics of the IA-MSP_{DF2}.

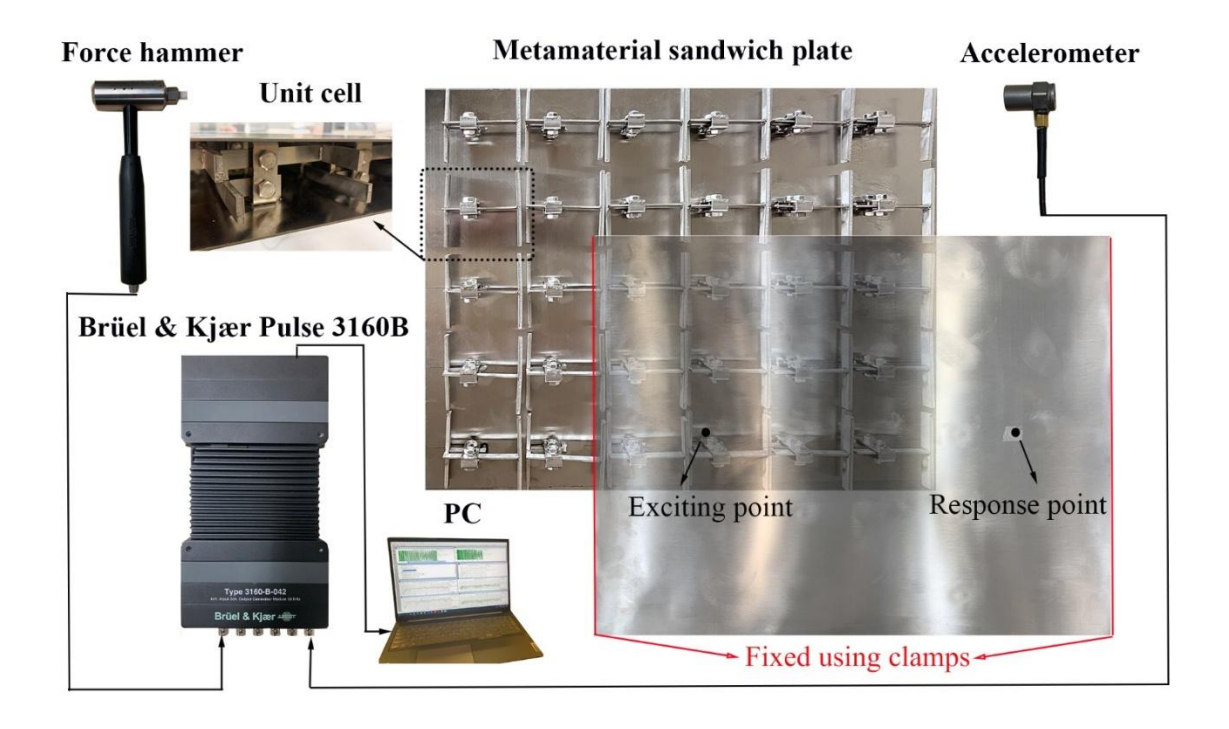


Figure 4.5 Experimental specimen of the IA-MSP_{DF2} and experimental setup.

4.2. Results and Discussions

This section primarily comprises three components. Firstly, the finite element method is employed to study the vibration characteristics of IA-MSP_{DF2}. The numerical results of vibration attenuation zones are compared with the theoretically predicted bandgaps to validate the efficacy of the theoretical model. Vibration modes of IA-MSP_{DF2} are presented for varying excitation frequencies to explain the mechanism of vibration attenuation. A comparative analysis is performed to verify the hypothesis regarding the enhanced low-frequency vibration attenuation capabilities of the IA-MSP_{DF2}. Subsequently, the influence of different parameters on the vibration transmission characteristics of IA-MSP_{DF2} is investigated. Finally, an experimental study is conducted, and a normalized comparison is carried out to quantitatively evaluate the

bandwidth of bandgaps and lightweight design of the proposed IA-MSP_{DF2} and other kinds of reported metamaterial sandwich plates.

4.2.1 Vibration Transmission Research of the IA-MSP_{DF2}

In practical engineering, the size of metamaterial sandwich plate is limited. Therefore, this subsection investigates the vibration transmission of the IA-MSP_{DF2} with 6×5 unit cells through the FEM. The FEM model of IA-MSP_{DF2} is presented in Figure 4.1 (c). The geometric and material characteristics of IA-MSP_{DF2} are detailed in Tables 4.1 and 4.2. The dispersion surfaces of the IA-MSP_{DF2} predicted theoretically are shown in Figure 4.6 (a), and the acceleration response of IA-MSP_{DF2} is illustrated in Figure 4.6 (b). It is evident that significant amplitude attenuation occurs in two frequency range in Figure 4.6 (b), which are termed as attenuation zone (AZ). The frequency ranges of AZ1 (38-42 Hz) and AZ2 (53-150 Hz), are slightly different from those of bandgap1 (39-45 Hz) and bandgap2 (49-142 Hz) shown in Figure 4.6 (a). The deviation may result from the theoretical dispersion analysis not accounting for boundary conditions and applied loads. In addition, in the theoretical derivation, the support bar is assumed to be rigid and possess no mass, while in the FEM analysis the support bar is not rigid and possesses mass. The presence of support bar with mass and non-rigid characteristics in the FEM analysis can lead to differences between the AZ results and the bandgap results. However, the comparison results presented in Figure 4.7 indicates that the theoretical predictions can capture the frequency ranges where significant vibration attenuation occurs. Figure 4.7 shows vibration modes of the IA-MSP_{DF2} at the marked points in Figure 4.6 (b). Notably, the propagation of vibration waves is observed to occur unhindered throughout the entire plate when frequencies lie within

the passband range (36 and 174 Hz). However, remarkable vibration attenuation characteristics are observed within the bandgap1 (40 Hz) and bandgap2 (60 Hz). These results indicate a significant effectiveness of the IA-MSP_{DF2} in suppressing vibrations within bandgaps.

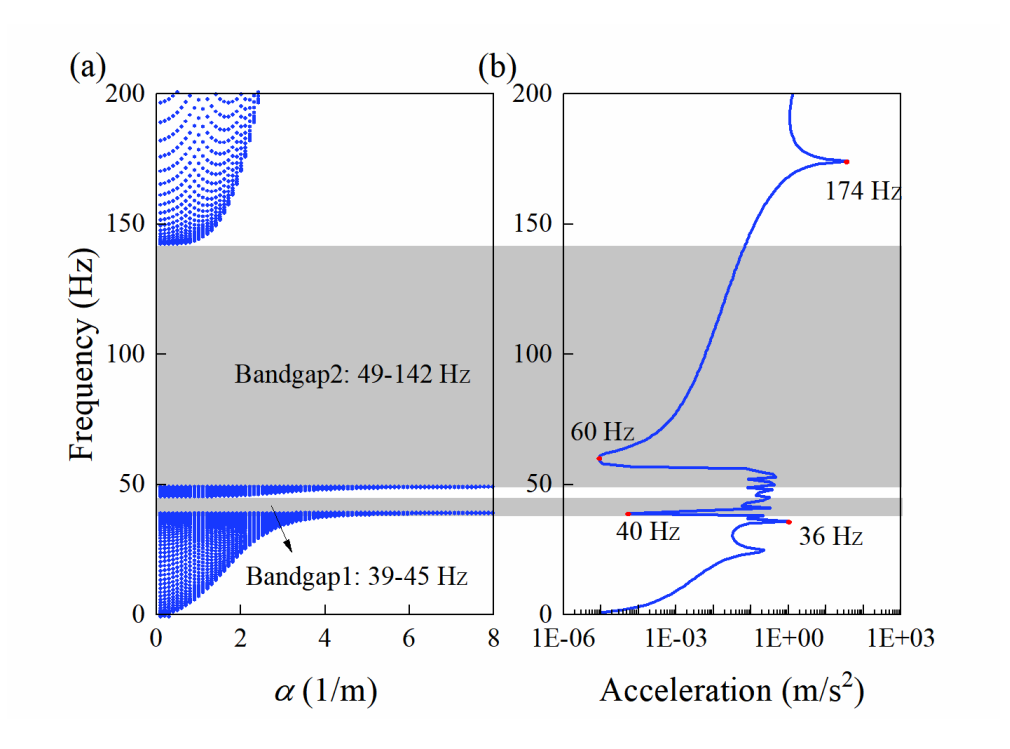


Figure 4.6 Comparison of the theoretical results and the FEM results: (a) the dispersion surfaces of IA-MSP $_{DF2}$ predicted theoretically, (b) the acceleration response through the FEM analysis.

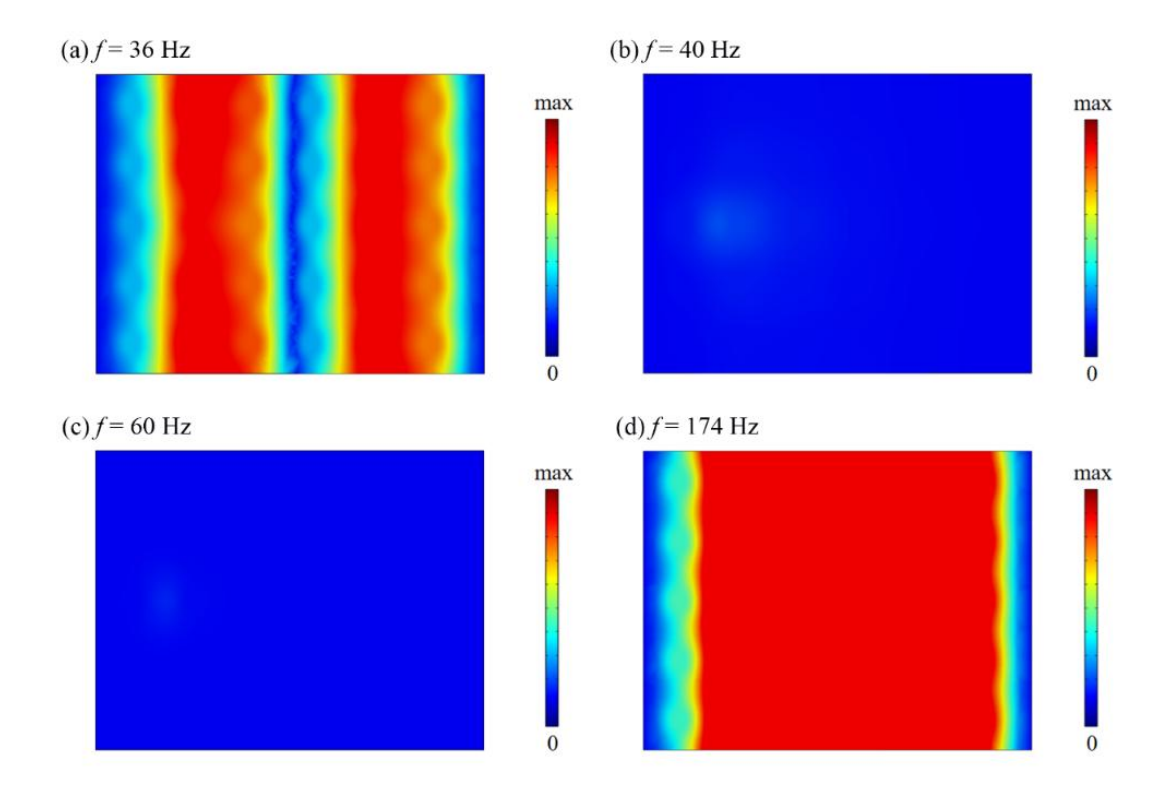


Figure 4.7 The top view of vibration modes of the IA-MSP_{DF2} with 6×5 unit cells at the marked frequencies in Figure 4.6 (b): (a) f = 36 Hz (falling within the passband); (b) f = 40 Hz (falling within the bandgap1); (c) f = 60 Hz (falling within the bandgap2); (c) f = 174 Hz (falling within the passband).

For Moreover, a comparative study is conducted to substantiate the hypothesis of IA-MSP_{DF2} possessing superior low-frequency vibration attenuation capabilities. A metamaterial sandwich plate incorporating multi-frequency local resonators (LR-MMSP) with 6 × 5 resonators is used for the comparison. The unit cell model of LR-MMSP is illustrated Figure 4.8. Figure 4.9 depicts the acceleration response at point B for both IA-MSP_{DF2} and LR-MMSP. It can be observed that the AZs of the LR-MMSP span approximately from 80 Hz to 100 Hz and from 105 Hz to 280 Hz. However, owing to the lever-type IA mechanism, the AZ of the IA-MSP_{DF2} is significantly lower compared to that of the LR-MMSP. Especially, the frequency ranges of AZ1 (39-45 67

Hz) and AZ2 (49-142 Hz) of the IA-MSP_{DF2} are nearly half as low as those of the LR-MMSP. Figure 4.10 presents the dispersion surfaces and acceleration response of the IA-MSP_{DF2} at different lever ratio values. The different lever ratio values are achieved by adjusting the position of the resonator while keeping the total lever length and the support bar position constant. The ranges of AZs observed in the acceleration responses as demonstrated in the right portion are close to the bandgap ranges identified in the dispersion surfaces presented on the left portion. It provides validation for the accuracy of the bandgap estimations derived from theoretical frameworks. In addition, a clear correlation can be observed between the lever ratio and the position of the AZs. Specifically, an increase in the lever ratio results in a significant downward shift of the AZs in frequency. This observation signifies that Under mass constraints, tuning the lever ratio allows for the attainment of lower bandgaps.

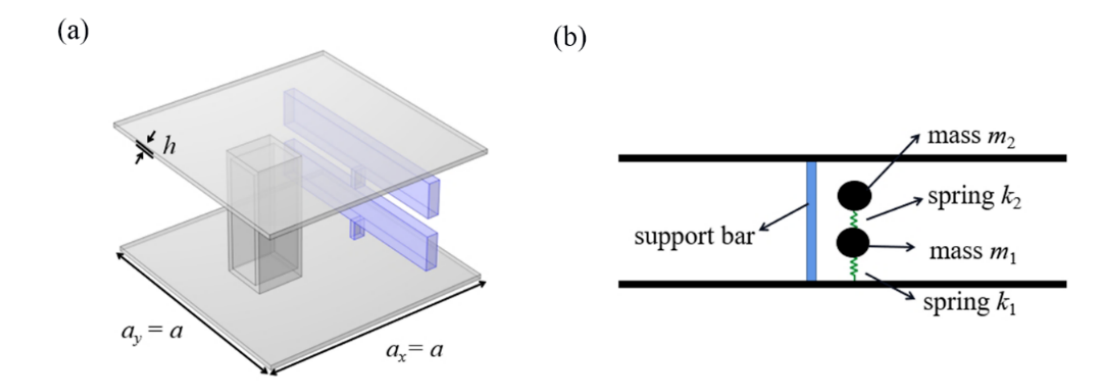


Figure 4.8 Schematic diagram of (a) the unit cell of the metamaterial sandwich plate incorporating multi-frequency local resonators (LR-MMSP); (b) simplified model of the unit cell.

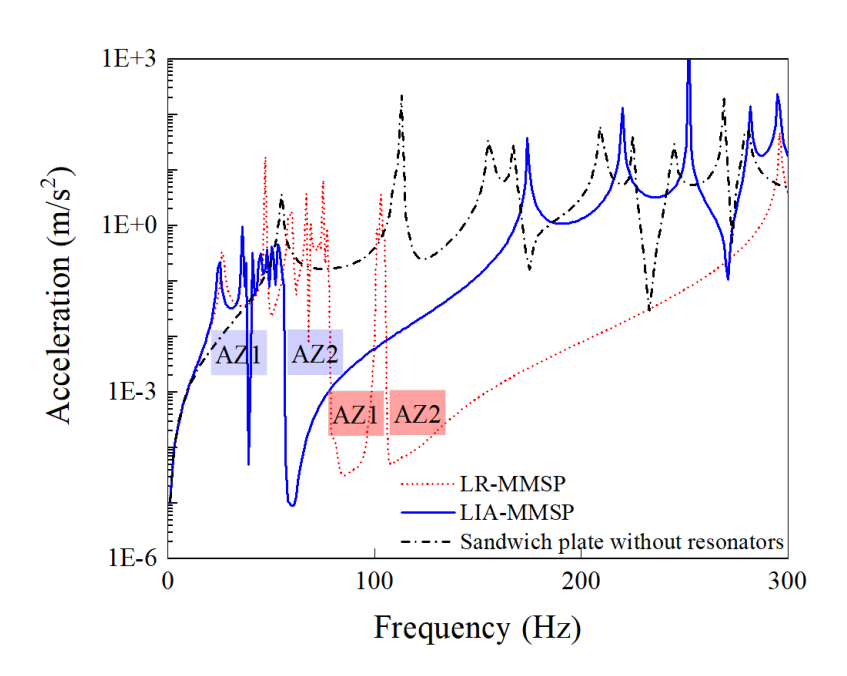


Figure 4.9 Acceleration response of the IA-MSP $_{DF2}$, the LR-MMSP and sandwich plate without resonators.

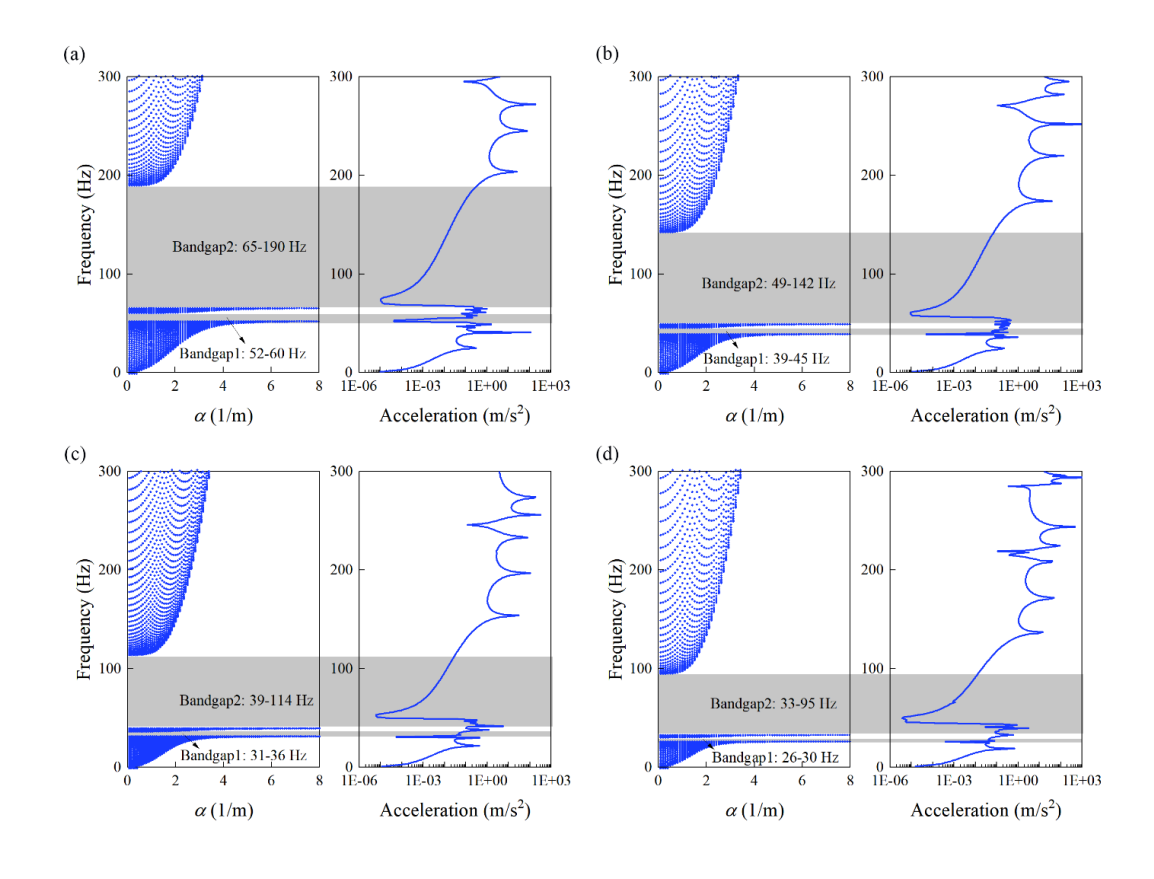


Figure 4.10 Dispersion surfaces and acceleration responses of the IA-MSP_{DF2}: (a) $R_1 = R_2 = 1.5$, (b) $R_1 = R_2 = 2$, (c) $R_1 = R_2 = 2.5$, and (d) $R_1 = R_2 = 3$.

4.2.2 Effects of Parameters on Vibration Transmission

This subsection focuses on investigating how different parameters affect the vibration transmission behavior of the IA-MSP_{DF2}. Owing to the lever-type IA mechanism, the eigenfrequency of the primary resonator is $f_p = \frac{1}{2\pi} \sqrt{\frac{k_1}{R_1^2 m_1}}$, and the eigenfrequency of the secondary resonator is $f_s = \frac{1}{2\pi} \sqrt{\frac{k_2}{R_2^2 m_2}}$. The geometric and material characteristics of the plate are detailed in Tables 4.1 and 4.2, and these parameters remain consistent with the descriptions provided in subsections 4.2.1. Specifically, the values of the parameters are as follows: $m_1 = 1060$ g, $m_2 = 0.05m_1 = 53$ g, $k_1 = 312500$ N/m, $k_2 = 1000$ g, $m_2 = 1000$ g, $m_3 = 1000$ g, $m_4 = 1000$ g, $m_5 = 1000$ g, $m_6 = 1000$ g, m_6

 $k_1/19 = 16447$ N/m, M = 108 g and $R_1 = R_2 = 2$. ($f_p = 43$ Hz, $f_s = 44$ Hz, $\chi = 0.05$, and $\psi = 9.8$). $\chi = m_2/m_1$ denotes the mass ratio between the secondary lever-type IA resonator and the primary lever-type IA resonator, and $\psi = m_1/M$ denotes the mass ratio between the primary lever-type IA resonator and the face plates.

Figure 4.11 (a) shows the acceleration responses at Point B of the IA-MSP_{DF2} at different eigenfrequencies of the primary lever-type IA resonator f_p . Modifying the spring k_1 will result in a corresponding adjustment in the f_p . As f_p decreases, both AZ1 and AZ2 move to lower frequencies, and the width of AZ1 expands. Furthermore, as f_p decreases, the smallest acceleration within the AZs diminishes. This relationship suggests that a lower f_p leads to lower frequency AZs and a diminished magnitude of the minimum acceleration. Figure 4.11 (b) shows the effect of different eigenfrequencies of the secondary lever-type IA resonator f_s on the acceleration response of the IA-MSP_{DF2}. Modifying the spring k_2 will result in a corresponding adjustment in the f_s . As f_s decreases, both AZ1 and AZ2 shift towards lower frequencies. However, additional changes in the AZ characteristics are observed. A reduction in f_s leads to a narrower AZ1 and a decrease in the minimum acceleration amplitude within both AZ1 and AZ2. Figure 4.11 (c) shows the acceleration responses at Point B of the IA-MSP_{DF2} at different resonator mass ratios $\chi = m_2/m_1$. Modifying the mass m_1 will result in a corresponding adjustment in the resonator mass ratios χ . As χ decreases, both AZ1 and AZ2 exhibit a downward shift towards lower frequencies, and the frequency range of AZ1 widens. Additionally, the amplitude of the minimum acceleration within both AZ1 and AZ2 decreases. Figure 4.11 (d) shows the effect of different mass ratios of the primary lever-type IA resonator to the face plates $\psi = m_1/M$ on the acceleration responses of the IA-MSP $_{DF2}$. Modifying the faceplate mass M will 71

result in a corresponding adjustment in the resonator mass ratios ψ . From the observation, the frequency range of AZ1 remains unaffected by the parameter ψ . However, as ψ increases, the frequency range of AZ2 expands. This indicates that higher values of ψ lead to a wider range of frequencies where significant vibration attenuation occurs. Sugino et al. (Sugino et al., 2016; Sugino et al., 2017) determined the boundary frequencies of bandgaps in finite locally resonant metamaterials employing a generalized form. They found that increasing the mass ratio of the resonator to main structure resulted in an expansion of the bandgap range. This phenomenon is also evident in Figure 4.11 (d). However, in the practical engineering applications, increasing the mass ratio within elements such as floors or columns may introduce various challenges related to constructability and costs (Choi et al., 2022).

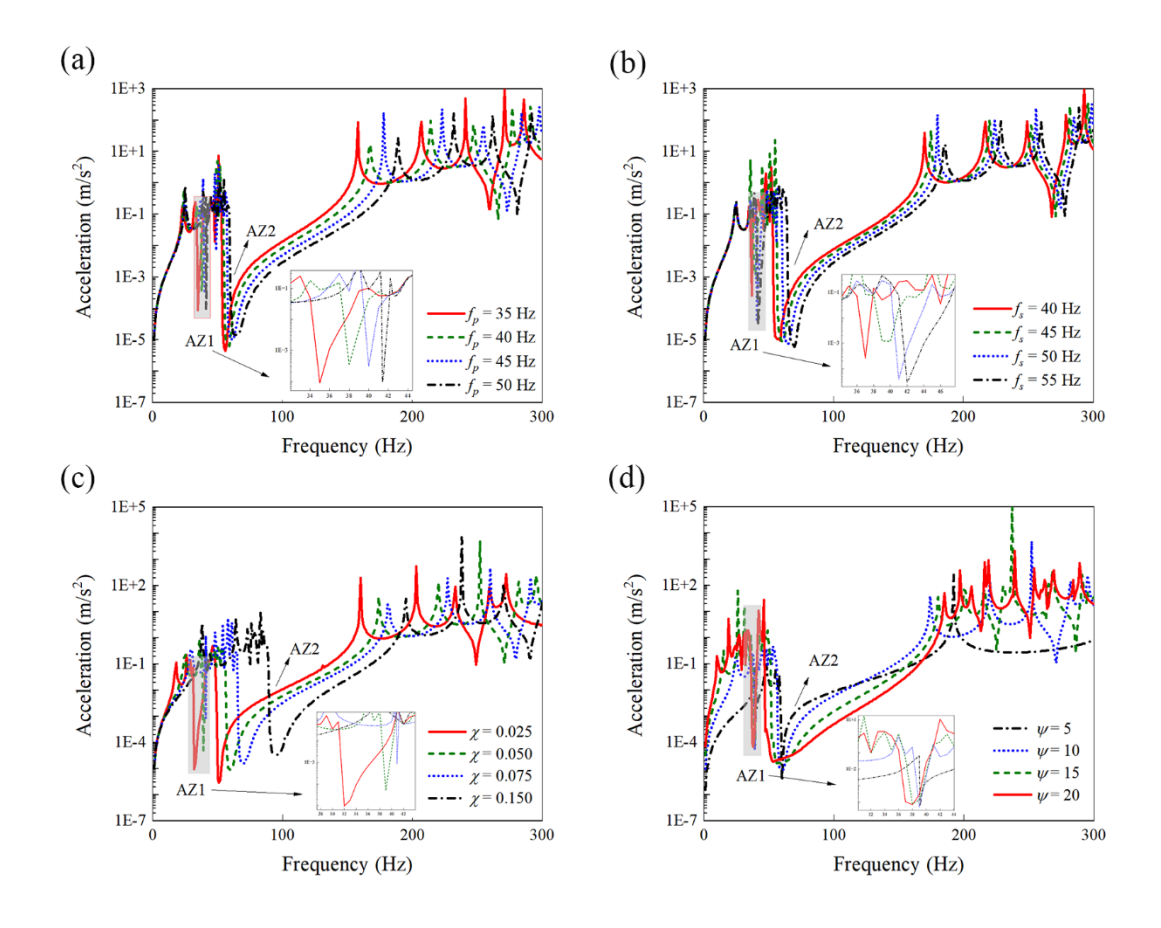


Figure 4.11 Acceleration responses of the IA-MSP_{DF2} for different parameters: (a) eigenfrequencies of the primary lever-type IA resonator f_p , (b) eigenfrequencies of the secondary lever-type IA resonator f_s , (c) resonator mass ratios $\chi = m_2/m_1$, (d) mass ratios of the primary lever-type IA resonator to the face plates $\psi = m_1/M$.

4.2.3 Experimental Validation

The vibration attenuation characteristic of the IA-MSP_{DF2} has been studied theoretically and numerically. Further experimental study is required to facilitate the practical implementation. An experimental specimen of the IA-MSP_{DF2} with 6×5 unit cells was fabricated and evaluated to confirm its attenuation performance. The experimental specimen of the IA-MSP_{DF2} and experimental setup are illustrated in

Figure 4.5 To facilitate the preparation of experimental specimen, all components including the springs, levers, masses, support bars, and faceplates were fabricated using steel material. The steel material possesses the following properties: a Young's modulus of 200 GPa, a density of 7850 kg/m3, and a Poisson ratio of 0.3. The geometrical parameters are shown in Table 4.1. Figure 4.12 presents the acceleration response obtained from the numerical simulation and experimental study. In the numerical result shown in Figure 4.12 (b), the AZ1 ranges from 500 to 620 Hz, while the AZ2 spans from 740 to 950 Hz. In the experimental result presented in Figure 4.12 (b), the AZ1 approximately ranges from 390 to 610 Hz, and AZ2 spans from 670 to 950 Hz. The obtained lower boundaries of AZ1 and AZ2 are approximately 110 Hz and 70 Hz lower than those obtained from the numerical analysis. Furthermore, the width of AZ1 and AZ2 obtained in the experimental study demonstrates an extension of approximately 100 Hz and 70 Hz beyond the range obtained through numerical simulation. The observed difference may be attributed to the absence of fully coordinated connection conditions and an ideal constraint within the experimental model. For instance, the hinge conditions established by the bolts in the experimental setup are not ideal due to the occurrence of frictional effects and the existence of voids at the hinge joint. Moreover, the clamping of the two short edges of the plate with clamps did not achieve a perfect configuration. The observed discrepancy may also be influenced by material damping of the experimental model and deviations in the manufacturing process. The bandwidth of the bandgaps is influenced by the damping characteristics of the resonators (Choi et al., 2024; Jinqiang Li et al., 2020; Jingru Li et al., 2020; Peng & Pai, 2014; Peng et al., 2015; D. Yu et al., 2006). In addition, achieving precise control over the force magnitude applied by humans in hammer experiments poses a challenge,

which results in inconsistencies in excitation magnitude between the experiment and simulation. Therefore, different acceleration amplitudes of the numerical and experimental results are observed in Figures 4.12 (a) and (b). Although there exists a discrepancy between the results obtained from numerical simulations and experimental observations, it is evident that the IA-MSP_{DF2} displays remarkable vibration attenuation performance across multiple bandgaps.

Furthermore, a normalized comparison is conducted to quantitatively evaluate the bandwidth of bandgaps and the efficacy of the lightweight design of the proposed IA-MSP_{DF2}. Figure 4.13 presents a visual representation of the comparative analysis pertaining to the normalized attenuation bandwidth γ and the relative density $\bar{\rho}_c$ across a range of metamaterial sandwich plates. To assess the width of the bandgaps, a normalized attenuation bandwidth RW is defined as $RW = (f_u - f_l)/[(f_u + f_l)/2]$ (H. Li et al., 2021; Z.-Y. Li et al., 2020; Lim, 2019), where f_u and f_l denote the upper and lower boundary frequency of the bandgap, respectively. The relative density $\bar{\rho}_c = \frac{\rho_c}{\rho}$ is employed to assess the level of lightweight design (Z. Xue & Hutchinson, 2004), which is characterized as the ratio of the average density of the core $\,\rho_{c}\,$ to the density of the host structure material ρ . The average density of the core ρ_c is defined as $\rho_c = \frac{m_c}{V_c}$, where m_c is the total mass of the core layer, and V_c is the space volume occupied by the core layer (the cuboid space between the two faceplates containing all resonators, including void spaces). When the material of the core layer is the same with the material of the host structure, the relative density $\bar{\rho}_c = \frac{\rho_c}{\rho} = \frac{V_s}{V_c}$, where V_s is the equivalent volume of core layer (solid volume of resonators only). It is crucial to highlight that in Figure 4.13, the coordinate of $\bar{\rho}_c$ has been taken the reciprocal. Larger values along

the x-axis correspond to lighter core layers of metamaterial sandwich panels, indicating superior lightweight design. Larger values along the y-axis indicate wider normalized attenuation bandwidth. As illustrated in Figure 4.13, the proposed IA-MSP_{DF2} design demonstrates a wider normalized attenuation bandwidth RW and superior lightweight design in comparison to other types of metamaterial sandwich plate configurations. Experimental investigations and normalized comparisons provide additional evidence supporting the practical applicability and superiority of the proposed IA-MSP_{DF2}.

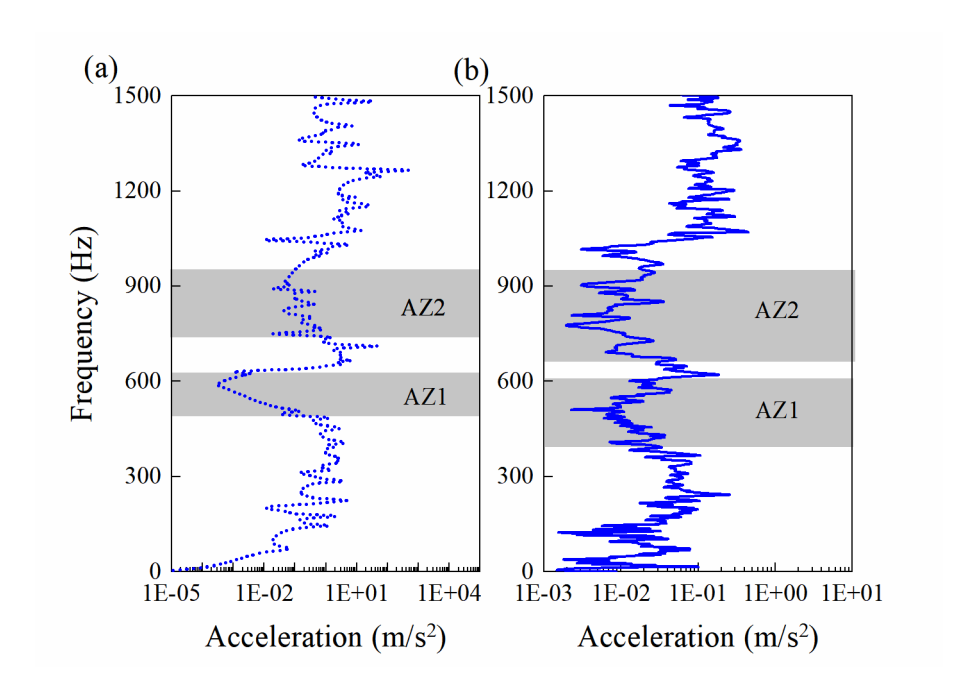


Figure 4.12 Comparison of the acceleration responses: (a) in the numerical simulation; (b) in the experimental study.

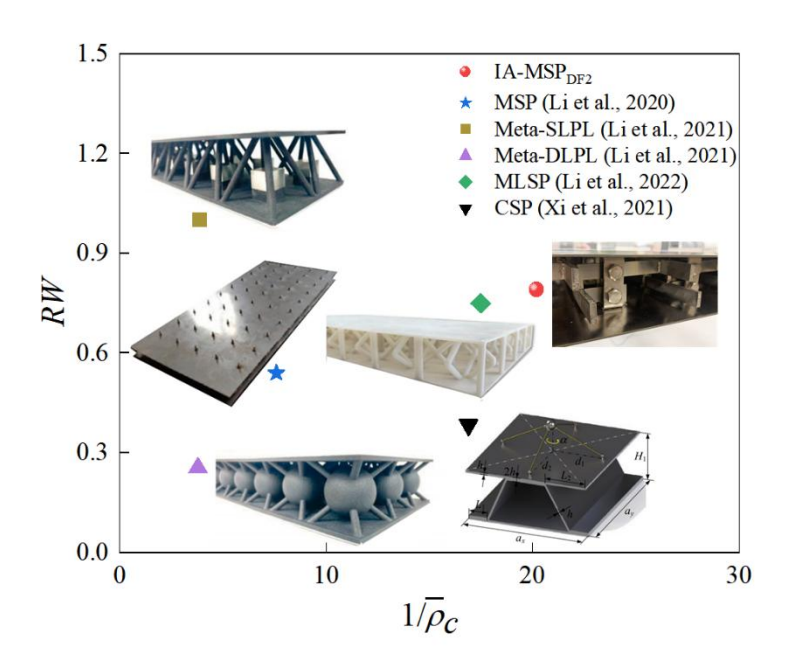


Figure 4.13 Normalized comparison of normalized attenuation bandwidth γ and the relative density $\bar{\rho}_c$ between the proposed IA-MSP_{DF2} and other metamaterial sandwich plates.

4.2.4 Effect of Damping on Bandgaps of the IA-MSP_{DF2}

To assess the effect of damping on bandgaps of IA-MSP_{DF2}, the vibration response of structures is studied at different damping ratios in numerical simulation. In engineering practice, damping materials are commonly attached to resonators to vary the damping of the structure. For this numerical simulation, the damping ratio is defined using complex elastic modulus $\tilde{C} = C (1 + i\eta_s)$ of the resonator (Qiang et al., 2021), where C is the elastic modulus of the undamped resonator, and η_s denotes the damping loss factor. Figure 4.14 presents acceleration responses of the IA-MSP_{DF2} at various damping ratios. The vibration energy in the structure is dissipated effectively due to the existence of damping. Therefore, increasing damping results in a reduction of vibration 77

intensity and amplitude, leading to smoother response curves and the merging of the two AZs into a wider AZ. Figure 4.15 illustrates vibration modes of faceplates and resonators of the IA-MSP_{DF2} with $\eta_s = 0.01$ and $\eta_s = 0.2$ at different excitation frequencies. The vibration of the IA-MSP_{DF2} at $\eta_s = 0.2$ attenuates significantly compared to that at $\eta_s = 0.01$ in the passband (450 and 690 Hz). It indicates the passband between bandgap 1 and bandgap 2 at $\eta_s = 0.2$ becomes a vibration attenuation zone. Therefore, the damping effect can merge multiple bandgaps into broad attenuation bands, which has significant implications for the design and optimization of metamaterial structures in vibration attenuation applications.

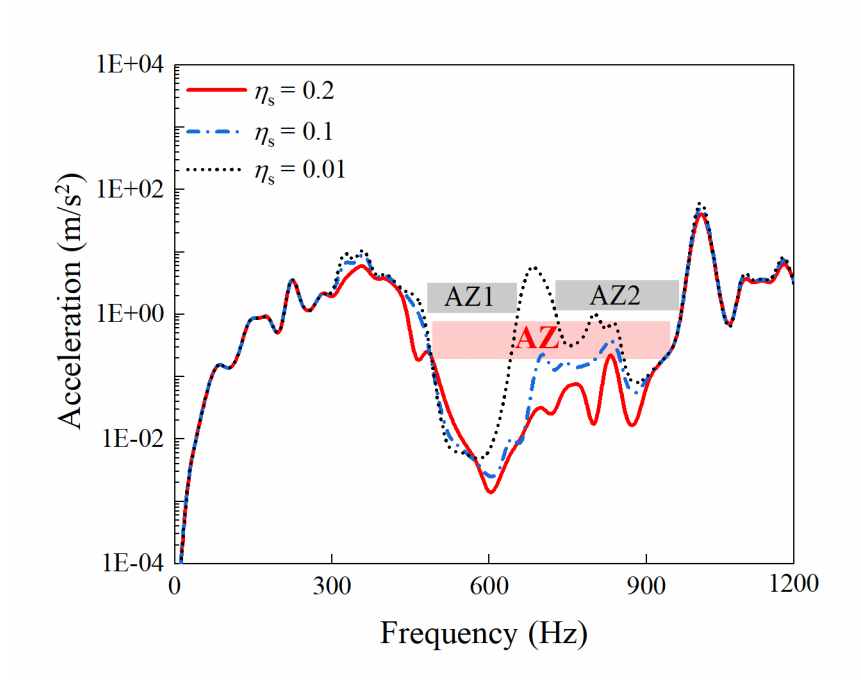


Figure 4.14 The acceleration responses of IA-MSP_{DF2} at different damping ratio.

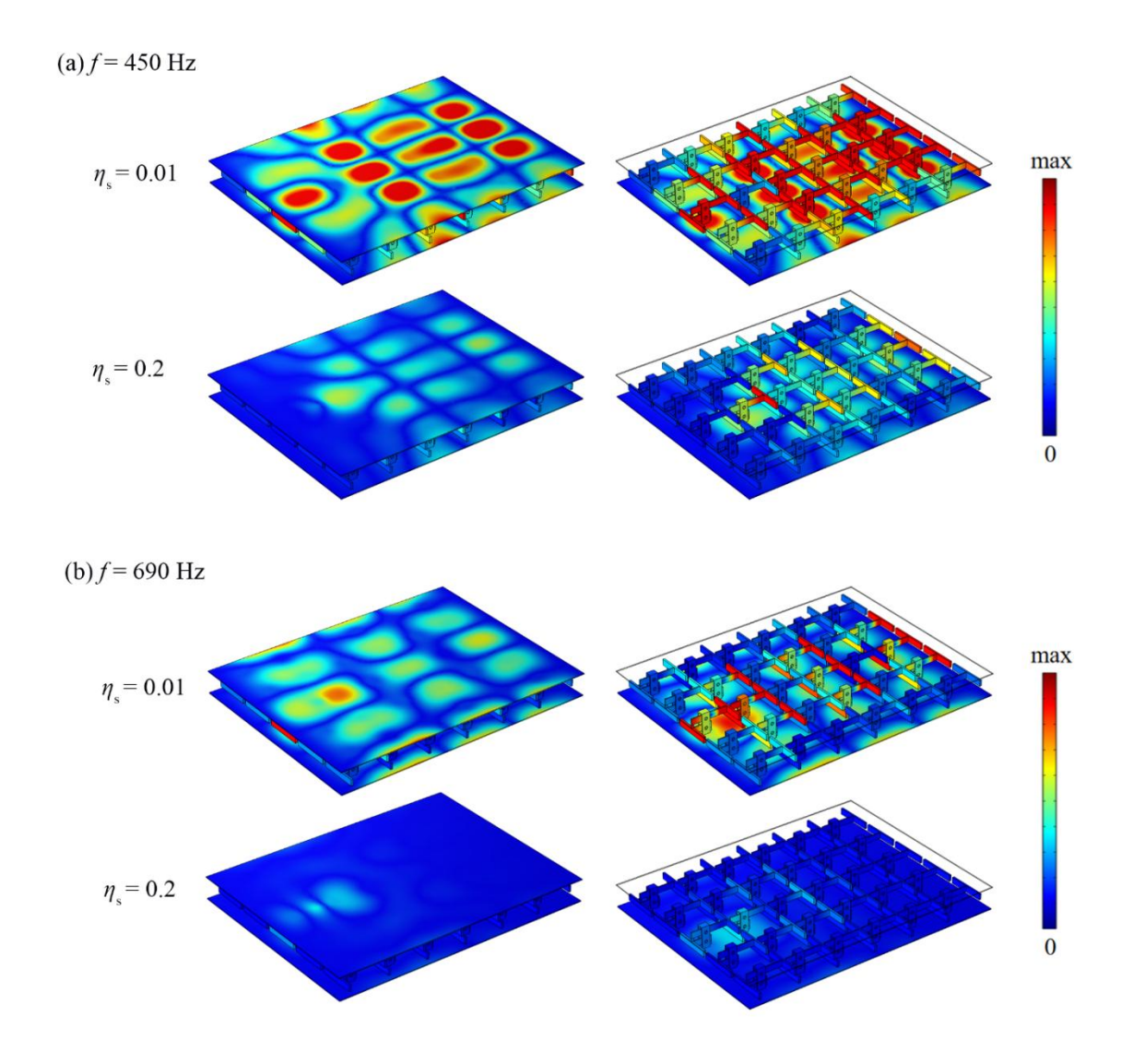


Figure 4.15 Vibration modes of faceplates and resonators of IA-MSP_{DF2} with $\eta_{\rm s}=0.01$ and $\eta_{\rm s}=0.2$ at different excitation frequencies: (a) f=450 Hz; (b) f=690 Hz.

4.3. Summary

In this chapter, a novel metamaterial sandwich plate with two-degree of freedom inertial amplified resonators (IA-MSP_{DF2}) is proposed for achieving low-frequency vibration attenuation. The IA-MSP_{DF2} consists of two face plates and a periodic array 79

of two-degree lever-type resonators. The superiority of the IA-MSP_{DF2} in achieving low-frequency and multi-bandgap vibration attenuation are fully revealed by the results of theoretical analysis, numerical simulation, and experimental study.

In theoretical analysis, a theoretical dynamic model is constructed by theoretical bandgap formulation (Eqs. (4.14-17)) in predicting the characteristics of low-frequency multiple bandgaps in the IA-MSP_{DF2}. The eigenfrequency of primary lever-type resonator can be predicted from the lever ratio R_1 , mass m_1 and spring stiffness k_1 . Similarly, the eigenfrequency of secondary lever-type resonator can be predicted from the lever ratio R_2 , mass m_2 and spring stiffness k_2 . Compared two degrees of freedom spring-mass resonators, the primary and secondary inertial masses in the proposed structure are amplified by a factor of R_1^2 and R_2^2 respectively. Therefore, the eigenfrequencies of the primary and secondary resonators are reduced by R_1 and R_2 respectively. This observation highlights that under mass constraints, fine-tuning the lever ratios allows for the realization of lower bandgaps. Notably, compared with the LR-MMSP with the same additional mass, the IA-MSP_{DF2} achieves multiple bandgaps at significantly lower frequencies. The boundary frequencies of the IA-MSP_{DF2} are 1/R of the LR-MMSP. The analytical model was also validated through the favorable agreement with the results obtained from the numerical simulation.

In the numerical simulation, the influence of different parameters on the vibration transmission characteristics of the IA-MSP_{DF2} is systematically investigated. The results indicate that a decrease in the eigenfrequencies of the primary (f_p) and secondary (f_s) resonators results in a downward shift of both AZ1 and AZ2. However, the decrease of f_p leads to the expansion of the AZ1 width. As the resonator mass ratios χ of the

secondary resonator to the primary resonator decreases, both AZ1 and AZ2 exhibit a downward shift towards lower frequencies. Simultaneously, AZ1 exhibits an expanded frequency range, accompanied by a reduction in the minimum acceleration magnitudes within both AZs. Increased mass ratio ψ of the primary resonator to the face plates results in a wider range of frequencies where significant vibration attenuation occurs. Furthermore, increasing the damping of the inertial amplified resonator reduces the vibration intensity and amplitude, which in turn leads to the merging of multiple AZs into a wider AZ.

The numerical simulation is also validated through the favorable agreement with the results obtained from experimental study. Moreover, a normalized comparison is presented to quantitatively evaluate the vibration attenuation performance and lightweight design of the proposed IA-MSP_{DF2}. The results demonstrate that the IA-MSP_{DF2} achieves a wider normalized attenuation bandwidth γ and superior lightweight design when compared to other configurations of metamaterial sandwich plates. This remarkable lightweight characteristic enhances the potential of the IA-MSP_{DF2} to offer significant advantages in various engineering applications.

Chapter 5

Precise Multi-frequency Vibration Control of the GLIA-

MSP

This chapter proposes a metamaterial sandwich plate with periodic graded arrays of lever-type inertial amplification resonators (GLIA-MSP), aiming to enhance the attenuation performance of low-frequency vibrations across multiple bands. A comprehensive framework is developed by integrating theoretical modeling, numerical simulations and genetic algorithm (GA) optimization to facilitate the design and finetuning of multi-bandgap metamaterial plates. The results demonstrate that the inertial amplification effect of the graded lever-type resonators enables the proposed GLIA-MSP to realize multiple lower frequency bandgaps beyond those of conventional metamaterial sandwich plates with periodic graded arrays of local resonators (GLR-MSP). Notably, multiple low-frequency bandgaps can be effectively achieved by simply increasing the lever ratios of resonators, without altering their mass or stiffness. GA-based optimization is employed to systematically identify the optimal configuration of lever ratios, ensuring that the bandgaps are simultaneously aligned with the designated target frequencies. Furthermore, normalized comparative analyses reveal that the bandwidth efficiency ratio (BER) of the GLIA-MSP exceeds that of other metamaterial sandwich plates, indicating its superior capability to achieve wider bandgaps with improved mass efficiency.

5.1. Methodology

This section introduces the theoretical model of GLIA-MSP and provides a detailed derivation of its dispersion relation. A finite element numerical model is then developed to investigate the vibration response. Finally, a genetic algorithm (GA) is implemented as an intelligent optimization approach to systematically search for the optimal lever ratio configurations, ensuring that the bandgaps are simultaneously tuned to their respective target values.

5.1.1 Theoretical Derivation

GLIA-MSP comprises two face plates and periodically graded arrays of lever-type IA resonators, as illustrated in Figure 5.1 (a). The corresponding unit cell is illustrated in Figure 5.1 (b). Each lever-type IA resonator comprises a spring, lever and mass, which is hinged to a supporting bar. Three types of graded lever-type IA resonators (GLIA-1, GLIA-2 and GLIA-3) are incorporated within each unit cell. To elucidate the graded lever-type IA mechanism, an equivalent analytical model of the GLIA-MSP unit cell is developed, as depicted in Figure 5.1 (c). m_1 , m_2 and m_3 are the masses of GLIA-1, GLIA-2 and GLIA-3, respectively. k_1 , k_2 and k_3 denote their corresponding spring stiffness values. R_1 , R_2 and R_3 are the lever ratios for GLIA-1, GLIA-2 and GLIA-3, respectively. In this study, the analysis is confined to the transverse vibration of the GLIA-MSP, assuming that levers are rigid and massless. The displacements of the masses GLIA-1, GLIA-2 and GLIA-3 are represented by w_1 , w_2 and w_3 , respectively,

while w_0 indicates the displacement of the plate at the origin. The displacements w, w_0 , w_1 , w_2 and w_3 are hypothesized to follow the expressions:

$$w = Ae^{i(\alpha x + \beta y - \omega t)}, \ w_0 = Ae^{-i\omega t}, \ w_1 = Be^{-i\omega t}, \ w_2 = Ce^{-i\omega t}, \ w_3 = De^{-i\omega t}$$
 (5.1)

where α and β represent wavenumbers in x- and y- directions, ω represents the wave frequency, and A, B, C and D correspond to displacement amplitudes. This study specifically focuses on the low-frequency vibration, where the wavelength greatly exceeds the lattice constant a. In this regime, the spatial variation of the face plate's displacement field is negligible over the scale of the resonator array. Therefore, it is assumed that the displacement w_0 across the resonator supports is uniform, and the phase differences among w_0 , w_1 , w_2 and w_3 are negligible.

The graded lever-type IA resonators, GLIA-1, GLIA-2, and GLIA-3, are characterized by their kinetic energies T_{r1} , T_{r2} , and T_{r3} , and elastic strain energies U_{r1} , U_{r2} , and U_{r3} , respectively, as defined below:

$$T_{r1} = \frac{1}{2} m_1 \dot{w}_1^2, \tag{5.2}$$

$$T_{r2} = \frac{1}{2} m_2 \dot{w}_2^2, \tag{5.3}$$

$$T_{r3} = \frac{1}{2} m_3 \dot{w}_3^2, \tag{5.4}$$

$$U_{r1} = \frac{1}{2} \frac{k_1}{R_1^2} (w_1 - w_0)^2, \tag{5.5}$$

$$U_{r2} = \frac{1}{2} \frac{k_2}{R_2^2} (w_2 - w_0)^2.$$
 (5.6)

$$U_{r3} = \frac{1}{2} \frac{k_3}{R_3^2} (w_3 - w_0)^2.$$
 (5.7)

The governing motion equation of the metamaterial sandwich plate derived through Hamilton's principle, expressed as:

$$\int_0^t (\delta T - \delta U + \delta T_r - \delta U_r) = 0, \qquad (5.8)$$

where $T_r = T_{r1} + T_{r2} + T_{r3}$ and $U_r = U_{r1} + U_{r2} + U_{r3}$ represent the total kinetic energy and elastic strain energy of graded lever-type IA resonators.

Inserting Eq. (5.5) into Eq. (5.8) leads to the following algebraic expressions:

$$\begin{bmatrix} \frac{8\sin\left(\frac{\alpha\alpha_x}{2}\right)\sin\left(\frac{\beta\alpha_y}{2}\right)}{\alpha\beta} \left[\rho h\omega^2 - \frac{(H^3 - (H - h)^3)}{3}\left(Q_{11}\alpha^4 + 2Q_{12}\alpha^2\beta^2 + Q_{22}\beta^4 + 4Q_{66}\alpha^2\beta^2\right)\right] - \frac{k_1}{R_1^2} - \frac{k_2}{R_2^2} - \frac{k_3}{R_3^2} & \frac{k_1}{R_1^2} & \frac{k_2}{R_2^2} & \frac{k_3}{R_3^2} \\ \frac{k_1}{R_1^2} & m_1\omega^2 - \frac{k_1}{R_1^2} & 0 & 0 \\ \frac{k_2}{R_2^2} & 0 & 0 & m_2\omega^2 - \frac{k_2}{R_2^2} & 0 \\ \frac{k_3}{R_3^2} & 0 & 0 & 0 & m_3\omega^2 - \frac{k_3}{R_3^2} \end{bmatrix} \begin{pmatrix} A \\ B \\ C \\ D \end{pmatrix} = 0, (5.9)$$

For non-zero solutions to exist in the eigenvalue problem defined in Eq. (5.9), the matrix determinant must be zero. Therefore, the dispersion relation among ω , α , and β can be obtained.

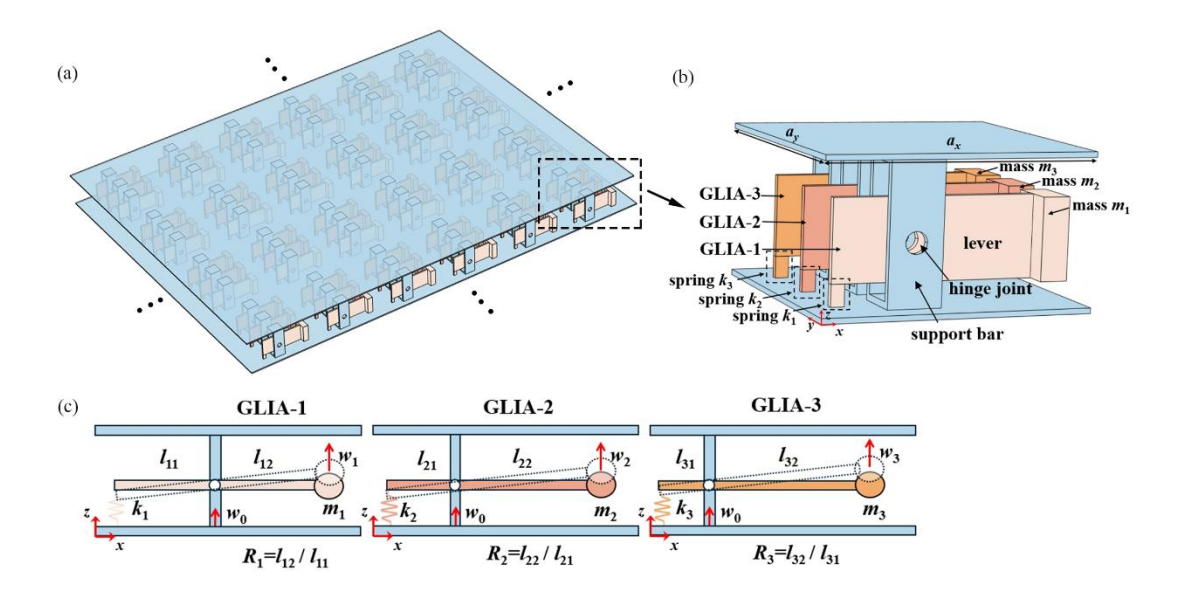


Figure 5.1 Schematic illustration of (a) GLIA-MSP; (b) unit cell of GLIA-MSP and (c) displacements of three graded lever-type IA resonators (GLIA-1, GLIA-2 and GLIA-3) in an equivalent unit cell model.

5.1.2 Vibration Response Analysis and Numerical Model

The vibration response analysis is performed using FEM. A numerical model of the GLIA-MSP comprising6×5 unit cells is established as illustrated in Figure 5.2. A vertical vibration excitation is applied at input point A. Two sides of the plate are fixed (red boundaries), whereas the other two sides are free (green boundaries). The geometric and material parameters of the GLIA-MSP are provided in Tables 5.1 and 5.2, respectively. Lever ratios R_1 , R_2 and R_3 are set to 1, 2, and 3, respectively. To discretize the model, tetrahedral mesh is used for the support bars and springs, whereas a swept mesh is employed for the remaining structural components. The vibration transmission spectrum reveals the elastic wave propagation characteristics of a structure and enables the determination of both the vibration attenuation frequency range and the degree of attenuation for the proposed system (An et al., 2024). The input

and output signals at various frequencies are recorded by sweeping the frequency across the desired range. The vibration transmissibility (VT) is then calculated as follows:

$$VT = 20 \log(\frac{|B_{out}|}{|A_{in}|}),$$
 (5.10)

where A_{in} is the displacement of the input point, and the B_{out} is the displacement of the output point. A negative value of VT indicates that the resonator effectively attenuates vibration, with a smaller VT corresponding to a higher degree of attenuation.

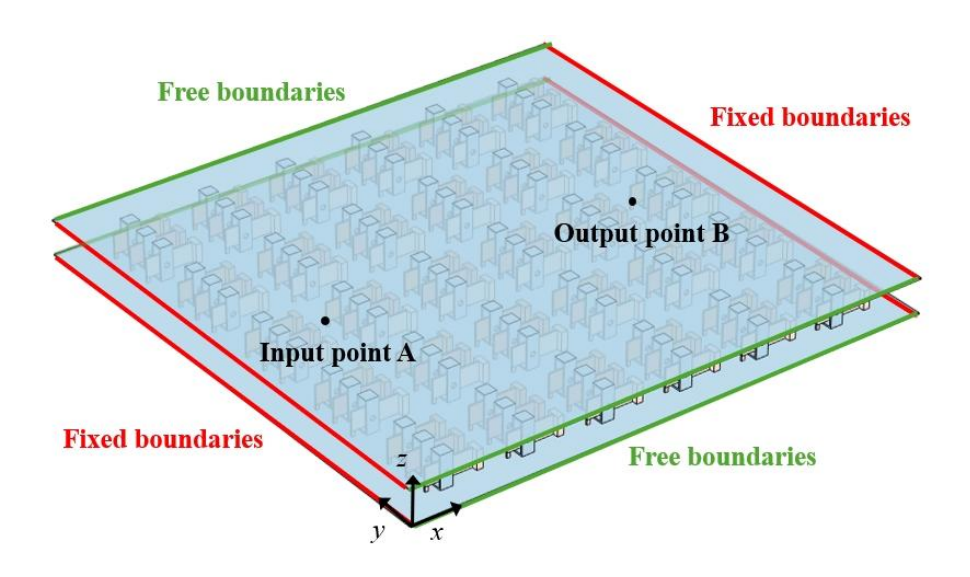


Figure 5.2 Numerical model of the GLIA-MSP comprising 6×5 unit cells.

Table 5.1 Geometrical parameters of the GLIA-MSP. ($a_x = a_y = a = 0.1 \text{ m}$)

Structure	Length, width, and height
Face plates,	6.000 <i>a</i> ×5.000 <i>a</i> ×0.020 <i>a</i>
Mass m_1 , m_2 and m_3 ,	$0.100a \times 0.200a \times 0.300a$
Lever 1, lever 2 and lever 3	$0.750a \times 0.025a \times 0.300a$

Spring k_1 , k_2 and k_3 ,	$0.050a \times 0.025a \times 0.080a$
Support bar	$0.200a \times 0.200a \times 0.530a$

Table 5.2 Material parameters of the GLIA-MSP.

Structure	Young's	Poisson	Density
	modulus	ration	(kg/m^3)
	(GPa)		
Mass (steel)	200	0.30	7850
Spring (rubber)	0.025	0.47	1300
Face plates, lever and support bar	70	0.33	2700
(aluminum)			

5.1.3 Optimization Methodology

While the GLIA-MSP is capable of achieving multiple low-frequency bandgaps, it is also essential to optimize its lever ratios (R_1 , R_2 and R_3) within a specified range to ensure bandgaps can be simultaneously tuned to their respective target values. Although only the lever ratios are considered as design variables, each lever ratio can assume an infinite number of possible values, making an exhaustive search infeasible for optimization. Furthermore, the problem is inherently multi-objective, as the center frequencies of multiple bandgaps must be optimized simultaneously. Even a small variation in the lever ratio leads to a shift in the center frequency of each corresponding bandgap, further complicating the optimization process. Given these challenges, a

global search algorithm capable of efficiently exploring the solution space is required. To address this, a genetic algorithm (GA) is employed to intelligently search for optimal lever ratio configurations.

GA is a global optimization search technique inspired by natural evolution and genetic mechanisms. One of the key advantages of GA over other stochastic optimization methods is their inherent parallelizability, as the computation of individuals within each iteration is independent, allowing for efficient parallel processing. The GA process typically consists of four fundamental operators: initialization, selection, crossover, and mutation. A critical component of GAs is the fitness function, which serves as the primary evaluation metric for assessing the quality of each individual. In this study, the objective is to optimize the lever ratios of the GLIA-MSP to achieve the desired center frequencies of the bandgaps (f_{c1} , f_{c2} and f_{c3}). For multi-objective optimization problems, a common approach is to transform multiple objective functions into a single weighted objective function, which is expressed as follows:

Minimize
$$F = \sum_{i} (\gamma_i \left| \frac{f_{ci} - f_{ci}^{\text{target}}}{f_{ci}^{\text{target}}} \right|),$$
 (5.11)

where f_{ci} and f_{ci}^{target} represent the center frequency of the *i*-th bandgap and its corresponding target center frequency, respectively. The weighting coefficient γ_i quantifies the relative importance of the *i*-th objective in the optimization process. It is evident that minimizing fitness function F leads to the optimal solution

The optimization method is presented in the flowchart in Figure 5.3, where the overall process is depicted on the left, and the core components of the GA are detailed on the right. The optimization procedure consists of the following steps: 1) Input the known 89

parameters of GLIA-MSP, including Young's modulus, density, Poisson's ratio, and mechanical properties such as m_1 , m_2 , m_3 , k_1 , k_2 and k_3 . 2) Define constraints on design variables and specify the achievable variation range for the lever ratios R_1 , R_2 and R_3 . 3) Compute the feasible range for the center frequencies (fc_1 , fc_2 and fc_3) based on the given parameters and constraints. 4) Set target values and weighting factors of the desired center frequency for the relevant bandgaps. The target values must be within the achievable range. 5) Establish termination criteria and define the stopping conditions for the optimization algorithm. The algorithm will terminate when either (i) the error between the computed and target center frequencies falls within an acceptable tolerance, or (ii) the maximum number of generations is reached. 6) Run the GA optimization process to search for the optimal lever ratios that achieve the desired bandgap properties.

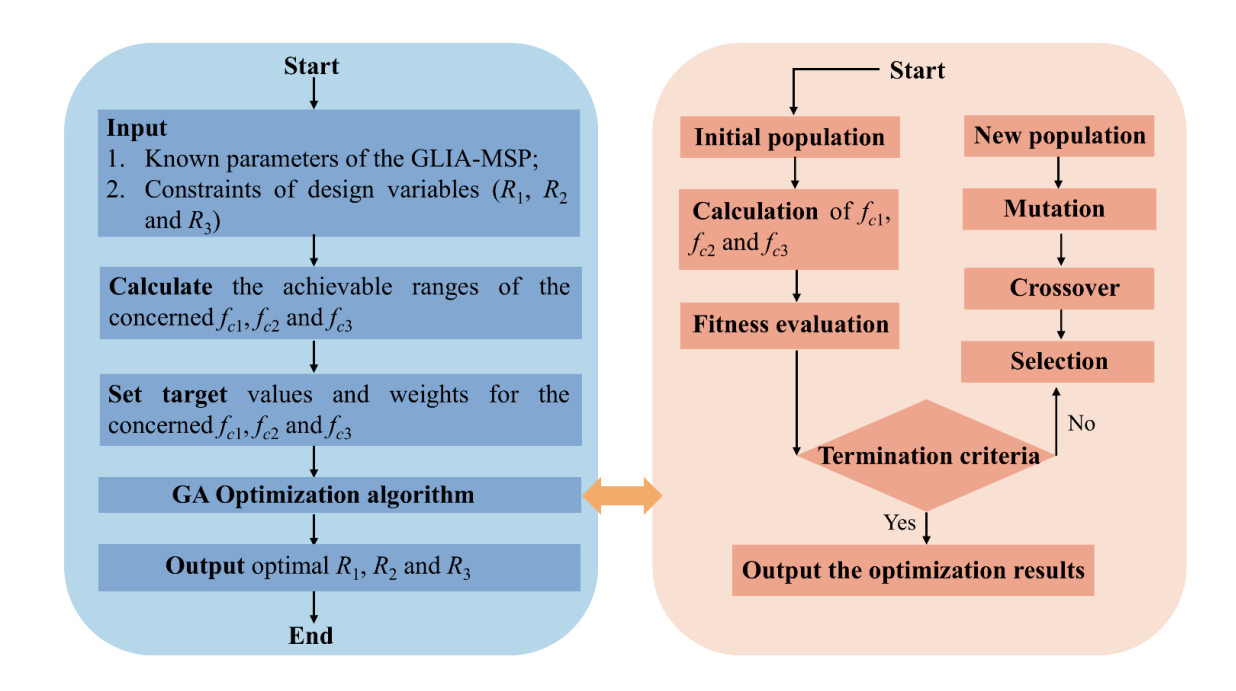


Figure 5.3 Flowchart of the GA optimization.

5.2. Results and Discussions

This section presents a comprehensive analysis of the bandgap properties and vibration suppression performance of GLIA-MSP. The reliability of the theoretical model is confirmed by its agreement with FEM results. Bandgap characteristics of the GLIA-MSP are then compared with those of a conventional metamaterial sandwich plate with periodic graded arrays of local resonators (GLR-MSP). Additionally, the effect of lever ratios on the bandgap properties of GLIA-MSP is examined. Finally, the proposed GA is employed to optimize the lever ratios (R_1 , R_2 and R_3) to ensure that the bandgaps are simultaneously tuned to their respective target values.

5.2.1 Dispersion Relationship and Vibration Transmission Research

The bandgap location and width of the GLIA-MSP can be determined by calculating the dispersion relationship using Eq. (5.9) in Section 5.1.1. For the validation of the theoretical dispersion equation presented in Section 5.1.1, the structural parameters of the GLIA-MSP used in the theoretical model are set to match those of the numerical model in Section 5.1.2 (Tables 5.1 and 5.2). The specific parameter values are as follows: $m_1 = m_2 = m_3 = 47$ g, $k_1 = k_2 = k_3 = 39,063$ N/m, M = 108 g, $R_1 = 1$, $R_2 = 2$ and $R_3 = 3$. Figure 5.4 (a) illustrates the dispersion surfaces of the GLIA-MSP, while Figures 5.4 (b) and (c) present the front and magnified views of the dispersion surfaces for clarity. The results indicate the presence of three distinct bandgaps, located between 48–54 Hz, 72–83 Hz and 145–177 Hz. These bandgaps are attributed to the local resonance frequencies of the three graded lever-type IA resonators (GLIA-1, GLIA-2 and GLIA-3), with each resonator influencing a specific bandgap.

A numerical simulation is performed to calculate the VT of the GLIA-MSP to assess and confirm the vibration attenuation performance. The transmission curve shown in Figure 5.4 (d) reveals three distinct attenuation zones (AZs) that correspond to frequency ranges similar to the theoretical bandgap results. This validates the accuracy of the dispersion relation in Eq. (5.9) from Section 5.1.1. To clarify the mechanism of bandgap formation, vibration modes at the excitation frequencies of 54, 70, 77, 103, 140, and 175 Hz are illustrated in Figure 5.4 (e). The frequencies of 54, 77, and 140 Hz fall within bandgap 1, bandgap 2, and bandgap 3, respectively, while 70, 103, and 175 Hz lie outside these bandgaps. At frequency outside the bandgaps (70, 103, and 175 Hz), vibration waves propagate without obstruction. However, significant attenuation is within the bandgap 1 (54 Hz), bandgap 2 (77 Hz) and bandgap 3 (140 Hz). These results demonstrate GLIA-MSP's excellent vibration suppression performance within the bandgap regions. Additionally, the excitation at 54 Hz induces strong vibrations in GLIA-3, at 77 Hz in GLIA-2, and at 140 Hz in GLIA-1, confirming that the vibration attenuation observed in bandgap 1, bandgap 2 and bandgap 3 is driven by local resonance in the GLIA-3, GLIA-2 and GLIA-1 resonators, respectively. Therefore, tuning the resonance frequencies of the GLIA-1, GLIA-2, and GLIA-3 resonators enables the precise control of bandgap formation, facilitating targeted vibration attenuation over a specific frequency range. Notably, this is achieved without modifying the mass or stiffness of the resonators. Instead, adjusting the lever ratio provides a straightforward and efficient approach to tailoring the bandgap properties.

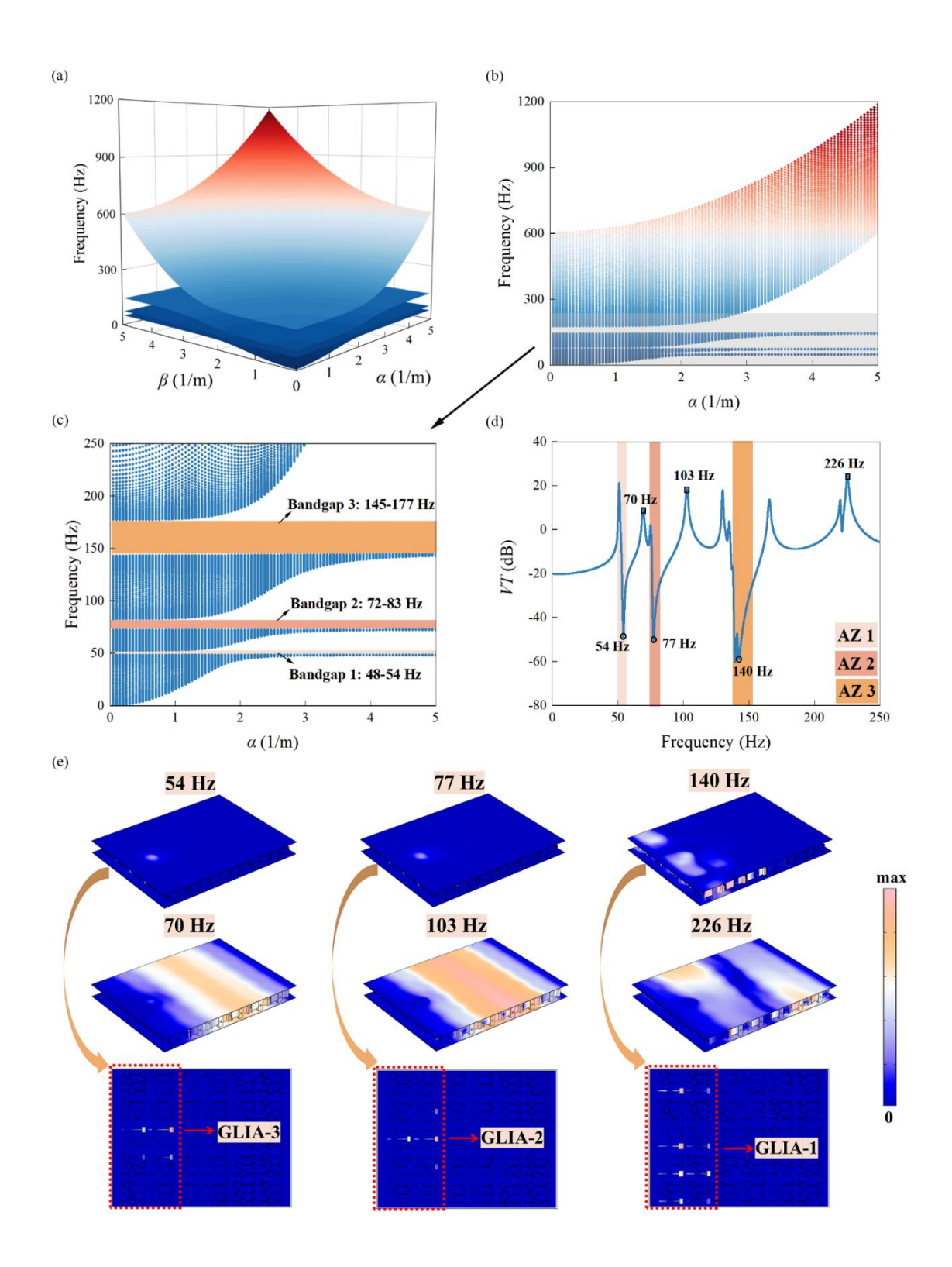


Figure 5.4 Theoretical and numerical results. (a) 3D view of dispersion surfaces of the GLIA-MSP; (b) front view; (c) magnified view; (d) vibration transmissibility of GLIA-

MSP with 6×5 unit cells and (e) vibration modes of GLIA-MSP at the excitation frequencies of 54, 70, 77, 103, 140, and 175 Hz.

5.2.2 Comparative Study and Effect of Lever Ratios

In this section, the bandgap characteristics of GLIA-MSP are compared with those of the conventional metamaterial sandwich plate with periodic graded arrays of local resonators (GLR-MSP). The effect of lever ratios on the bandgaps of GLIA-MSP is also investigated. Additionally, the vibration transmissibility is analyzed and compared to further demonstrate the efficacy of the proposed GLIA-MSP. To ensure a direct comparison, the structural parameters of both GLIA-MSP and GLR-MSP are set to identical values: $m_1 = m_2 = m_3 = 47$ g, $k_2 = 39,063$ N/m, $k_1 = k_2/2$, $k_3 = 2$ k_2 and M = 108 g. Figure 5.5 (a) and Table 5.3 present a comparison of the theoretical bandgap distributions for both structures, considering different lever ratios. In the GLIA-MSP model, all three resonators (GLIA-1, GLIA-2, and GLIA-3) are assigned to the same lever ratio ($R_1 = R_2 = R_3$). Notably, the GLR-MSP is equivalent to the GLIA-MSP when the lever ratio is set to $(R_1 = R_2 = R_3 = 1)$. As illustrated in Figure 5.5 (a), the bandgap frequencies of GLIA-MSP are consistently lower than those of GLR-MSP. Furthermore, as the lever ratio increases, both the boundary frequencies and the center frequency (f_c) of bandgaps in GLIA-MSP decrease, demonstrating the effect of inertial amplification on bandgap formation. Table 5.3 provides a detailed comparison of the three bandgap ranges for GLIA-MSP with varying lever ratios alongside those of GLR-MSP. To quantify the total bandgap width, the concept of relative bandwidth (RW) is introduced:

$$RW = \sum_{i=1}^{n} \frac{f_{ui} - f_{li}}{f_{ci}},$$
 (5.12)

where f_{ui} , f_{li} and f_{ci} represent the upper boundary frequency, lower boundary frequency, and center frequency of the i-th bandgap, respectively. A higher RW value indicates a wider bandgap, signifying greater vibration attenuation capability. The bandgap boundary frequencies of GLIA-MSP scale as 1/R relative to those of GLR-MSP. Given that both structures maintain the same resonator mass and exhibit similar RWs, the inertial amplification effect of lever resonator enables GLIA-MSP to achieve lower-frequency bandgaps compared to GLR-MSP.

Figure 5.5 (b) further compares the vibration transmissibility of GLIA-MSP ($R_1 = R_2 = R_3 = 1.5$) and GLR-MSP, both configured with a 6×5 unit cell arrangement. The results indicate that the attenuation zones (AZ1, AZ2, and AZ3) of GLIA-MSP occur at lower frequencies than those of GLR-MSP. The frequencies at troughs of GLIA-MSP (70 Hz, 99 Hz and 138 Hz) are approximately 2/3 of those in GLR-MSP (114 Hz, 163 Hz and 232Hz), further confirming the accuracy of the theoretically derived bandgap predictions. In addition, the effect of lever ratios on the vibration transmissibility of GLIA-MSP is examined. As shown in Figure 5.6, increasing the lever ratio causes the AZs to move to lower frequency regions. Furthermore, the frequencies at troughs decrease as the lever ratio increases. This indicates that multiple vibration attenuation zones at lower frequencies are achieved solely by increasing the lever ratio of resonators, without the need to increase mass or reduce stiffness. This approach enables effective low-frequency vibration suppression while maintaining a lightweight structural design, offering a practical and efficient solution for engineering applications requiring both high performance and minimal additional mass.

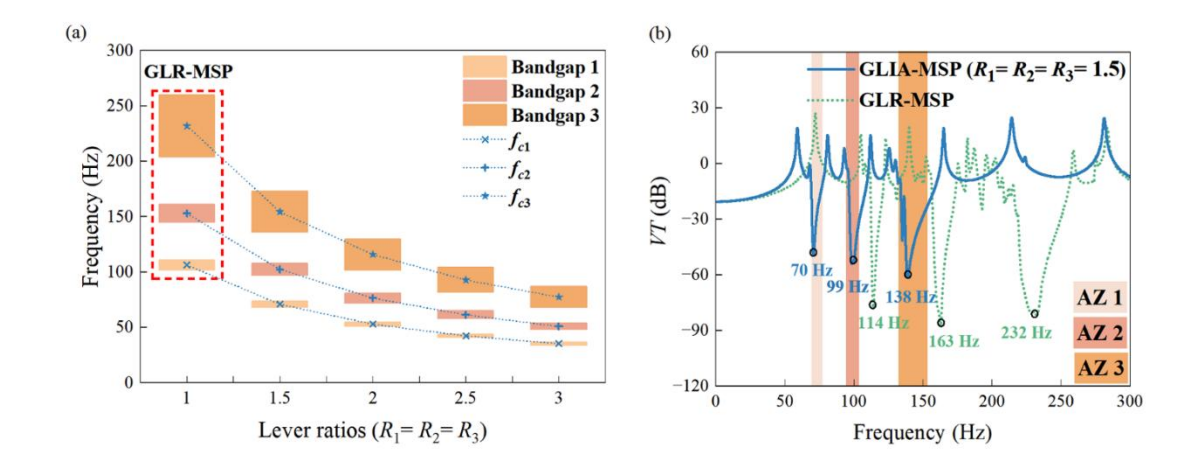


Figure 5.5 Comparison of bandgap characteristics between GLIA-MSP and GLR-MSP.

(a) Theoretical bandgap distributions; (b) Vibration transmissibility of GLIA-MSP $(R_1 = R_2 = R_3 = 1.5)$ and GLR-MSP.

Table 5.3 Comparison of bandgaps for GLIA-MSP with varying lever ratios alongside those of GLR-MSP.

Structure	Bandgap 1	Bandgap 2	Bandgap 3	Relative bandwidth (RW)	
GLR-MSP	102-111 Hz	145-161 Hz	204-260 Hz	0.418	
GLIA-MSP $(R_1 = R_2 = R_3 = 1.5)$	68-74 Hz	97-108 Hz	136-173 Hz	0.411	
GLIA-MSP $(R_1 = R_2 = R_3 = 2)$	51-55 Hz	72-81 Hz	102-130 Hz	0.409	
GLIA-MSP $(R_1 = R_2 = R_3 = 2.5)$	41-44 Hz	58-65 Hz	82-104 Hz	0.408	
GLIA-MSP $(R_1 = R_2 = R_3 = 3)$	34-37 Hz	48-54 Hz	68-87 Hz	0.407	

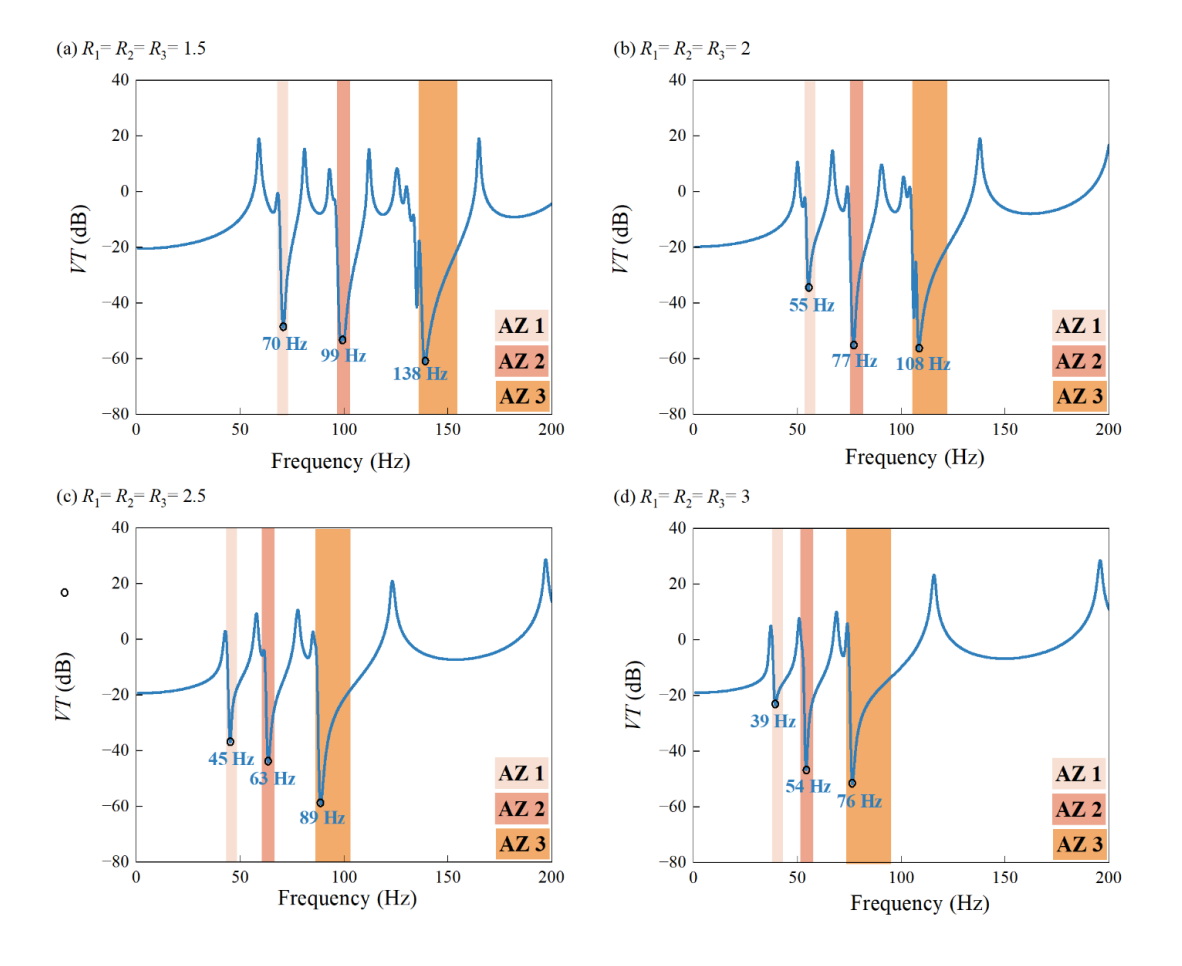


Figure 5.6 Effect of lever ratios on the vibration transmissibility of GLIA-MSP: (a) R_1 = R_2 = R_3 = 1.5; (b) R_1 = R_2 = R_3 = 2; (c) R_1 = R_2 = R_3 = 2.5 and (d) R_1 = R_2 = R_3 = 3.

In previous studies, the plate was constrained with clamped boundary conditions on the two short sides while leaving the two long sides free. In this section, we further investigate the influence of boundary conditions on the vibration transmissibility of the GLIA-MSP. Figure 5.7 presents the vibration transmissibility of a GLIA-MSP (R_1 = R_2 = R_3 = 1.5) with a 6×5 unit cell arrangement under three distinct boundary conditions: (1) clamped short sides and free long sides, (2) simply-supported short sides and free long sides, and (3) fully free boundaries (all sides free). The results reveal that despite the variation in boundary conditions, the frequency range of the AZ remains largely consistent. This suggests that the bandgap characteristics are primarily governed by the 97

unit cell design rather than the boundary constraints. However, it is noteworthy that the attenuation performance under free boundary conditions is inferior to that observed under clamped or simply-supported conditions. This difference may be attributed to the fact that free boundaries permit wave transmission, whereas clamped and simply-supported boundaries reflect waves, thereby promoting energy localization and dissipation within the resonators. Additionally, Figure 5.8 illustrates the vibration transmissibility of the GLIA-MSP across different damping ratios. As the damping ratio increases, the *VT* curve becomes smoother, and its peak amplitude significantly decreases. This behavior occurs because damping enhances energy dissipation within the structure. Consequently, the three original attenuation zones merge into a broader AZ, demonstrating improved vibration suppression performance.

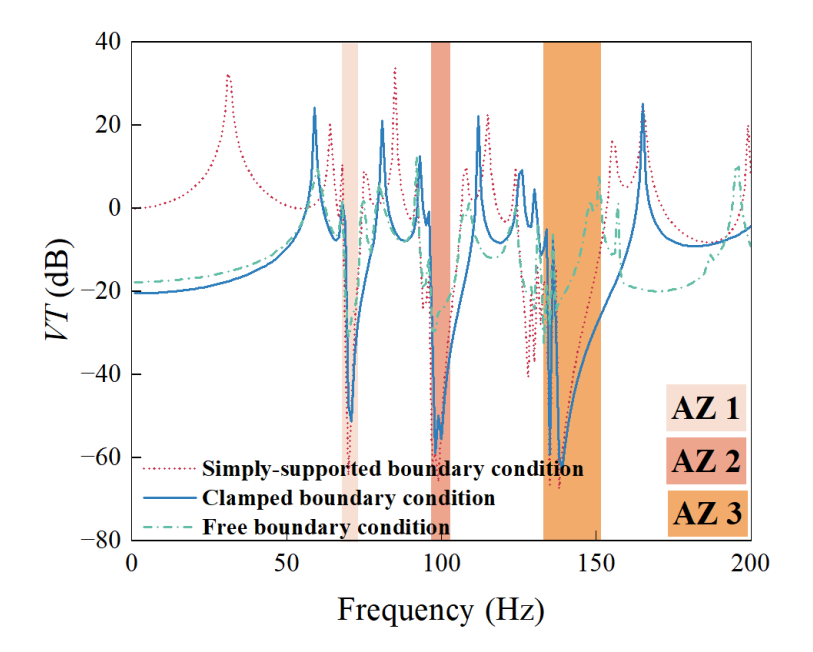


Figure 5.7 Vibration transmissibility of GLIA-MSP ($R_1 = R_2 = R_3 = 1.5$) with a 6×5 unit cell arrangement under different boundary conditions.

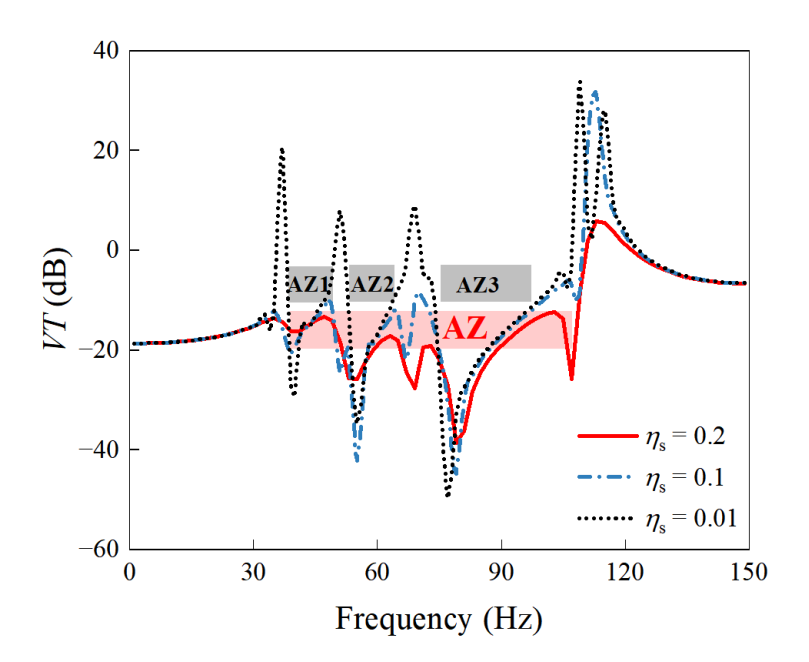


Figure 5.8 Vibration transmissibility of GLIA-MSP ($R_1 = R_2 = R_3 = 3$) at different damping ratio.

5.2.3 Optimization and Normalized Comparison

In this section, the proposed GA is implemented to optimize the lever ratios (R_1 , R_2 and R_3) of the GLIA-MSP to ensure that the bandgaps can be simultaneously adjusted to their respective target values. In the GA method, the initial population size is 100, the maximum number of generations is limited to 500, and the stall generation is set to 50. The crossover rate and mutation rate are 0.8 and 0.08, respectively. The target center

frequencies of the relevant bandgaps $(f_{c1}, f_{c2} \text{ and } f_{c3})$ can be freely assigned within the achievable range. The termination criteria of the optimization algorithm are established as follows: 1) the fitness function F reaches a tolerance threshold of 0.1% error ($F \le 0.1\%$). 2) The average improvement in fitness remains below 1×10^{-6} for 50 stall generations. 3) If the above optimization criterion is not met, the algorithm proceeds until the predefined maximum number of generations is reached, at which point it terminates and outputs the best solution found. These conditions ensure a balance between computational efficiency and solution accuracy, allowing the GA to effectively converge toward an optimal design while preventing excessive computational cost.

The optimization results for a specific case are presented in Table 5.4. In this case, the known parameters are based on those defined in Section 5.2.2. The design variables, namely the lever ratios (R_1 , R_2 and R_3), are constrained within the range of 1 to 5. Through computational analysis, the achievable frequency ranges for the center frequencies f_{c1} , f_{c2} and f_{c3} are determined to be 26.2–169.7 Hz, 46.2–228.5 Hz, and 70.7–230.5 Hz, respectively. The optimization targets for these frequencies are set at 50 Hz, 100 Hz, and 150 Hz, with equal weighting factors of $\gamma_1 = \gamma_2 = \gamma_3 = 1$. The GA optimization yields the optimal lever ratios as $R_1 = 2.15$, $R_2 = 1.52$, and $R_3 = 1.53$. These values successfully adjust the center frequencies to 50 Hz, 100 Hz, and 150 Hz, respectively, achieving an exact match with the target values, with a deviation of 0%. Figures 5.9 (a) and (b) present the theoretical and numerical optimization results. The obtained frequency ranges of AZ1, AZ2, and AZ3 are clearly identified. Notably, the optimized AZs exhibit strong agreement with the theoretically predicted bandgap frequencies and effectively encompass the target bandgap center frequencies. These 100

results validate the effectiveness of the proposed optimization approach in accurately tuning the bandgap frequencies of GLIA-MSP, demonstrating its capability to achieve precise vibration attenuation within the desired frequency range.

Table 5.4 Optimization results of the GLIA-MSP

Known parameters	Young's	Densit v	Poisson' s ratio	<i>m</i> ₁ (kg)	<i>m</i> ₂ (kg)	<i>m</i> ₃ (kg)	k ₁ (N/m)	k ₂ (N/m)	k ₃ (N/m)
of the	modulu	(kg/m ³	5 Iulio	(NS)	(NS)	(115)	(14/11)	(11/111)	(14/11)
GLIA-MSP	s (GPa))							
	70	2700	0.33	0.04	0.04	0.04	19,53	39,06	78,12
				7	7	7	1	3	5
Constraints		R_1		R_2			R_3		
of design		1~5			1~5		1~5		
variables									
Achievable	$f_{c1} \in [26.2, 169.7], f_{c2} \in [46.2, 228.5], f_{c3} \in [70.7, 230.5],$								
ranges of									
the									
concerned									
fc_1, fc_2 and									
fc_3		1	- torget	- tor	ret	tora	ret		
Optimizatio	Target va	alues	$f_{c1}^{\text{target}} = 3$	50, f_{c2}^{targ}	$g^{et} = 10$	$00, f_{c3}^{\text{targ}}$	$e^{1} = 150$		
n target	(Hz)								
	Weights		$\gamma_1=1,\gamma_2=$						
Optimizatio	Lever ratios $R_1 = 2.15, R_2 = 1.52, R_3 = 1.53$								
n results	Bandgaps (Hz) Bandgap 1: 47.7~52.3, bandgap 2: 95.1~104.9, bandgap					ıp			
	3:133.4~166.6								
	Center frequencies $f_{c1} = 50, f_{c2} = 100, f_{c3} = 150$								
	(Hz)								
	Deviation 0% , 0% , and 0% for $i=1, 2$ and 3 , respectively								
	$\left \frac{f_{ci} - f_{ci}^{\text{target}}}{f_{ci}} \right ^{\text{target}}$								

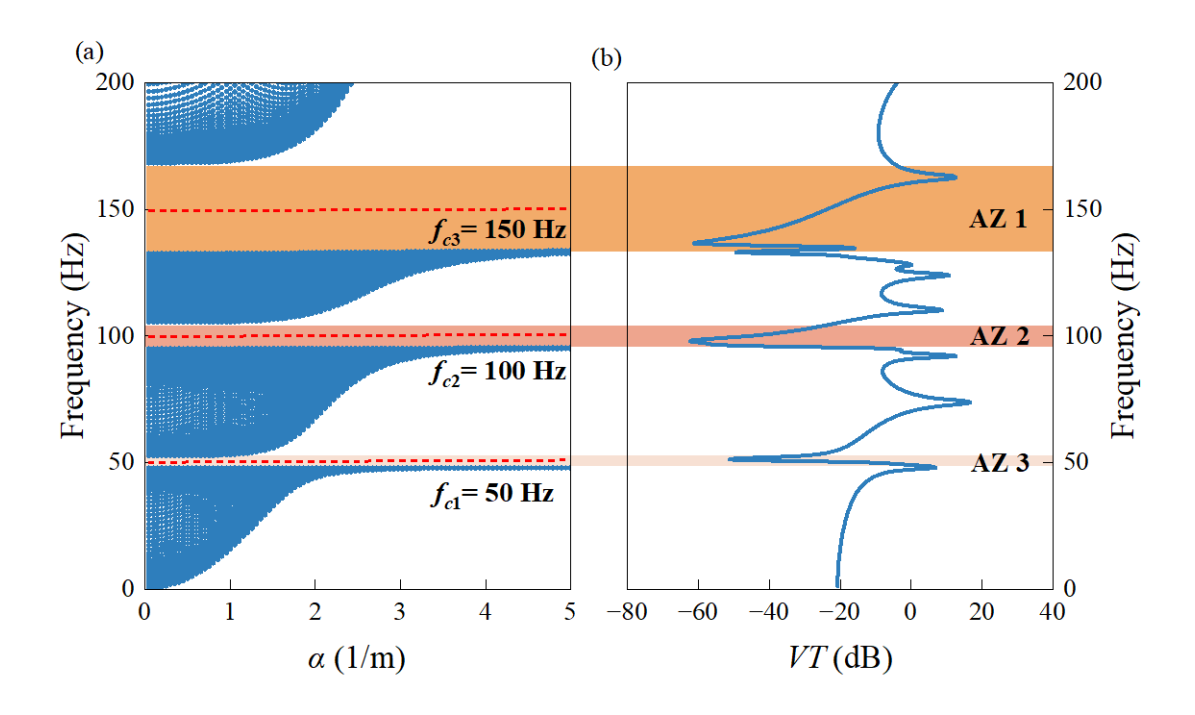


Figure 5.9 Optimization results for target bandgap center frequencies (50 Hz, 100 Hz, 150 Hz): (a) dispersion surfaces of the GLIA-MSP and (b) vibration transmissibility of GLIA-MSP with 6×5 unit cell configuration.

Furthermore, a normalized comparison is conducted to assess the bandgap width and lightweight characteristics of the GLIA-MSP. Figure 5.10 illustrates the comparison of relative bandwidth (RW), relative core density $\bar{\rho}_c$ and bandwidth efficiency ratio (BER) between GLIA-MSP and other metamaterial sandwich plates. The relative core density, defined as $\bar{\rho}_c = \rho_c/\rho$ is used as an indicator of the lightweight efficiency of the structure (Z. Xue & Hutchinson, 2004), where ρ_c represents the average density of core layer, and ρ represents the density of host structure material. The core layer density ρ_c is further calculated as $\rho_c = \frac{m_c}{V_c}$, with m_c and V_c denoting the mass and volume of the core layer, respectively. In Figure 5.10, the y-axis shows the reciprocal of the average core density $\bar{\rho}_c$, such that higher values indicate lighter core layers and improved

lightweight characteristics. In contrast, the x-axis reflects the normalized attenuation bandwidth, with greater values indicating broader frequency suppression ranges. As shown in Figure 5.10, the GLIA-MSP achieves a wider bandgap while maintaining a lower core density, demonstrating a superior balance between lightweight design and vibration suppression capability in comparison with other metamaterial sandwich plates. To further quantify the bandwidth contribution per unit mass of the resonator, the bandwidth efficiency ratio (BER) is introduced:

$$BER = \frac{RW}{\overline{\rho}_c}. (5.13)$$

This parameter represents the total relative bandwidth that can be achieved per unit of relative resonator mass, thereby serving as an efficiency metric for evaluating vibration suppression performance. A higher *BER* signifies that the resonator can generate a wider bandgap with a relatively lower mass, indicating a more efficient design. The size and color intensity of the circles in Figure 5.10 represent the magnitude of the *BER* value. Larger areas and darker colors correspond to higher *BER* values. The comparative results in Figure 5.10 reveal that the *BER* of GLIA-MSP exceeds that of other metamaterial sandwich plates, indicating that GLIA-MSP can achieve wider vibration suppression bandgaps with greater mass efficiency. This highlights the superior performance of GLIA-MSP in realizing low-frequency vibration control with an optimized lightweight structure.

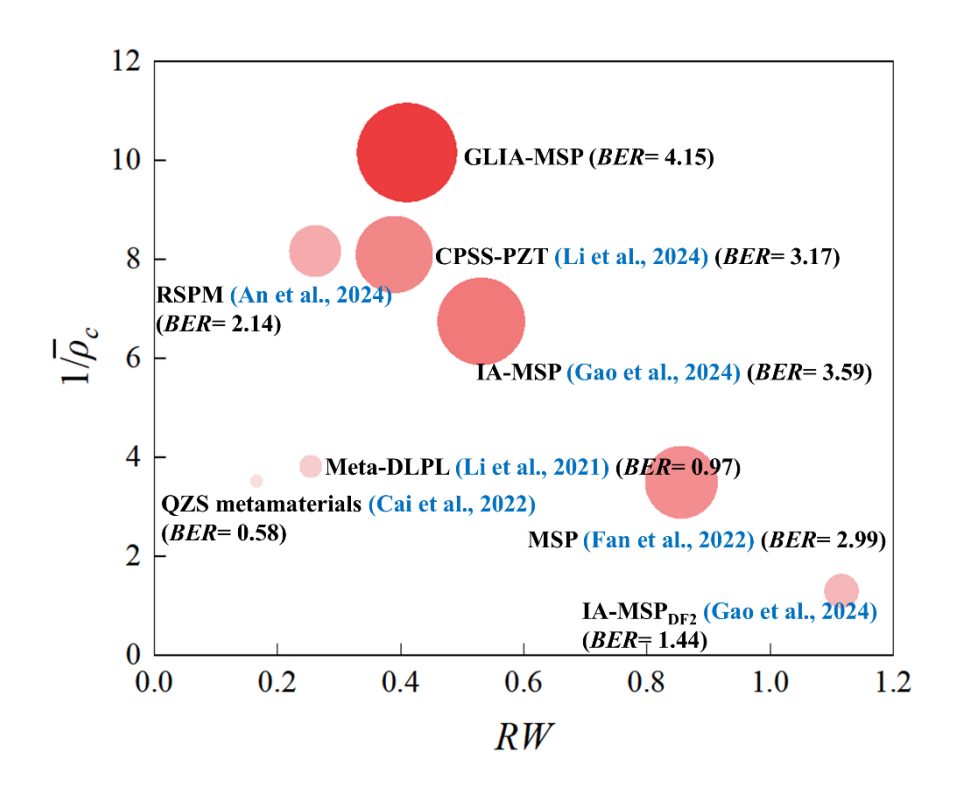


Figure 5.10 Normalized comparison of relative bandwidth (RW), relative density $\bar{\rho}_c$ and bandwidth efficiency ratio (BER) between GLIA-MSP and other metamaterial sandwich plates.

5.3. Summary

In this chapter, a novel metamaterial sandwich plate with periodic graded arrays of lever-type IA resonators (GLIA-MSP) is proposed to achieve effective low-frequency vibration attenuation over multiple frequency bands. The superiority of GLIA-MSP in precisely attenuating low-frequency vibration across multiple target frequency ranges is demonstrated through theoretical analysis, numerical simulations and genetic algorithm (GA) optimization.

From the theoretical analysis, a comprehensive theoretical model of GLIA-MSP is established, and a detailed derivation of its dispersion relation is presented to predict the characteristics of multiple low-frequency bandgaps. The formulation of bandgap 1, bandgap 2 and bandgap 3 is attributed to the local resonance of the graded lever-type IA resonators (GLIA-1, GLIA-2 and GLIA-3), respectively. The bandgap boundary frequencies of GLIA-MSP are found to scale as 1/R relative to those of conventional multi-bandgap metamaterial sandwich plate with periodic graded arrays of local resonators (GLR-MSP). Given that both structures maintain the same resonator mass and exhibit similar relative bandwidths (RWs), the inertial amplification effect of lever-type resonators enables GLIA-MSP to achieve lower-frequency bandgaps compared to GLR-MSP. Theoretical model accuracy is further validated through its strong agreement with numerical simulation results.

Numerical simulations are conducted using a FEM model to investigate the vibration response of the GLIA-MSP. The attenuation zones (AZ1, AZ2, and AZ3) of GLIA-MSP are observed at lower frequencies compared to those of GLR-MSP. When the lever ratios are set as $R_1 = R_2 = R_3 = 1.5$, the trough frequencies of GLIA-MSP (70 Hz, 99 Hz and 138 Hz) are approximately 2/3 of those in GLR-MSP (114 Hz, 163 Hz and 232Hz). Moreover, increasing the lever ratio causes the AZs to shift downward toward lower frequencies, with the trough frequencies decreasing as the lever ratio increases. This demonstrates that multiple low-frequency vibration AZs can be effectively realized by simply increasing the lever ratio of resonators, without modifying the resonator mass or stiffness. Such an approach enables efficient low-frequency vibration suppression while maintaining a lightweight structural design, providing a practical and

efficient solution for engineering applications requiring both high performance and minimal additional mass.

Additionally, the GA is employed as an intelligent optimization strategy to systematically search for the optimal lever ratio configurations, ensuring that the bandgaps are simultaneously tuned to their respective target values. The optimization targets for the center frequencies are set at 50 Hz, 100 Hz, and 150 Hz, with equal weighting factors ($\gamma_1 = \gamma_2 = \gamma_3 = 1$). The GA optimization yields the optimal lever ratios as $R_1 = 2.15$, $R_2 = 1.52$, and $R_3 = 1.53$, successfully adjusting the center frequencies to the desired 50 Hz, 100 Hz, and 150 Hz, with a deviation of 0%, demonstrating the accuracy of the optimization approach. The normalized comparative results reveal that the bandwidth efficiency ratio (BER) of GLIA-MSP exceeds that of other metamaterial sandwich plates, indicating that GLIA-MSP can achieve wider vibration suppression bandgaps with greater mass efficiency.

Chapter 6

Conclusions and Suggestions for Future Work

6.1. Conclusion

This thesis presents a systematic investigation into the design, analysis, and optimization of novel metamaterial sandwich plates embedded with lever-type inertial amplification (IA) resonators for achieving effective low-frequency and multi-bandgap vibration attenuation. The work addresses several critical limitations in traditional locally resonant (LR) metamaterials, such as the need for bulky resonators, narrow bandgap bandwidths, and poor tunability in multi-frequency applications.

In the first part of the study, a metamaterial sandwich plate with lever-type IA resonators (IA-MSP) is proposed. A theoretical model is developed to derive the dispersion relation and predict bandgap characteristics. Numerical simulations and experimental results demonstrate that IA-MSP can achieve significantly lower bandgap frequencies than conventional LR-MSP with equivalent mass and stiffness parameters. The reduction in bandgap frequency is attributed to the effective mass enhancement induced by the lever-type amplification, which shifts the bandgap toward lower frequencies without increasing the physical mass. This proves the feasibility of using IA mechanisms to break the long-standing trade-off between mass and low-frequency isolation in metamaterial designs.

Building on this concept, a two-degree-of-freedom configuration (IA-MSP_{DF2}) is developed to further improve multi-bandgap vibration attenuation. Theoretical modeling reveals that the eigenfrequencies of the primary and secondary resonators are inversely proportional to the square of their respective lever ratios. Numerical and experimental results confirm that IA-MSP_{DF2} can generate two distinct low-frequency attenuation zones (AZ1 and AZ2), which can be tuned independently through lever ratio adjustment. Parametric studies show that modifying resonator mass, stiffness and damping can control the location, width and depth of the attenuation zones. Moreover, normalized comparisons demonstrate that the IA-MSP_{DF2} outperforms conventional LR-based designs in both attenuation bandwidth and lightweight efficiency, making it suitable for applications with stringent space and mass constraints.

In the final phase, a graded lever-type IA metamaterial sandwich plate (GLIA-MSP) is proposed to achieve precise and simultaneous control of multiple bandgaps across target frequency ranges. A theoretical framework is established to derive the bandgap dispersion relation for graded IA resonators (GLIA-1, GLIA-2, GLIA-3). Finite element simulations show that the GLIA-MSP achieves lower and broader attenuation zones compared to GLR-MSPs. Importantly, it is demonstrated that the bandgap frequencies scale inversely with the lever ratio, allowing for efficient low-frequency control without modifying resonator mass or stiffness. To further enhance design adaptability, a genetic algorithm (GA)-based optimization strategy is employed. The GA successfully identifies optimal lever ratio configurations that precisely align the bandgaps with pre-defined target frequencies (50 Hz, 100 Hz, and 150 Hz), achieving 0% deviation. The high bandwidth efficiency ratio (*BER*) of the GLIA-MSP confirms its superior performance in multi-band low-frequency vibration control.

Overall, this thesis establishes a comprehensive hybrid framework—integrating theoretical modeling, numerical simulation, experimental validation, and intelligent optimization—for the design of high-performance, lightweight, and tunable metamaterial sandwich plates with enhanced vibration attenuation capabilities. The outcomes of this study are expected to provide significant insights into the design principles governing metamaterial plates to achieve effective vibration control.

6.2. Suggestions for Future Work

Although the present study demonstrates the potential of lever-type inertial amplification metamaterial sandwich plates, several areas remain open for further exploration:

The current study focuses on linear, time-invariant lever-type IA metamaterial systems. However, many real-world engineering structures are subject to nonlinear dynamic behavior. Incorporating nonlinear stiffness elements—such as geometric nonlinearity or nonlinear springs—into IA resonators may allow for amplitude-dependent bandgaps, leading to adaptive vibration attenuation under varying excitation conditions. In addition, introducing time-varying parameters, such as switchable stiffness or variable mass elements, may enable effective vibration control of lever-type IA metamaterial sandwich plates.

While the proposed lever-type IA metamaterial sandwich plates rely on passive mechanical configurations, integrating active control strategies could offer greater adaptability and real-time tunability. For instance, embedding piezoelectric patches, electromagnetic actuators, or shape memory alloys into the resonator structure would 109

allow dynamic adjustment of mass, stiffness or damping in response to changing operational conditions. This integration could facilitate active bandgap tuning, vibration suppression on demand, or multi-mode switching, greatly expanding the scope of applications in aerospace, precision equipment, and adaptive structures.

Although this study includes experimental verification under controlled conditions, further validation under realistic engineering environments is essential to demonstrate the robustness and practical feasibility of the proposed lever-type IA metamaterial designs. Future work should consider implementing the metamaterial sandwich plate in full-scale structural components, such as aircraft fuselage panels, railway floorboards or marine bulkheads, subject to multi-point excitation, random or broadband loads and variable boundary constraints.

The current optimization approach focuses on aligning bandgap center frequencies with predefined targets. In practice, the design of metamaterials often involves trade-offs between multiple performance criteria, such as bandwidth, vibration transmissibility, mass, structural stiffness, manufacturability and cost. Future research could adopt multi-objective optimization frameworks to address these conflicting objectives simultaneously. Algorithms such as multi-objective genetic algorithms (MOGA), non-dominated sorting genetic algorithms (NSGA-II), or particle swarm optimization (PSO) can be employed to explore the optimal design space.

References

- Acar, G., & Yilmaz, C. (2013). Experimental and numerical evidence for the existence of wide and deep phononic gaps induced by inertial amplification in two-dimensional solid structures. *Journal of sound and vibration*, 332(24), 6389-6404.
- An, X., Yuan, X., Hou, X., & Fan, H. (2023). Low frequency vibration attenuation of meta-orthogrid sandwich panel with high load-bearing capacity.

 Composite structures, 305, 116560.

 doi:10.1016/j.compstruct.2022.116560
- An, X., Yuan, X., Sun, G., He, W., Lai, C., Hou, X., & Fan, H. (2024). Sandwich platetype metastructures with periodic graded resonators for low-frequency and broadband vibration attenuation. *Ocean Engineering*, 298, 117229.
- Araújo, A. L., Mota Soares, C. M., & Mota Soares, C. A. (2010). Finite Element Model for Hybrid Active-Passive Damping Analysis of Anisotropic Laminated Sandwich Structures. *The journal of sandwich structures & materials,* 12(4), 397-419. doi:10.1177/1099636209104534
- Banerjee, A., Adhikari, S., & Hussein, M. I. (2021). Inertial amplification band-gap generation by coupling a levered mass with a locally resonant mass.

 International journal of mechanical sciences, 207, 106630.

- Bhatt, A., Banerjee, A., & Adhikari, S. (2022). Closed-form solutions for attenuation peaks and band boundaries of general monocoupled systems. *Journal of sound and vibration*, *541*, 117318.
- Brillouin, L. (1953). Wave propagation in periodic structures: electric filters and crystal lattices (Vol. 2): Dover publications.
- Cai, C., Zhou, J., Wang, K., Lin, Q., Xu, D., & Wen, G. (2023). Quasi-zero-stiffness metamaterial pipe for low-frequency wave attenuation. *Engineering Structures*, 279, 115580.
- Cai, C., Zhou, J., Wang, K., Pan, H., Tan, D., Xu, D., & Wen, G. (2022). Flexural wave attenuation by metamaterial beam with compliant quasi-zero-stiffness resonators. *Mechanical Systems and Signal Processing*, 174, 109119.
- Cai, C., Zhou, J., Wang, K., Xu, D., & Wen, G. (2022). Metamaterial plate with compliant quasi-zero-stiffness resonators for ultra-low-frequency band gap. *Journal of sound and vibration*, 540, 117297.
- Carrera, E., Demirbas, M. D., & Augello, R. (2021). Evaluation of stress distribution of isotropic, composite, and FG beams with different geometries in nonlinear regime via Carrera-Unified Formulation and Lagrange polynomial expansions. *Applied Sciences*, 11(22), 10627.
- Carrera, E., Filippi, M., & Zappino, E. (2013). Free vibration analysis of rotating composite blades via Carrera Unified Formulation. *Composite* structures, 106, 317-325.

- Carrera, E., & Giunta, G. (2010). Refined beam theories based on a unified formulation.

 International Journal of Applied Mechanics, 2(01), 117-143.
- Carrera, E., & Zozulya, V. (2022). Carrera unified formulation for the micropolar plates.

 Mechanics of Advanced Materials and Structures, 29(22), 3163-3186.
- Chen, J. S., Sharma, B., & Sun, C. T. (2011). Dynamic behaviour of sandwich structure containing spring-mass resonators. *Composite structures*, *93*(8), 2120-2125. doi:10.1016/j.compstruct.2011.02.007
- Choi, J., Cho, T., Bae, S. G., & Park, H. S. (2022). Development and practical application of locally resonant metamaterials for attenuation of noise and flexural vibration of floors in residential buildings. *Journal of Building Engineering*, 57, 104907.
- Choi, J., Cho, T., & Park, H. S. (2023). Design and performance evaluation of steel beam members with plate - type locally resonant metamaterials for vibration control. *Computer - Aided Civil and Infrastructure Engineering*, 38(12), 1622-1637.
- Choi, J., Hong, T., Lee, D.-E., Cho, T., & Park, H. S. (2024). Hybrid behaviors of RC metaslab combining bandgap and isolation for broadband vibration control. *International journal of mechanical sciences*, 267, 109004.
- Cinefra, M., de Miguel, A. G., Filippi, M., Houriet, C., Pagani, A., & Carrera, E. (2021).

 Homogenization and free-vibration analysis of elastic metamaterial

- plates by Carrera Unified Formulation finite elements. *Mechanics of Advanced Materials and Structures*, 28(5), 476-485.
- De Miguel, A., Cinefra, M., Filippi, M., Pagani, A., & Carrera, E. (2021). Validation of FEM models based on Carrera Unified Formulation for the parametric characterization of composite metamaterials. *Journal of sound and vibration*, 498, 115979.
- Denli, H., & Sun, J. Q. (2007). Structural-acoustic optimization of sandwich structures with cellular cores for minimum sound radiation. *Journal of sound and vibration*, 301(1), 93-105. doi:10.1016/j.jsv.2006.09.025
- Fan, X., Li, J., Zhang, X., & Li, F. (2022). Multi-bandgaps metamaterial plate design using complex mass-beam resonator. *International journal of mechanical sciences*, 236, 107742. doi:10.1016/j.ijmecsci.2022.107742
- Fang, X., Chuang, K.-C., Jin, X., & Huang, Z. (2018). Band-gap properties of elastic metamaterials with inerter-based dynamic vibration absorbers. *Journal of Applied Mechanics*, 85(7), 071010.
- Fang, X., Wen, J., Bonello, B., Yin, J., & Yu, D. (2017). Wave propagation in one-dimensional nonlinear acoustic metamaterials. *New journal of physics*, 19(5), 053007.
- Fang, X., Wen, J., Yin, J., Yu, D., & Xiao, Y. (2016). Broadband and tunable one-dimensional strongly nonlinear acoustic metamaterials: theoretical study. *Physical Review E*, 94(5), 052206.

- Fang, X., Wen, J., Yu, D., & Yin, J. (2018). Bridging-coupling band gaps in nonlinear acoustic metamaterials. *Physical Review Applied*, 10(5), 054049.
- Frandsen, N. M., Bilal, O. R., Jensen, J. S., & Hussein, M. I. (2016). Inertial amplification of continuous structures: Large band gaps from small masses. *Journal of applied physics*, 119(12).
- Frandsen, N. M. M., Bilal, O. R., Jensen, J. S., & Hussein, M. I. (2016). Inertial amplification of continuous structures: Large band gaps from small masses. *Journal of applied physics*, 119(12), 124902. doi:10.1063/1.4944429
- Gao, L., Mak, C. M., & Cai, C. (2024). Low-frequency vibration attenuation of metamaterial sandwich plate with lever-type inertial amplified resonators. *Thin-Walled Structures*, 199, 111827. doi:10.1016/j.tws.2024.111827
- Gao, L., Mak, C. M., Cai, C., & Deng, S. (2024). Metamaterial sandwich plates with two-degree of freedom inertial amplified resonators for broadband low-frequency vibration attenuation. *Mechanics of Advanced Materials and Structures*, 1-13. doi:10.1080/15376494.2024.2329458
- Gao, L., Mak, C. M., Ma, K. W., & Cai, C. (2024). Mechanisms of multi-bandgap inertial amplification applied in metamaterial sandwich plates.

 International journal of mechanical sciences, 277, 109424.

- Gao, W., Qin, Z., & Chu, F. (2022). Broadband vibration suppression of rainbow metamaterials with acoustic black hole. *International journal of mechanical sciences*, 228, 107485.
- Hu, G., Austin, A. C., Sorokin, V., & Tang, L. (2021). Metamaterial beam with graded local resonators for broadband vibration suppression. *Mechanical Systems and Signal Processing*, 146, 106982.
- Huang, Y., Li, J., Chen, W., & Bao, R. (2019). Tunable bandgaps in soft phononic plates with spring-mass-like resonators. *International journal of mechanical sciences*, 151, 300-313.
- Hussain, S. I., & Lim, C. (2021). Composite trampoline metamaterial with enlarged local resonance bandgap. *Applied acoustics*, 184, 108353.
- Hussein, M. I., & Frazier, M. J. (2013). Metadamping: An emergent phenomenon in dissipative metamaterials. *Journal of sound and vibration*, 332(20), 4767-4774.
- Hussein, M. I., Patrick, I., Banerjee, A., & Adhikari, S. (2022). Metadamping in inertially amplified metamaterials: Trade-off between spatial attenuation and temporal attenuation. *Journal of sound and vibration*, 531, 116977.
- Jiang, W., Yin, M., Liao, Q., Xie, L., & Yin, G. (2021). Three-dimensional single-phase elastic metamaterial for low-frequency and broadband vibration mitigation. *International journal of mechanical sciences*, 190, 106023.

- Li, H., Hu, Y., Chen, J., Shou, D., & Li, B. (2022). Lightweight meta-lattice sandwich panels for remarkable vibration mitigation: Analytical prediction, numerical analysis and experimental validations. *Composites Part A:*Applied Science and Manufacturing, 163, 107218.
- Li, H., Hu, Y., Huang, H., Chen, J., Zhao, M., & Li, B. (2021). Broadband low-frequency vibration attenuation in 3D printed composite meta-lattice sandwich structures. *Composites Part B: Engineering*, 215, 108772.
- Li, H., Li, Y., & Liu, X. (2023). Double-beam metastructure with inertially amplified resonators for flexural wave attenuation. *European Journal of Mechanics-A/Solids*, 97, 104794.
- Li, J., Fan, X., & Li, F. (2020). Numerical and experimental study of a sandwich-like metamaterial plate for vibration suppression. *Composite structures*, 238, 111969. doi:10.1016/j.compstruct.2020.111969
- Li, J., Yang, P., & Li, S. (2020). Phononic band gaps by inertial amplification mechanisms in periodic composite sandwich beam with lattice truss cores. *Composite structures*, 231, 111458.
- Li, J., Yang, P., & Xia, M. (2022). Actively tuning of transverse wave band gaps in hybrid sandwich beam metamaterials with shunted piezoelectric array and inertial amplification mechanism. *Journal of Intelligent Material Systems and Structures*, 33(20), 2520-2541.

- Li, J., Zhang, Y., Fan, X., & Li, F. (2023). Multi bandgaps design of sandwich metamaterial plate with embedded membrane-type resonators. *Journal of Sandwich Structures & Materials*, 25(3), 311-329.
- Li, Y., & Zhou, W. (2021). Bandgap and vibration transfer characteristics of scissor-like periodic metamaterials. *Journal of applied physics*, 130(2).
- Li, Z.-Y., Ma, T.-X., Wang, Y.-Z., Chai, Y.-Y., Zhang, C., & Li, F.-M. (2022). Active auto-adaptive metamaterial plates for flexural wave control.

 International journal of solids and structures, 254, 111865.
- Li, Z.-Y., Ma, T.-X., Wang, Y.-Z., Li, F.-M., & Zhang, C. (2020). Vibration isolation by novel meta-design of pyramid-core lattice sandwich structures.

 **Journal of sound and vibration, 480, 115377.
- Li, Z.-Y., Wang, Y.-Z., Ma, T.-X., Zheng, Y.-F., Zhang, C., & Li, F.-M. (2022). A self-sensing and self-actuating metamaterial sandwich structure for the low-frequency vibration mitigation and isolation. *Composite structures*, 297, 115894.
- Li, Z.-Y., Xie, L.-T., Ma, T.-X., Wang, Y.-Z., Chai, Y.-Y., Zhang, C., & Li, F.-M. (2024). A simple active adaptive control method for mitigating and isolating mechanical vibrations of the pyramid-core lattice sandwich structures. *Journal of sound and vibration*, 577, 118321.
- Lim, C. (2019). Elastic waves propagation in thin plate metamaterials and evidence of low frequency pseudo and local resonance bandgaps. *Physics Letters A*, 383(23), 2789-2796.

- Lim, C., Li, J. T., & Zhao, Z. (2020). Lightweight architected lattice phononic crystals with broadband and multiband vibration mitigation characteristics. *Extreme Mechanics Letters*, 41, 100994.
- Lin, Q., Zhou, J., Wang, K., Xu, D., Wen, G., Wang, Q., & Cai, C. (2022). Low-frequency locally resonant band gap of the two-dimensional quasi-zero-stiffness metamaterials. *International journal of mechanical sciences*, 222, 107230.
- Lin, S., Zhang, Y., Liang, Y., Liu, Y., Liu, C., & Yang, Z. (2021). Bandgap characteristics and wave attenuation of metamaterials based on negative-stiffness dynamic vibration absorbers. *Journal of sound and vibration*, 502, 116088. doi:10.1016/j.jsv.2021.116088
- Liu, Y., Yang, J., Yi, X., Guo, W., Feng, Q., & Chronopoulos, D. (2022). Enhanced vibration suppression using diatomic acoustic metamaterial with negative stiffness mechanism. *Engineering Structures*, 271, 114939.
- Liu, Z., Zhang, X., Mao, Y., Zhu, Y. Y., Yang, Z., Chan, C. T., & Sheng, P. (2000).
 Locally Resonant Sonic Materials. Science (American Association for the Advancement of Science), 289(5485), 1734-1736.
 doi:10.1126/science.289.5485.1734
- Lou, J., Zhang, S., Fan, H., Fang, X., & Du, J. (2025). Ultra-low frequency and broadband flexural wave attenuation using an inertant nonlinear metamaterial beam. *Engineering Structures*, 323, 119169.

- Luo, Y., Xie, S., & Zhang, X. (2008). The actuated performance of multi-layer piezoelectric actuator in active vibration control of honeycomb sandwich panel. *Journal of sound and vibration*, 317(3), 496-513. doi:10.1016/j.jsv.2008.03.047
- Mak, C. M., & Jianxin, S. (2002). A power transmissibility method for assessing the performance of vibration isolation of building services equipment.

 Applied acoustics, 63(12), 1281-1299.
- Mak, C. M., Ma, K. W., & Wong, H. M. (2023). Prediction and Control of Noise and Vibration from Ventilation Systems: CRC Press.
- Mead, D. M. (1996). WAVE PROPAGATION IN CONTINUOUS PERIODIC STRUCTURES: RESEARCH CONTRIBUTIONS FROM SOUTHAMPTON, 1964–1995. *Journal of sound and vibration, 190*(3), 495-524. doi:10.1006/jsvi.1996.0076
- Mei, C., Li, L., Li, X., Jiang, Y., Han, X., Tang, H., Wang, X., & Hu, Y. (2023). Spatiotemporal damping of dissipative metamaterial. *International journal of mechanical sciences*, 254, 108393.
- Mi, Y., & Yu, X. (2021). Sound transmission of acoustic metamaterial beams with periodic inertial amplification mechanisms. *Journal of sound and vibration*, 499, 116009.
- Mizukami, K., Funaba, K., & Ogi, K. (2021). Design and three-dimensional printing of carbon-fiber-composite elastic metamaterials with inertial amplification mechanisms. *Journal of sound and vibration*, 513, 116412.

- Mousavi, S. H., Khanikaev, A. B., & Wang, Z. (2015). Topologically protected elastic waves in phononic metamaterials. *Nature communications*, 6(1), 8682.
- Mu, D., Wang, K., Shu, H., & Lu, J. (2022a). Low frequency broadband bandgaps in elastic metamaterials with two-stage inertial amplification and elastic foundations. *Journal of physics. D, Applied physics, 55*(34), 345302. doi:10.1088/1361-6463/ac7480
- Mu, D., Wang, K., Shu, H., & Lu, J. (2022b). Metamaterial beams with graded twostage inertial amplification and elastic foundation. *International journal* of mechanical sciences, 236, 107761.
- Muhammad, & Lim, C. W. (2019). Elastic waves propagation in thin plate metamaterials and evidence of low frequency pseudo and local resonance bandgaps. *Physics letters*. *A*, 383(23), 2789-2796. doi:10.1016/j.physleta.2019.05.039
- Muhammad, S., Wang, S., Li, F., & Zhang, C. (2020). Bandgap enhancement of periodic nonuniform metamaterial beams with inertial amplification mechanisms. *Journal of vibration and control*, 26(15-16), 1309-1318.
- Nobrega, E., Gautier, F., Pelat, A., & Dos Santos, J. (2016). Vibration band gaps for elastic metamaterial rods using wave finite element method.

 *Mechanical Systems and Signal Processing, 79, 192-202.
- Orta, A. H., & Yilmaz, C. (2019). Inertial amplification induced phononic band gaps generated by a compliant axial to rotary motion conversion mechanism.

- Journal of sound and vibration, 439, 329-343. doi:10.1016/j.jsv.2018.10.014
- Otlu, S. N., Acar, B., Tetik, Z. G., & Yilmaz, C. (2023). Three-dimensional ultra-wide elastic metamaterial with inertial amplification mechanisms having optimized flexure hinges. *International journal of solids and structures*, 282, 112453.
- Oudich, M., Senesi, M., Assouar, M. B., Ruzenne, M., Sun, J.-H., Vincent, B., Hou, Z., & Wu, T.-T. (2011). Experimental evidence of locally resonant sonic band gap in two-dimensional phononic stubbed plates. *Physical Review B—Condensed Matter and Materials Physics*, 84(16), 165136.
- Pagani, A., & Carrera, E. (2017). Large-deflection and post-buckling analyses of laminated composite beams by Carrera Unified Formulation. *Composite* structures, 170, 40-52.
- Patro, S. R., Banerjee, A., & Ramana, G. (2023). Vibration attenuation characteristics of finite locally resonant meta beam: Theory and experiments. *Engineering Structures*, 278, 115506.
- Peng, H., & Pai, P. F. (2014). Acoustic metamaterial plates for elastic wave absorption and structural vibration suppression. *International journal of mechanical sciences*, 89, 350-361.
- Peng, H., Pai, P. F., & Deng, H. (2015). Acoustic multi-stopband metamaterial plates design for broadband elastic wave absorption and vibration suppression.

 International journal of mechanical sciences, 103, 104-114.

- Qiang, C., Hao, Y., Zhang, W., Li, J., Yang, S., & Cao, Y. (2021). Bandgaps and vibration isolation of local resonance sandwich-like plate with simply supported overhanging beam. *Applied Mathematics and Mechanics*, 42(11), 1555-1570.
- Russillo, A. F., Failla, G., & Alotta, G. (2022). Ultra-wide low-frequency band gap in locally-resonant plates with tunable inerter-based resonators. *Applied Mathematical Modelling*, 106, 682-695.
- Ruzzene, M. (2004). Vibration and sound radiation of sandwich beams with honeycomb truss core. *Journal of sound and vibration*, 277(4-5), 741-763.
- Sheng, P., Fang, X., Dai, L., Yu, D., & Wen, J. (2023). Synthetical vibration reduction of the nonlinear acoustic metamaterial honeycomb sandwich plate.

 Mechanical Systems and Signal Processing, 185, 109774.
- Shi, D., Liu, Y., Chen, H., Meng, F., An, X., Jin, F., & Fan, H. (2022). An engineering feasible metastructure: Ring-spring-resonator based sandwich metabeam for vibration attenuation. *Engineering Structures*, 273, 115105.
- Song, Y., Feng, L., Liu, Z., Wen, J., & Yu, D. (2019). Suppression of the vibration and sound radiation of a sandwich plate via periodic design. *International journal of mechanical sciences*, 150, 744-754. doi:10.1016/j.ijmecsci.2018.10.055

- Song, Y., Wen, J., Tian, H., Lu, X., Li, Z., & Feng, L. (2020). Vibration and sound properties of metamaterial sandwich panels with periodically attached resonators: Simulation and experiment study. *Journal of sound and vibration*, 489, 115644. doi:10.1016/j.jsv.2020.115644
- Sugino, C., Leadenham, S., Ruzzene, M., & Erturk, A. (2016). On the mechanism of bandgap formation in locally resonant finite elastic metamaterials.

 **Journal of applied physics, 120(13).
- Sugino, C., Xia, Y., Leadenham, S., Ruzzene, M., & Erturk, A. (2017). A general theory for bandgap estimation in locally resonant metastructures.

 **Journal of sound and vibration, 406, 104-123.
- Sun, Y., Dong, J., Lee, H. P., & Zheng, H. (2024). Sound transmission characteristics of X-shape inertial amplification acoustic metamaterial. *Applied acoustics*, 218, 109908.
- Sun, Y., Gong, D., Zhou, J., Sun, W., & Xia, Z. (2019). Low frequency vibration control of railway vehicles based on a high static low dynamic stiffness dynamic vibration absorber. *Science China Technological Sciences*, 62(1), 60-69. doi:10.1007/s11431-017-9300-5
- Sun, Y., Li, Y., Zhang, G., Lee, H. P., Zheng, H., & Li, F. (2025). Inertial amplification stiffened meta-panels for low-frequency sound insulation. *International journal of mechanical sciences*, 110116.

- Sun, Y., Zhang, G., Lee, H. P., Zheng, H., Luo, Z., & Li, F. (2024). Sound transmission of truss-based X-shaped inertial amplification metamaterial double panels. *International journal of mechanical sciences*, 283, 109669.
- Tallarico, D., Bergamini, A., & Van Damme, B. (2023). Long-range order Bragg scattering and its effect on the dynamic response of a Penrose-like phononic crystal plate. *Physical Review B*, 107(17), 174201.
- Tao, Z., Ren, X., Zhao, A. G., Sun, L., Zhang, Y., Jiang, W., Han, D., Zhang, X. Y., & Xie, Y. M. (2022). A novel auxetic acoustic metamaterial plate with tunable bandgap. *International journal of mechanical sciences*, 226, 107414.
- Teng, X. C., Ni, X. H., Zhang, X. G., Jiang, W., Zhang, Y., Xu, H. H., Hao, J., Xie, Y. M., & Ren, X. (2023). Design and mechanical performance of stretchable sandwich metamaterials with auxetic panel and lattice core. *Thin-Walled Structures*, 192, 111114.
- Thomes, R. L., Beli, D., & Junior, C. D. M. (2022). Space-time wave localization in electromechanical metamaterial beams with programmable defects.

 *Mechanical Systems and Signal Processing, 167, 108550.
- Timorian, S., Ouisse, M., Bouhaddi, N., De Rosa, S., & Franco, F. (2020). Numerical investigations and experimental measurements on the structural dynamic behaviour of quasi-periodic meta-materials. *Mechanical Systems and Signal Processing*, 136, 106516.

- Vinson, J. R. (2001). Sandwich Structures. *Applied Mechanics Reviews*, *54*(3), 201-214. doi:10.1115/1.3097295
- Vo, N. H., Pham, T. M., Hao, H., Bi, K., & Chen, W. (2022). A reinvestigation of the spring-mass model for metamaterial bandgap prediction. *International journal of mechanical sciences*, 221, 107219.
- Wang, Q., Li, J., Zhang, Y., Xue, Y., & Li, F. (2021). Bandgap properties in metamaterial sandwich plate with periodically embedded plate-type resonators. *Mechanical Systems and Signal Processing*, 151, 107375. doi:10.1016/j.ymssp.2020.107375
- Wang, S., Wang, M., & Guo, Z. (2021). Adjustable low-frequency bandgap of flexural wave in an Euler-Bernoulli meta-beam with inertial amplified resonators. *Physics letters. A, 417*, 127671. doi:10.1016/j.physleta.2021.127671
- Wang, T., Li, S., & Nutt, S. R. (2009). Optimal design of acoustical sandwich panels with a genetic algorithm. *Applied acoustics*, 70(3), 416-425. doi:10.1016/j.apacoust.2008.06.003
- Wang, Y., Perras, E., Golub, M. V., Fomenko, S. I., Zhang, C., & Chen, W. (2021).
 Manipulation of the guided wave propagation in multilayered phononic plates by introducing interface delaminations. *European journal of mechanics*, A, Solids, 88, 104266.
 doi:10.1016/j.euromechsol.2021.104266

- Wu, Z.-J., Li, F.-M., & Wang, Y.-Z. (2013). Vibration band gap behaviors of sandwich panels with corrugated cores. *Computers & structures*, 129, 30-39. doi:10.1016/j.compstruc.2013.08.009
- Wu, Z., Liu, W., Li, F., & Zhang, C. (2019). Band-gap property of a novel elastic metamaterial beam with X-shaped local resonators. *Mechanical Systems and Signal Processing*, 134, 106357.
- Xi, C., Dou, L., Mi, Y., & Zheng, H. (2021). Inertial amplification induced band gaps in corrugated-core sandwich panels. *Composite structures*, 267, 113918. doi:10.1016/j.compstruct.2021.113918
- Xi, C., Zheng, H., Mi, Y., & Yu, X. (2023). Lever-type inertial amplification plates for low-frequency vibration reduction. *Thin-Walled Structures*, 192, 111131.
- Xi, C., Zhu, X., & Zheng, H. (2022). A corrugated-core sandwich beam with local resonators for low-frequency broadband elastic wave attenuation.

 Journal of vibration and control, 28(23-24), 3482-3494.

 doi:10.1177/10775463211034957
- Xiao, X., He, Z., Li, E., & Cheng, A. (2019). Design multi-stopband laminate acoustic metamaterials for structural-acoustic coupled system. *Mechanical Systems and Signal Processing*, 115, 418-433.
- Xu, J., & Jing, J. (2024). Low-frequency band gaps in quasi-zero stiffness locally resonant metamaterial shaft. *International journal of mechanical sciences*, 267, 108992.

- Xue, Y., Li, J., Wang, Y., Song, Z., & Krushynska, A. O. (2024). Widely tunable magnetorheological metamaterials with nonlinear amplification mechanism. *International journal of mechanical sciences*, 264, 108830.
- Xue, Z., & Hutchinson, J. W. (2004). A comparative study of impulse-resistant metal sandwich plates. *International Journal of Impact Engineering*, 30(10), 1283-1305.
- Yan, G., Yao, S., & Li, Y. (2022). Propagation of elastic waves in metamaterial plates with various lattices for low-frequency vibration attenuation. *Journal of sound and vibration*, 536, 117140. doi:10.1016/j.jsv.2022.117140
- Yang, J., Xiong, J., Ma, L., Wang, B., Zhang, G., & Wu, L. (2013). Vibration and damping characteristics of hybrid carbon fiber composite pyramidal truss sandwich panels with viscoelastic layers. *Composite structures*, 106, 570-580. doi:10.1016/j.compstruct.2013.07.015
- Yao, S., Zhou, X., & Hu, G. (2008). Experimental study on negative effective mass in a 1D mass–spring system. *New journal of physics*, 10(4), 043020. doi:10.1088/1367-2630/10/4/043020
- Yasuda, H., & Yang, J. (2015). Reentrant origami-based metamaterials with negative Poisson's ratio and bistability. *Physical review letters*, 114(18), 185502-185502. doi:10.1103/PhysRevLett.114.185502
- Yilmaz, C., & Hulbert, G. M. (2010). Theory of phononic gaps induced by inertial amplification in finite structures. *Physics letters*. *A*, 374(34), 3576-3584. doi:10.1016/j.physleta.2010.07.001

- Yilmaz, C., Hulbert, G. M., & Kikuchi, N. (2007). Phononic band gaps induced by inertial amplification in periodic media. *Physical review. B, Condensed matter and materials physics*, 76(5). doi:10.1103/PhysRevB.76.054309
- Yilmaz, C., & Kikuchi, N. (2006). Analysis and design of passive low-pass filter-type vibration isolators considering stiffness and mass limitations. *Journal of sound and vibration*, 293(1), 171-195. doi:10.1016/j.jsv.2005.09.016
- Yu, D., Liu, Y., Wang, G., Zhao, H., & Qiu, J. (2006). Flexural vibration band gaps in Timoshenko beams with locally resonant structures. *Journal of applied physics*, 100(12), 124901.
- Yu, G.-L., & Miao, H.-W. (2019). On vibration isolation of sandwich plate with periodic hollow tube core. *Journal of Sandwich Structures & Materials*, 21(3), 1119-1132.
- Yuksel, O., & Yilmaz, C. (2015). Shape optimization of phononic band gap structures incorporating inertial amplification mechanisms. *Journal of sound and vibration*, 355, 232-245.
- Yuksel, O., & Yilmaz, C. (2020). Realization of an ultrawide stop band in a 2-D elastic metamaterial with topologically optimized inertial amplification mechanisms. *International journal of solids and structures*, 203, 138-150. doi:10.1016/j.ijsolstr.2020.07.018
- Zeng, Y., Cao, L., Wan, S., Guo, T., An, S., Wang, Y.-F., Du, Q.-J., Vincent, B., Wang, Y.-S., & Assouar, B. (2022). Inertially amplified seismic metamaterial

- with an ultra-low-frequency bandgap. *Applied Physics Letters*, 121(8), 081701.
- Zeng, Y., Cao, L., Wan, S., Guo, T., Wang, Y.-F., Du, Q.-J., Assouar, B., & Wang, Y.-S. (2022). Seismic metamaterials: Generating low-frequency bandgaps induced by inertial amplification. *International journal of mechanical sciences*, 221, 107224. doi:10.1016/j.ijmecsci.2022.107224
- Zhang, J., Dong, X., Wang, T., Chen, K., Sun, Y., & Peng, Z. (2025). Attenuation enhancement for the inertial amplification metamaterial using multiple local resonators. *Journal of sound and vibration*, 600, 118874.
- Zhang, S., Lou, J., Fan, H., & Du, J. (2023). A nonlinear acoustic metamaterial beam with tunable flexural wave band gaps. *Engineering Structures*, 276, 115379.
- Zhang, Y., Fan, X., Li, J., Li, F., Yu, G., Zhang, R., & Yuan, K. (2021). Low-frequency vibration insulation performance of the pyramidal lattice sandwich metamaterial beam. *Composite structures*, 278, 114719. doi:10.1016/j.compstruct.2021.114719
- Zhao, C., Zhang, K., Zhao, P., & Deng, Z. (2023). Finite-amplitude nonlinear waves in inertial amplification metamaterials: theoretical and numerical analyses.

 **Journal of sound and vibration, 560, 117802.
- Zhao, C., Zhang, K., Zhao, P., Hong, F., & Deng, Z. (2023). Bandgap merging and backward wave propagation in inertial amplification metamaterials. *International journal of mechanical sciences*, 250, 108319.

- Zhao, P., Zhang, K., Zhao, C., Qi, L., & Deng, Z. (2021). In-plane wave propagation analysis for waveguide design of hexagonal lattice with Koch snowflake.

 International journal of mechanical sciences, 209, 106724.

 doi:10.1016/j.ijmecsci.2021.106724
- Zok, F. W., Waltner, S. A., Wei, Z., Rathbun, H. J., McMeeking, R. M., & Evans, A. G. (2004). A protocol for characterizing the structural performance of metallic sandwich panels: application to pyramidal truss cores.
 International journal of solids and structures, 41(22), 6249-6271.
 doi:10.1016/j.ijsolstr.2004.05.045